Band gap engineering of a MoS_2 monolayer through transition metal and chalcogen alloying: an *ab initio* study

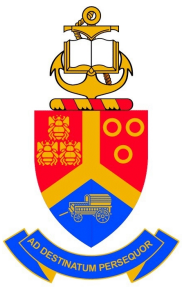

by
Noeliarinala Felana Andriambelaza

Submitted in partial fulfilment of the requirements
for the degree
Philosophiæ Doctor (PhD) in Physics
in the Faculty of Natural and Agricultural Sciences
University of Pretoria

Supervisor: Prof. Nithaya Chetty
Co-Supervisor: Dr. Refilwe Edwin Mapasha

February 13, 2019

UNIVERSITEIT VAN PRETORIA
UNIVERSITY OF PRETORIA
YUNIBESITHI YA PRETORIA

UNIVERSITY OF PRETORIA

DECLARATION OF ORIGINALITY

This document must be signed and submitted with every essay, report, project, assignment, dissertation and/or thesis.

Full names of student: NOELIARINALA FELANA ANDRIAMBELAZA

Student number: u15405908

Personnel number:

Declaration

1. I understand what plagiarism is and am aware of the University's policy in this regard.
2. I declare that this thesis is my own original work. Where other people's work has been used (either from a printed source, Internet or any other source), this has been properly acknowledged and referenced in accordance with departmental requirements.
3. I have not used work previously produced by another student or any other person to hand in as my own.
4. I have not allowed, and will not allow, anyone to copy my work with the intention of passing it off as his or her own.

SIGNATURE STUDENT:.....

SIGNATURE SUPERVISOR:.....

Abstract

In this thesis, density functional theory (DFT) calculations are performed to study the transition metal and chalcogen alloying of a molybdenum disulfide (MoS_2) monolayer for band gap engineering. The effects of the foreign atoms on the thermodynamic stability, structural and electronic properties of the MoS_2 monolayer are investigated. To study these effects systematically at different alloying concentrations, the possible line-ordered configurations at each concentration are considered. Their energetics, structural and electronic properties are compared with the well-known alloy shapes, random and/or cluster configurations.

For the case of the transition metal alloying, chromium (Cr) atoms are introduced at the molybdenum (Mo) sites. Various unique line-ordered configurations are considered at each concentration. The most stable ones are identified by means of formation energies. The energetics comparison of the line-ordered alloy and the random configurations generated using special quasirandom structure (SQS) shows that the line-ordered alloy configurations have relatively low formation energies compared to the random configurations. The formation energies of all considered configurations are positive but relatively small, revealing that both shapes of the Cr alloying can be synthesized and co-exist at the same synthesis conditions. For the structural properties, the increase in Cr concentration reduces the lattice constant of the MoS_2 system following the Vegard's law. The Cr atoms fine-tune the band gap of a MoS_2 monolayer from 1.65 eV to 0.86 eV. Based on the partial density of states and the charge density analysis, the Cr $3d$ and Mo $4d$ at the vicinity of the band edges are found to be the main responsible for the reduction of the band gap.

For the chalcogen alloying, the influence of the oxygen (O) and tellurium (Te) atoms are considered. We start with the study of the O alloying in a MoS_2 monolayer appearing in different shapes: line-ordered, cluster and random. The small calculated formation energy values of the various O alloy configurations show that this alloying

are stable and should be synthesizable under favorable conditions. At high concentration, the O line-ordered alloys seem to be constantly most stable compared to the considered random and cluster alloy configurations, while the formation energies of all the configurations are nearly the same at low concentration. Although the O atom has small atomic radii compared to the S atom, their alloying preserve the 2D hexagonal structure of the MoS_2 monolayer at each concentration. However, the lattice constant decreases linearly with the increase in O concentration, consistent with Vegard's law. The introduction of O atom in the MoS_2 monolayer also fine-tunes the band gap of the MoS_2 monolayer with a range of 1.65 eV to 0.98 eV. The band gap reduction is mainly contributed by the Mo $4d$ and O $2p$ orbitals at the band edges.

We further carried out a thorough systematic study of Te line-ordered alloys in a MoS_2 monolayer. The low formation energies of the Te line-ordered alloy configurations indicate that they are also thermodynamically stable at low concentration. The obtained formation energies for line-ordered alloy configurations at each concentration compete very well with the random configurations that are already achieved experimentally. The structural characterization indicates that the lowest energy configuration at each concentration corresponds to the configuration where the Te atom rows are far apart from each other within the supercell. Similar to that of O alloying, the variation of the lattice constant at different concentrations obeys Vegard's law, but its values increase with the concentration since Te atom has larger atomic radius than S and O atoms. The Te alloying fine-tunes the band gap ranging between the MoS_2 (1.65 eV) and the $MoTe_2$ (1.04 eV) band gap values .

In brief, the Cr, O and Te successfully engineer the band of a MoS_2 monolayer, and their study should be beneficial for nanotechnological applications.

Dedication

To my parents, for their endless love, support and encouragement.

Acknowledgements

First and foremost, I would like to thank God Almighty for giving me strength, inspiration, wisdom, knowledge and understanding, to undertake this PhD program and to complete it satisfactorily. Without His blessings, this accomplishment would not have been possible.

I would like to express my deepest appreciation to my supervisor Prof Nithaya Chetty for his guidance, encouragement, valuable discussions and support throughout my PhD research studies. It was an honour and a great opportunity for me to share his extraordinary expertise in my area of research, and also of his exceptional human qualities.

I would also like to extend my deepest gratitude to my co-supervisor Dr Refilwe Edwin Mapasha for his constant support, availability and constructive suggestions, which were valuable for the completion of this thesis.

I would like to acknowledge the University of Pretoria for financial assistance, that allowed me to stay in South Africa and to complete this degree.

I would like to thank Dr Richard Andrew for the all fruitful and constructive discussions.

My sincere gratitude to my former advisor Prof Andrianelison Rakotomahevitra, for his help and effort to find this PhD position for me.

I would like to thank all members of the computational and solid state physics research group at the University of Pretoria for their willingness to help, their interest and encouragement.

I would like to offer my special thanks to Mr Shaunel Walker for listening, offering me advice, and supporting me through this entire process.

I also would like to express my sincere thanks to my family for the support they have provided me throughout my entire life and particularly during the PhD research process. Where I am today and what I am today is because of their unconditional love, prayers and sacrifice.

Contents

List of Figures

Acronyms

AACVD aerosol assisted chemical vapour deposited. 22, 23

ADF annular dark field. 17, 24

AE all-electron. 61–64, 66

APW augmented plane wave. 54

BO Born-Oppenheimer. 34, 60

CBM conduction band minimum. 17, 20, 21, 147

CVD chemical vapor deposition. 3, 4, 6, 17, 19, 22–25

CVT chemical vapor transport. 18, 19

DFT density functional theory. 6, 8, 10, 17, 19, 23, 27, 32, 38–40, 42, 46, 48, 50–52, 56, 58, 66, 145, 149

DOS density of states. 17–19, 23, 26, 38, 58, 147, 148

EBS effective band structure. 26

EDX energy-dispersive X-ray. 22, 23

EPM empirical pseudopotential method. 61

EXAFS extended X-ray absorption fine structure. 18

FBZ first Brillouin zone. 56, 58, 59, 66

FET field effect transistor. 6, 19

GGA generalized gradient approximation. 32, 46, 49, 50, 52

HF Hartree-Fock. 32, 38, 39, 47, 51–54

HRTEM high-resolution transmission electron microscopy. 17

HSE Heyd, Scuseria, Ernzerhof. 53, 54

ICP-OES inductively coupled plasma optical emission spectroscopy. 22

KS Kohn-Sham. 32, 42–44, 54, 56, 57, 60

LDA local density approximation. 32, 46, 48, 49, 51

LDOS local densities of states. 19

PAW projector augmented wave. 61–64, 66

PBC periodic boundary conditions. 55

PBE Perdew, Burke, Ernzerhof. 21, 49, 50, 52, 54

PDOS partial density of states. 9

PL photoluminescence. 6, 19, 22, 25

PVD physical vapor deposition. 17

PW Perdew and Wang. 48

PZ Perdew and Zunger. 48

QMC quantum Monte Carlo. 46, 48

SPW symmetrized plane-waves. 58

SQS special quasirandom structure. 9, 145, 146, 157

STEM scanning transmission electron microscope. 17, 19, 22–25

TMD transition metal dichalcogenides. iv, 1–3, 5, 21, 22, 26, 149, 157, 158

TMO transition metal oxides. 8

VASP Vienna *ab initio* simulation packages. 54, 67

VBM valence band maximum. 17, 19–21, 147

VWN Vosko, Wilk and Nusair. 48

XPS X-ray photoelectron spectroscopy. 24

Chapter 1

Introduction

We give, in this preliminary chapter, a brief overview of the two dimensional (2D) transition metal dichalcogenides (TMD) more especially the 2D molybdenum disulfide (MoS_2). The recent techniques to prepare the MoS_2 monolayer are discussed. We also describe the various extraordinary properties of the 2D MoS_2 that could be important for the next generation device applications. The aims and objectives of this thesis are introduced at the end of this chapter.

1.1 Rationale

The fabrication of the optoelectronic and electronic devices usually relies on the bulk semiconductors, such as silicon (Si), gallium nitride (GaN), gallium arsenide (GaAs), etc. Nowadays, the demand of the society for the miniaturization of such devices increases rapidly. Thus, this becomes the main focus of many research topics in material science as well as in the manufacturing industry. This miniaturization requires the exploitation of materials at nanometre scale on the devices. The 2D materials are promising candidates for this application based on their size and other extraordinary properties [1, 2, 3, 4]. For the past decades, the synthesis of 2D materials was consid-

ered to be impossible until 2004, when Novoselov *et. al* [1, 5, 6] reverse this misconception. They successfully synthesized the first free standing graphene, cleaved from bulk graphite using a scotch tape [1, 5, 6]. Although graphene presents interesting properties such as strong mechanical properties [7, 8], very thin [1], high electron mobility [9], transparent [10] and mechanical flexibility [11], its zero-gap property [1, 12, 13] restricts its direct integration in the nanotechnological devices that required semiconductor materials. However, the efficient synthesis of graphene opened up a way to search for other 2D materials of different physical properties such as hexagonal boronitrene (h-BN) [2, 14], transition metal dichalcogenides (TMD) [3, 4, 15, 16, 17], phosphorene [18] and silicene [19, 20]. The TMD monolayers are interesting materials due to their broad electronic properties [21, 22], from metallic behaviors ($NbTe_2$ monolayer) to semiconductors (MoS_2 monolayer), the high charge carrier mobility [4], extreme mechanical strength and flexibility [4, 23].

A TMD monolayer is denoted by the formula T_MX_2, where T_M is a transition metal such as molybdenum (Mo), tungsten (W), chromium (Cr), niobium (Nb), rhenium (Re), etc., and X is chalcogen such as sulfur (S), selenium (Se) and tellurium (Te). There are two polytypes of TMD monolayers: 2H and 1T structures [21, 22]. The common feature of these two structures is that both systems are constructed by two layers of chalcogen X atom sandwiching one layer of transition metal T_M atom as seen in Fig. 1.1. Their difference arises from the crystal symmetry; the 2H structure has a hexagonal symmetry, where the chalcogens X in the upper layer are situated directly above those of the bottom layer (see Fig. 1.1a). However, the 1T structure has a tetragonal structure, where the layers of chalcogen are offset from each other (see Fig. 1.1b). Numerous TMD monolayers have been predicted, characterized and found to be thermodynamically stable [22]. They are presented in Fig. 1.2 with their corresponding stable structural symmetries [22]. The MoS_2 monolayer is a typical TMD monolayer [21, 22]. Similar to graphite [1], the molybdenite (bulk MoS_2) crystals in

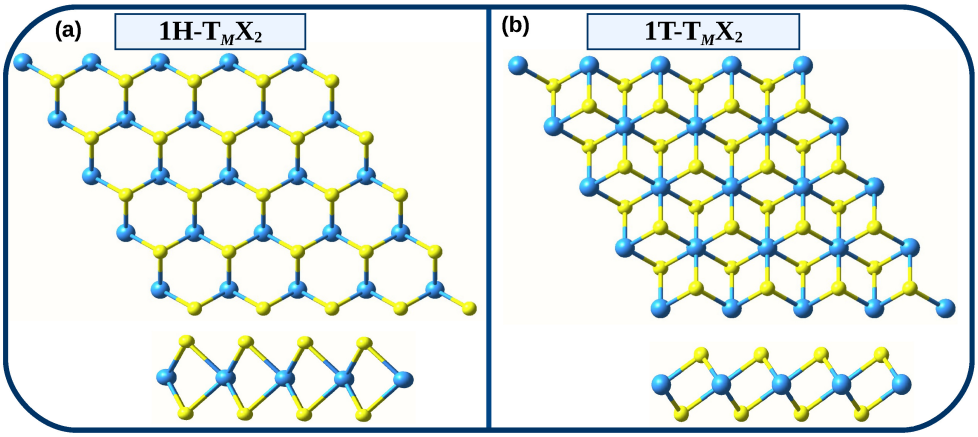

Figure 1.1: The two polytypes: (a) hexagonal (H) and (b) tetragonal (T) structures of a transition metal dichalcogenide (TMD) monolayer. The blue and yellow spheres in (a) and (b) indicate the transition metal and chalcogen atoms of the TMD monolayer respectively.

layered form is naturally abundant in the earth crust [24, 25]. As seen in Fig 1.2, the MoS_2 monolayer is stable in H symmetry. The energy of the 1T-MoS_2 monolayer is 0.28 eV/atom higher than the 2H-MoS_2 monolayer [26]. These two phases of the MoS_2 monolayer also have different electronic properties. The H structure is a semiconductor material while the 1T structure is metallic. In the entire study of this thesis, we consider the hexagonal H structure of the MoS_2 monolayer.

The MoS_2 monolayer can be synthesized using different methods such as chemical exfoliation, mechanical exfoliation from the MoS_2 bulk and chemical vapor deposition (CVD) technique. The easiest and popularly used method is the mechanical exfoliation [1, 4]. Due to the weak interactions between layers, it is easier to mechanically cleave a single layer of MoS_2 using a scotch tape method [1, 4]. The cleaved monolayer comes with purity and cleanliness [24], making it a suitable method to study the fundamental properties of this monolayer. However, this method produces the small sizes of MoS_2, and the produced layers are not controllable both horizontally and vertically. Thus, it limits its application in the commercial production. The chemical exfoliation,

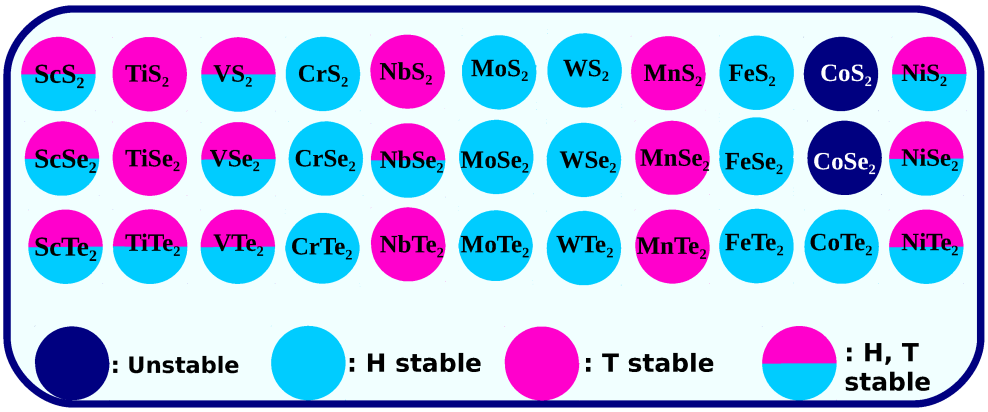

Figure 1.2: Various TMD monolayers with their corresponding stable structures. The blue circle corresponds to unstable TMD material either in H or T structures. Pink circle indicates that the material is stable in H structure. Grey circle indicates that the material is stable in T structure. Half grey/half blue sphere means the TMD material is stable in both structure.

involving ion intercalation [27, 28] and solvent-based method [27, 29], is another type of exfoliation used to prepare the MoS_2 monolayer. This method can synthesize a large quantity of MoS_2 monolayer. However, there are many defects in the MoS_2 structure occurred during this process [24, 29]. The other possible synthetic method, CVD is enabled to synthesize a large-area of MoS_2 monolayer [30, 31, 32, 33, 34].

The MoS_2 monolayer is a promising candidate for the nanotechnological devices due to its numerous extraordinary properties [4, 23, 35, 36, 37]. Amongst of them, it exhibits extraordinary electronic properties compared to those of its bulk counterpart. The MoS_2 material has fascinating thickness dependent electronic properties. From bulk to monolayer, the band gap increases from 1.2 eV (indirect) to 1.9 eV (direct band gap) [23, 35, 36]. The MoS_2 monolayer also presents a moderate charge carrier mobility of $\sim$200 $cm^2\ V^{-1}\ s^{-1}$ and a current on/off ratio of 10^8 at room temperature [4]. Furthermore, it has tremendous mechanical properties and strength, making this 2D material a good candidate for the next generation devices. It has an effective in plane Young's modulus of 270$\pm$100 GPa and an average in plane breaking strength of 15$\pm$3Nm^{-1} comparable

to those of steel [23]. In addition, although it is a strong material, the MoS_2 monolayer possesses a high flexibility along the vertical axis, essential for the fabrication of flexible devices. It can retain its carrier mobility at a curvature of 0.75mm [38]. It is noteworthy that the popularity of the MoS_2 monolayer is not only due to the well known intrinsic extraordinary properties but also due to its band gap tunability.

Generally, the implementation of a semiconductor material in certain device depends on the required band gap value. Furthermore, tuning the band gap size of a semiconductor opens up opportunity to extend its potential application. For the past many years, the creation of an isolated defects such as vacancies and doping was popularly used to tailor the properties of the 3D bulk semiconductors [39, 40, 41]. Defects can be a source of *n*- or *p*-type materials that are essential elements for the fabrication of electronic and optoelectronic devices. Inducing defects in the MoS_2 monolayer is attractive because of its 2D nature, making it easy to reach the target atom. It has been established that the isolated defect effectively alters the electronic properties of a MoS_2 monolayer towards the desired application [42, 43, 44]. The doping with various elements of the periodic table in a MoS_2 monolayer has been broadly investigated [42, 43, 45]. Nevertheless, the study of the effect of foreign atoms can be extended to high concentration known as alloying. This technique has been reported to be an effective way to achieve a continuously tunable band gap in a material. As seen earlier, a large number of TMD materials have been predicted to be stable in 2D structure. Owing to the similarity in crystallographic structures, the alloying between any 2D TMD material and the MoS_2 monolayer is feasible [46]. This will expand the range, and improve the efficiency of the 2D MoS_2 applications.

The alloying of a MoS_2 monolayer at both transition metal (Mo) and chalcogen (S) sublattices were theoretically and experimentally studied [47, 48, 49, 50, 51]. For the Mo site, the alloying with the transition metal tungsten (W) atom have attracted a lot of attentions due to the good lattice mismatch between the WS_2 and MoS_2 monolayers. The

theoretical study using a density functional theory (DFT) method predicts an exothermic formation of this alloy at each concentration. In other words, the $Mo_{1-x}W_xS_2$ alloys are thermodynamically stable and can be synthesized at ambient temperature [37]. Many experimental works have supported this theoretical prediction by successfully synthesizing the $Mo_{1-x}W_xS_2$ alloys at different concentrations [47, 50, 51]. The photoluminescence (PL) experiments, in agreement with the density of state (DOS) analysis show that the W alloying is an efficient way to engineer the band gap of a MoS_2 monolayer continuously. The MoS_2 monolayer based alloy material has shown the fascinating properties suitable for application in photodetection with a response time shorter than 150 ms [50].

On the other hand, the possibilities of creating alloy at S site (chalcogen) of the MoS_2 monolayer has been theoretically investigated by replacing the S atom with Se and Te atoms. These chalcogen alloys are thermodynamically stable, indicating that they can be synthesized at room temperature [37]. Experimentally, they are successfully prepared using different methods such as mechanical exfoliation or by controlling the S and Se (Te) ratio using CVD method [48]. Due to their peculiar properties [37, 47, 48, 50, 51], these MoS_2 monolayer alloyed with chalcogen atoms are promising materials for the practical applications. In the case of electronic properties in particular, the chalcogen Se and Te atoms fine tune the band gap of the MoS_2 monolayer with a range of 1.8 eV (band gap of pristine MoS_2) to 1.55 eV (band gap of pristine $MoSe_2$) and 1.05 eV (band gap of pristine $MoTe_2$) respectively. These band gap values correspond to the red section of the visible spectrum and the infrared region respectively [37, 48]. These characteristics give the opportunity for the MoS_2 alloyed materials to be used in solar cells, radiation detector and gas sensor devices [37, 46]. Furthermore field effect transistor (FET) using a MoS_2 monolayer alloyed with the Se atoms have been fabricated [47] and exhibits a relatively high on/off ratios of 10^6 [46, 47]. This alloy also shows a high sensitivity of up to 800 AW^{-1} [46] and response times of a few

seconds [46, 50] making it a good candidate for photodetector devices.

The research on the band gap engineering of a MoS_2 monolayer through alloying is still in its infancy stage, and there are still many possibility worth to be studied. To date, the three elements W, Se and Te atoms are the most popular used to tailor the properties of the MoS_2 monolayer through alloying. Referring to the periodic table, the W atom is found below the Mo atom in the VIb periodic group. Similarly, the Te and Se atoms are below the S atom in the chalcogen group. The structural analysis of the MoS_2 monolayer alloyed with these elements showed that the lattice constant increases linearly with respect to the concentration [51]. This is due to the large atomic radius of the W (Se and Te) atom compared to the Mo (S) atom. However, the effect of the foreign atoms with small atomic radii such as chromium (Cr) and oxygen (O) on the properties of the MoS_2 monolayer is still a remaining question, and deserves to be considered in the study of a MoS_2 monolayer alloying in order to expand its applications.

In addition, the most critical question in alloying is how the atoms in the lattice are distributed since the atomic arrangement plays an important role in the electronic structures of alloyed materials. Larsen *et al*. [52] showed five models of the possible alloying configurations in a hexagonal lattice, namely ordered, random (disordered), clustered, lines and triplets. The most studied alloying shape in experimental and theoretical works is the random configuration [25, 37, 48, 51]. Few studies have also reported the formation and properties of ordered alloy in a MoS_2 monolayer at 0K [48, 53]. In principle, the study of the different possible alloy configurations at each concentration gives a new choice of material to achieve the nanotechnological devices based on 2D materials. To the best of our knowledge, a systematic study of the possible line-ordered alloy configurations at each concentration is missing in the literature.

1.2 Aims and objectives

As mentioned earlier, the MoS_2 monolayer alloyed with W, Te and Se atoms have been widely studied, and have presented promising success in further practical application. Looking at the periodic table, the Cr atom is a transition metal belonging to the same group as W and Mo atoms. However, there is no detailed study of Cr alloying in a MoS_2 monolayer. Although the lattice constant of the CrS_2 monolayer is slightly smaller than that of the MoS_2 monolayer, they have the same hexagonal crystal structure, and their lattice mismatch can be negligible. This motivated the investigation in the first part of this thesis to study the band gap engineering of the MoS_2 monolayer through Cr alloying, and also to study the effect of Cr atom having smaller atomic radius than Mo atom on the energetics and structural properties. Moreover, the chalcogen group including O, S, Te, Se and the radioactive element polonium (Po) atoms is also called "oxygen family". Similarly, we noticed that the band gap engineering of a MoS_2 monolayer through O atom having smaller atomic radius than S atom, has not yet been investigated previously. The new 2D transition metal oxides (TMO) such as a molybdenum dioxide (MoO_2) monolayer have lately been theoretically predicted to be stable, and have the same crystal structure as a MoS_2 monolayer [21, 22]. The transition through alloying from a MoS_2 monolayer to MoO_2 monolayer is given in detail in the second part of this thesis. The synthesis of the MoS_2 monolayer alloyed with the Te atoms has not yet extensively explored. Therefore, a detailed theoretical understanding of the thermodynamic stability, structural and electronic properties of the various possible Te alloy configurations is essential for its fabrication, and is presented in this thesis.

In this thesis, the first-principles calculations using DFT were carried out to study the thermodynamic stability, structural and electronic properties of the MoS_2 monolayer alloyed with Cr, O and Te atoms for band gap engineering. The new and understudied alloy arrangement (line-ordered alloy) were identified and characterized. For

each study, the properties of the line-ordered alloy configuration are compared with those of the well-known random and/or cluster configurations. The main objectives of this thesis are:

- to identify all the possible line-ordered alloy configurations in the MoS_2 system. The number of the possible line-ordered alloy configurations for the alloying at Mo site is different to that of S site due to the presence of double layers of S atoms sandwiching the Mo layer.
- to examine the thermodynamic stability of these various line-ordered alloy configurations in order to predict the lowest energy configurations that might be suitable candidate structures for nanotechnological applications.
- to introduce the special quasirandom structure (SQS) method in order to generate the random alloy configurations in a MoS_2 monolayer.
- to investigate the effect of transition metal (Cr) and chalcogens (O, Te) atoms alloying on the structural properties of the MoS_2 monolayer. Usually, the variation of the lattice constant with respect to the concentration for an alloy system obeys Vegard's law.
- to examine the influence of the concentration and structural configuration of the Cr, O and Te atoms on the electronic properties of the semiconductor MoS_2 monolayer.
- to understand the origin (orbital contributions) of the band gap engineering in a MoS_2 monolayer through alloying based on partial density of states (PDOS) and charge density plots.
- to improve qualitatively the value of the tuned band gap using the HSE06 exchange-correlation functional since this functional is known to accurately predict the electronic properties of a material.

1.3 Synopsis

The Chapter 2 of this thesis unfolds with a literature review which summarizes various strategies that have been reported to efficiently modify the band gap of a MoS_2 monolayer. Chapter 3 provides the theoretical background behind the electronic structure simulations. A brief overview of the many body problem is introduced. Subsequently, DFT) which is one of the approximate solution to the many body problem, is described. Different exchange-correlation functionals including the standard DFT and the hybrid functionals are also discussed. Lastly, a description of the pseudopotentials used in this thesis is introduced in this chapter. Chapter 4 describes the effects of the Cr atoms at different concentrations on the properties of the MoS_2 monolayer. In the first part of this chapter, the effects of Cr atom at low concentration (single and two Cr dopants) with different atomic positions is considered. In the second part, a comparative study of the thermodynamic stability, structural and electronic properties of the Cr line-ordered and random alloys is introduced. Both chapter 5 and chapter 6 describe the chalcogen alloying at S sites of the MoS_2 monolayer. In chapter 5, the influence of the O alloying at different concentrations and with different shapes is discussed. Chapter 6 focuses on a systematic study of the MoS_2 alloyed with Te atoms by considering the line-ordered alloy configurations at each concentration. The properties of the line-ordered alloy are compared with those of random alloy since it has already been synthesized. Finally, all work are summarized and future work are presented in chapter 7.

Bibliography

[1] K. S. Novoselov, A. K. Geim, S. V. Morozov, D. Jiang, Y. Zhang, S. V. Dubonos, I. V. Grigorieva, A. A. Firsov, science 306 (5696) (2004) 666-669. [1, 2, 3]

[2] K. Zhang, Y. Feng, F. Wang, Z. Yang, J. Wang, Journal of Materials Chemistry C 5 (46) (2017) 11992-12022. [1, 2]

[3] K. F. Mak, C. Lee, J. Hone, J. Shan, T. F. Heinz, Physical review letters 105 (13) (2010) 136805. [1, 2]

[4] B. Radisavljevic, A. Radenovic, J. Brivio, i. V. Giacometti, A. Kis, Nature nanotechnology 6 (3) (2011) 147. [1, 2, 3, 4]

[5] K. Novoselov, D. Jiang, F. Schedin, T. J. Booth, V. V. Khotkevich, S. V. Morozov, and A. K. Geim, Proceedings of the National Academy of Sciences of the United States of America 102 (2005) 10451. [2]

[6] A. Geim, and K. S. Novoselov, Nature Materials 6 (2007) 183. [2]

[7] C. Lee, X. Wei, J. W. Kysar, science 321 (5887) (2008) 385-388. [2]

[8] F. Liu, P. Ming, J. Li, Physical Review B 76 (6) (2007) 064120. [2]

[9] A. S. Mayorov, R. V. Gorbachev, S. V. Morozov, L. Britnell, R. Jalil, L. A. Ponomarenko, P. Blake, K. S. Novoselov, K. Watanabe, T. Taniguchi, et al. Nano letters 11 (6) (2011) 2396-2399. [2]

[10] D. J. Merthe, V. V. Kresin, Physical Review B 94 (20) (2016) 205439. [2]

[11] S. J. Kim, K. Choi, B. Lee, Y. Kim, B. H. Hong, Annual Review of Materials Research 45 (2015) 63-84. [2]

[12] M. Terrones, A. R. Botello-M endez, J. Campos-Delgado, F. L opez-Ur as, Y. I. Vega-Cant u, F. J. Rodr guez-Mac as, A. L. El as, E. Munoz-Sandoval, A. G. Cano-M arquez, J.-C. Charlier, et al., Nano today 5 (4) (2010) 351-372. [2]

[13] E. P. Randviir, D. A. Brownson, C. E. Banks, Materials Today 17 (9) (2014) 426-432. [2]

[14] L. H. Li, Y. Chen, Advanced Functional Materials 26 (16) (2016) 2594-2608. [2]

[15] K.M. McCreary, A.T. Hanbicki, J.T. Robinson, E. Cobas, J.C. Culbertson, A.L. Friedman, et al., Advanced Functional Materials, 24 (2014), pp. 6449-6454. [2]

[16] Z. He, W. Que, Applied Materials Today 3 (2016) 23-56. [2]

[17] S. Manzeli, D. Ovchinnikov, D. Pasquier, O. V. Yazyev, A. Kis, Nature Reviews Materials 2 (8) (2017) 17033. [2]

[18] R. Irshad, K. Tahir, B. Li, Z. Sher, J. Ali, S. Nazir, Journal of Industrial and Engineering Chemistry 64 (2018) 60-69. [2]

[19] H. Oughaddou, H. Enriquez, M. R. Tchalala, H. Yildirim, A. J. Mayne, A. Bendounan, G. Dujardin, M. A. Ali, A. Kara, Science 90 (1) (2015) 46-83. [2]

[20] J. Zhao, H. Liu, Z. Yu, R. Quhe, S. Zhou, Y. Wang, C. C. Liu, H. Zhong, N. Han, J. Lu, Y. Yao, K. Wu, Progress in Materials Science 83 (2016) 24-151. [2]

[21] F. A. Rasmussen, K. S. Thygesen, The Journal of Physical Chemistry C 119 (23) (2015) 13169-13183. [2, 8]

[22] C. Ataca, H. Sahin, S. Ciraci, The Journal of Physical Chemistry C 116 (16) (2012) 8983-8999. [2, 8]

[23] S. Bertolazzi, J. Brivio, A. Kis, ACS nano 5 (12) (2011) 9703-9709. [2, 4, 5]

[24] X. Li, H. Zhu, Journal of Materiomics 1 (1) (2015) 33-44. [3, 4]

[25] Z. Wang, B. Mi, Environmental science technology 51 (15) (2017) 8229-8244. [3, 7]

[26] D. B. Putungan, J.-L. Kuo, Integrated Ferroelectrics 156 (1) (2014) 93-101. [3]

[27] Ganatra, Q. Zhang, ACS nano 8 (5) (2014) 40744099. [4]

[28] Z. Zeng, Z. Yin, X. Huang, H. Li, Q. He, G. Lu, F. Boey, H. Zhang, Angewandte Chemie 123 (47) (2011) 11289-11293. [4]

[29] J. N. Coleman, M. Lotya, A. ONeill, S. D. Bergin, P. J. King, U. Khan, K. Young, A. Gaucher, S. De, R. J. Smith, et al., Science 331 (6017) (2011) 568-571. [4]

[30] Y.-H. Lee, X.-Q. Zhang, W. Zhang, M.-T. Chang, C.-T. Lin, K.-D. Chang, Y.-C. Yu, J. T.-W. Wang, C.-S. Chang, L.-J. Li, et al., Advanced materials 24 (17) (2012) 2320-2325. [4]

[31] Y. Yu, C. Li, Y. Liu, L. Su, Y. Zhang, L. Cao, Scientific reports 3 (2013) 1866. [4]

[32] Y.-C. Lin, W. Zhang, J.-K. Huang, K.-K. Liu, Y.-H. Lee, C.-T. Liang, C.-W. Chu, L.-J. Li, Nanoscale 4 (20) (2012) 6637-6641. [4]

[33] K.-K. Liu, W. Zhang, Y.-H. Lee, Y.-C. Lin, M.-T. Chang, C.-Y. Su, C.-S. Chang, H. Li, Y. Shi, H. Zhang, et al., Nano letters 12 (3) (2012) 1538-1544. [4]

[34] S. Wu, C. Huang, G. Aivazian, J. S. Ross, D. H. Cobden, X. Xu, ACS Nano 7 (3) (2013) 2768-2772. [4]

[35] A. Splendiani, L. Sun, Y. Zhang, T. Li, J. Kim, C.-Y. Chim, G. Galli, F. Wang, Nano letters 10 (4) (2010) 1271-1275. [4]

[36] G. Eda, H. Yamaguchi, D. Voiry, T. Fujita, M. Chen, M. Chhowalla, Nano letters 11 (12) (2011) 5111-5116. [4]

[37] H.-P. Komsa, A. V. Krasheninnikov, The journal of physical chemistry letters 3 (23) (2012) 3652-3656. [4, 6, 7]

[38] J. Pu, Y. Yomogida, K.-K. Liu, L.-J. Li, Y. Iwasa, T. Takenobu, Nano letters 12 (8) (2012) 4013-4017. [5]

[39] F. L. Thiel, S. K. Ghandhi, Journal of Applied Physics 41 (1) (1970) 254-263. [5]

[40] S. Noor Mohammad, M. Abdus Sobhan, physica status solidi (b) 156 (1) (1989) 287-302. [5]

[41] H. Sugimoto, M. Fujii, K. Imakita, S. Hayashi, K. Akamatsu, The Journal of Physical Chemistry C 117 (22) (2013) 11850-11857. [5]

[42] K. Dolui, I. Rungger, C. D. Pemmaraju, S. Sanvito, Physical Review B 88 (7) (2013) 075420. [5]

[43] Y. Li, Y.L. Li, C. M. Araujo, W. Luo, R. Ahuja, Catalysis Science & Technology 3 (9) (2013) 2214-2220. [5]

[44] D. Pierucci, H. Henck, Z. Ben Aziza, C. H. Naylor, A. Balan, J. E. Rault, M. G. Silly, Y. J. Dappe, F. Bertran, P. Le F‘evre, et al. ACS nano 11 (2) (2017) 1755-1761. [5]

[45] S.-C. Lu, J.-P. Leburton, Nanoscale research letters 9 (1) (2014) 676. [5]

[46] L. Xie, Nanoscale 7 (44) (2015) 1839218401. [5, 6, 7]

[47] Q. L. Feng, N. N. Mao, J. X. Wu, H. Xu, C. M. Wang, J. Zhang and L. M. Xie, ACS Nano, 2015, 9(7), 7450-7455. [5, 6]

[48] Y. Chen, J. Xi, Y. chen, D. O. dumcenco, Z. Liu, K. Suenaga, D. Wang, Z. Shuai, Y.-S. Huang, and L. Xie, ACS Nano 7 (2013) 4610. [5, 6, 7]

[49] V. Klee, E. Preciado, D. Barroso, A. E. Nguyen, C. Lee, K. J. Erickson, M. Triplett, B. Davis, I. H. Lu, S. Bobek, J. McKinley, J. P. Martinez, J. Mann, A. A. Talin, L. Bartels and F. Leonard, Nano Letters, 2015, 15, 2612-2619. [5]

[50] J. Yao, Z. Zheng, G. Yang, ACS applied materials interfaces 8 (20) (2016) 12915-12924. [5, 6, 7]

[51] J. Kang, S. Tongay, J. Li, J. Wu, Journal of Applied Physics 113 (14) (2013) 143703. [5, 6, 7]

[52] P. M. Larsen, A. R. Kalidindi, S. Schmidt, C. A. Schuh, Acta Materialia 139 (2017) 254-260. [7]

[53] W. Tan, Z. Wei, X. Liu, J. Liu, X. Fang, D. Fang, X. Wang, D. Wang, J. Tang, X. Fan, Scientific Reports 7 (1) (2017) 15124. [7]

Chapter 2

Review of previous work

In this chapter, previous experimental and theoretical work on band gap engineering in a MoS_2 monolayer are reviewed. Unlike semimetallic graphene, MoS_2 monolayer is a semiconductor material with a sizable band gap ($\sim$ 1.9 eV). Controlling the band gap of the MoS_2 monolayer is necessary for nanotechnological operation devices. Various techniques have been reported to successfully modify the band gap of the MoS_2 monolayer. In this chapter, the influence of defects such as vacancies, doping, and alloying at the molybdenum (Mo) and sulfur (S) sites on the electronic struture of the MoS_2 monolayer are discussed.

2.1 Defects in a MoS_2 monolayer

Usually, defects affect the characteristics of a host material in a way that can be beneficial or harmful to the material, depending on the application. They can enhance the electronic and magnetic properties of a host material to meet the specific requirement for nanotechnological applications.

Just like in real materials, native defects such as vacancies and antisites in a MoS_2 monolayer are inevitable during the synthesis. Different synthesis methods create dif-

ferent types of defects [1]. It was reported that the mechanical exfoliation and chemical vapor deposition (CVD) methods are responsible for the S vacancies, while Mo antisites are observed from the physical vapor deposition (PVD) samples [1, 2]. The atomic-resolution annular dark field (ADF) imaging on an aberration-corrected scanning transmission electron microscope (STEM) reveals single and double S vacancies, vacancy complex (formed by Mo atom and nearest S atoms) and antisites on the samples. It has been reported that S vacancies are frequently noted in the MoS_2 samples, while the other defects are rarely observed [2, 3]. First-principles calculations predict that S vacancies are more energetically stable than the double vacancies, vacancy complex, antisites [2] and Mo vacancy [4]. Moreover, Komsa *et al.* [5] performed first-principles calculations to study the formation of various intrinsic defects such as adsorption, vacancies and antisites under different condition limits. It was confirmed that S vacancies are the most abundant defects, especially in the Mo-rich conditions supporting experimental works [1, 2]. The presence of these defects modifies the electronic properties of the pristine MoS_2 monolayer. The density of states (DOS) analysis showed that the S vacancies induce deep states in the band gap [4, 5, 6]. A single S vacancy has a defect state at $\sim$0.6 eV below the conduction band minimum (CBM) [2, 4] caused by the Mo dangling bonds, and also a shallow state near the valence band maximum (VBM) due to the reduction in hybridization of the Mo $4d$ and S $3p$ orbitals [4]. These stable defects can be beneficial for controlling the properties of a MoS_2 monolayer in order to achieve good nanoelectronic devices.

Besides single vacancy, high-resolution transmission electron microscopy (HRTEM) experiments revealed that it is possible to create line vacancy defects (after 818 s of irradiation) [7]. Performing an electron irradiation in a MoS_2 monolayer at room temperature, various S vacancies are created, spontaneously moved and agglomerated to form line vacancies [7]. Two types of S line vacancies are observed: a single and double S line vacancies [7]. Furthermore, density functional theory (DFT) calculations

were used to study the electronic properties of these vacancy systems. The DOS of the single line vacancy showed that the system remains a semiconductor with a small band gap of 0.5 eV. This is due to the large unoccupied states induced within the band gap. However, the double line vacancy completely closes the band gap revealing a strong metallic character.

Thermodynamic stability and electronic property calculations of single and double S line vacancies along the armchair (AC) and zigzag (ZZ) directions in a MoS_2 monolayer were further performed [8]. It was found that the configurations with ZZ-types are more thermodynamically stable than the AC-types, supporting the TEM images [7]. On the other hand, a ZZ double line vacancy has low formation energy compared to the ZZ single line vacancy, revealing that the line vacancies prefer to be closed to each other. Furthermore, the DOS analysis showed that both line defects configurations alter the electronic properties of the MoS_2 monolayer. The single and double line vacancies of AC-types fine-tune the band gap of the MoS_2 monolayer by reducing its value. The *d* orbitals of the Mo atoms at the S line vacancy are found to be responsible for this band gap narrowing [8]. Their corresponding ZZ-types close the band gap (metallic character). These results will be very helpful for designing nanoelectronics and nanoelectromechanics devices.

Defects can also be created by introducing foreign atoms through substitutional doping at S and Mo sites. Finding the appropriate dopants for nanotechnological applications is crucial in the study of a MoS_2 monolayer. For the substitutional doping at Mo sites, several dopants have already been studied experimentally and theoretically, including manganese (Mn) [9], niobium (Nb) [10], iron (Fe) [11], rhenium (Re) [3] and gold (Au) [3].

Suh *et al.* [10] studied a Nb doping on a MoS_2 monolayer via chemical vapor transport (CVT) synthesis at a growth temperature of 935°C. The structural analysis using an extended X-ray absorption fine structure (EXAFS) confirmed that the Nb

atoms successfully substitute the Mo atoms. It was found that the doped system has a p-type characteristic. Theoretically, Dolui *et al.* [12] also observed this p-type behavior of Nb-doped MoS_2 monolayer through the DOS plots. To demonstrate the application of the Nb-doped MoS_2 monolayer, Suh *et al.* [10] fabricated a van der Waals p-n homojunctions of this doped material with an undoped MoS_2 monolayer. The fabricated field effect transistor (FET) using the later material exhibits an enhanced current densities and tunable junction currents.

Lin *et al.* [3] synthesized the Re- and Au-doped MoS_2 monolayer using a CVT growth. A STEM imaging showed Re occupying Mo site, while Au is noted above the layer. The Re substitution over the Mo sites is favorable while substituting Mo atoms with Au atoms is found to be unfavorable, based on formation energy analysis. Their experimental results reconciled very well with the DFT formation energies. The local densities of states (LDOS) near the dopant atoms were also evaluated for all experimentally obtained configurations. Re dopants substituting Mo atoms give a n-type material since it has an excess of electrons compared to the Mo atoms. This is in good agreement with the theoretical observation by Dolui *et al.* [12]. In the case of Au dopants, an induced mid-gap state is observed, and yielded a n-type doping. It was suggested that the Re- and Au-doped MoS_2 monolayer can extend the applications in the fabrication of nanoelectronics devices. Additionally, an experimental study on Fe-doped MoS_2 monolayer [11] showed a n-type character. The frequency-dependent photoconductivity measurements indicated that Fe dopants introduced a deep states at 1.2 eV above the VBM within the band gap.

On the same substitutional site (at Mo sites), Zhang *et al.* [9] fabricated a manganese (Mn)-doped MoS_2 monolayer using a CVD method. The photoluminescence (PL) spectra analysis showed that the Mn atoms shift the valence band edge of the MoS_2 monolayer by 150 meV from 0.76 to 0.61 eV. This reveals that the Mn atoms alter the electronic properties of the MoS_2 monolayer. Lu *et al.* [13] performed spin-polarized

DFT calculations to study the electronic and magnetic properties of Mn, Fe, and Co atoms at Mo sites. Mn-doped MoS_2 monolayer is the most favorable configuration. It creates an impurity state near the CBM, at a 0.48 eV from Fermi level. Interestingly, it has the most localized spin distribution with a total magnetic moment of 1 μB [13]. Subsequently, they also considered vanadium (V), tantalum (Ta) and Nb at Mo sites. The Ta configurations are the most energetically stable with negative formation energy values as opposed to V and Nb atoms with positive formation energy [13]. Ta configurations are good p-type dopant candidates suitable for various electronic applications. Since Ta has one valence electron less than Mo atom, a magnetic moment of 1 μB was observed [13]. The magnetic properties of Mn- and Ta-doped MoS_2 monolayer make them good candidates for spintronics applications.

Similar to the Mo sites, substitutional doping at the S sites has been experimentally studied [14]. Momose *et al.* [14] conducted Phosphorus (P) doped MoS_2 thin films using CVD technique. The P atom acts as an acceptor dopant in the MoS_2 monolayer. The P-doped MoS_2 monolayer has a relatively high mobility with a Hall-mobility of 0.53 cm^2/Vs and a field-effect mobility of 43 cm^2/Vs [14]. This reveals that P-doped MoS_2 monolayer is a promising material to achieve devices with high performance.

The theoretical studies of doping at S sites have been widely studies [12, 13, 15]. Dolui *et al.* [12] performed a DFT calculation to study the electronic properties of doped MoS_2 monolayer. Fluorine (F), chlorine (Cl), bromine (Br), iodine (I), nitrogen (N), phosphorus (P) and arsenic (As) atoms were introduced at the S sites. Extreme growth conditions of these dopants were considered. For these dopants considered, positive formation energies were obtained under the S-rich limit, whereas negative values were achieved under the Mo-rich limit. P and As atoms induce gap states near the VBM [12, 13]. It was suggested that the later are promising candidates to achieve a p-type doping and can be used as hole-carriers to improve the conductivity of this semiconductor. The halogens, as expected, are n-type dopants inducing a deep gap

state at about 0.4 eV above the CBM. Therefore, n-type doping for a MoS_2 monolayer seems to be not possible for all S substitutions considered. Generally, the aim of the doping strategies for a MoS_2 monolayer is to find new materials used in 2D devices manufacturing with high performance.

The electronic and magnetic properties of several impurities such as carbon (C), silicon (Si), germanium (Ge), boron (B), aluminium (Al) and gallium (Ga) atoms at S sites have been investigated by Lu *et al.* [13]. For the stability analysis, it was found that B and C dopants have the lowest formation energies. The C atom induce a mid-gap state above the Fermi level while B doping introduces impurity states located near the VBM. For the magnetic properties, although C atom has a deficit of two valence electrons per atom compared to the S atoms, the system remains nonmagnetic because these two electrons have opposite spins. For B doping, a magnetic moment of 1 μB arises from the one remaining unpaired electron. This study can give an insight to the use of doped MoS_2 monolayer in spintronic applications.

O-doped MoS_2 monolayer was conducted by Krivosheeva *et al.* [15] using *ab initio* simulation. The structural analysis of the O substitutional doping showed that the crystal structure of the host system is preserved. The O atom reduces the band gap of the MoS_2 monolayer from 1.86 eV to 1.64 eV using Perdew, Burke, Ernzerhof (PBE) functional. They further considered adsorbed O atom above one of the S atoms on the top layer. It also reduces the band gap of the pristine up to 0.98 eV. However, an O atom adsorbed in the center of the hexagon yields metallic character. The oxygen plasma processing is suggested to be an efficient way for such band-gap engineering.

Generally, isolated defects in the pristine MoS_2 monolayer provide new insights into the thermodynamically stability, structural and electronic properties of this transition metal dichalcogenides (TMD) material. The 2D MoS_2 is the most promising semiconductors among the existent 2D TMD monolayers, therefore it is expected that the introduction of defects in this system will play an important role in its application for

electronic, spintronic and optoelectronic devices.

2.2 Alloying at Mo and S sites of a MoS_2 monolayer

In the history of material science, alloying has been used as an efficient way to tune the electronic properties of the semiconductor materials. Alloying in a TMD monolayer especially in a MoS_2 monolayer has been widely studied experimentally and theoretically. Similar to doping, alloying can be created at the Mo or S sites of the MoS_2 monolayer.

2.2.1 Alloying at Mo sites

In the case of Mo sites, the MoS_2 monolayer alloyed with tungsten (W) is the most popular one studied thus far. It has been synthesized using mechanical exfoliation [16] and the CVD method [17]. Usually, the electronic structures of the alloy materials greatly depend on the atomic arrangement such as random, ordered and clustered. STEM is usually used to analyze the distribution of the W atoms on the $Mo_{1-x}W_xS_2$ monolayer alloys [16, 17]. The imaging revealed a random arrangement of the W atoms in the $Mo_{1-x}W_xS_2$ monolayer alloys [16, 17, 18]. The Raman spectroscopy results showed a one-mode behavior corresponding to a random arrangement [17, 18]. The electronic properties of the $Mo_{1-x}W_xS_2$ monolayer were further investigated with a PL experiment. A continuous shift of the PL emission wavelengths was observed as the concentration of W atoms increases [16] revealing that the band gap of the MoS_2 monolayer is monotonously increased. The band gap values change from 1.83 eV ($x = 0.0$) to 1.99 eV ($x = 1$) [16, 18].

Beside the W atom, the Re and Cr atoms alloyed with 2D MoS_2 have also been synthesized at low concentration. $Mo_{1-x}Re_xS_2$ monolayer were successfully synthesized by Al-Dulaimi *et al.* [19] via aerosol assisted chemical vapour deposited (AACVD). The energy-dispersive X-ray (EDX) spectroscopy and inductively coupled plasma optical

emission spectroscopy (ICP-OES) confirmed that the Re atoms are successfully introduced into the MoS_2 monolayer. The structure of the $Mo_{1-x}Re_xS_2$ monolayer were thereafter investigated using a STEM apparatus. The imaging showed a homogeneous mixture of the Mo and Re atoms during the synthesis of a $Mo_{1-x}Re_xS_2$ monolayer but the morphology of the sample depends on the concentration of Re atoms. A cluster structure was observed for 1.79% while a feather-like crystal was obtained with higher Re concentration. Lewis *et al.* [20] also introduced chromium (Cr) atoms into the MoS_2 using an AACVD method. The nanosheets $Mo_{1-x}Cr_xS_2$ were formed by liquid-phase exfoliation. The presence of Cr in the MoS_2 nanosheets were confirmed using a EDX spectroscopy.

DFT calculations have been performed to study the effect of alloying on the stability, structural and electronic properties of a MoS_2 monolayer [16, 17, 21, 22, 23]. Mostly random distributions of the W atom in the MoS_2 monolayer are considered [16, 22]. The free energy of mixing of these alloys was found to be negative [21, 22] revealing that the $Mo_{1-x}W_xS_2$ alloyed monolayers are energetically stable. It was confirmed that random $Mo_{1-x}W_xS_2$ monolayer can be synthesized using mechanical exfoliating or the CVD method [16]. The DOS and bandstructure analysis showed that the alloyed systems remain semiconductors at each concentration but the band gap is increased from 1.82 eV to 1.99 eV [16, 17, 21, 23]. This band gap engineering originates from the hybridization of W and Mo *d*-orbitals at the band edges [16].

The structural properties of a $Mo_{1-x}W_xS_2$ monolayer were intensively studied by Gan *et al.* [24] using the combination of DFT, empirical model and Monte Carlo simulations. Both random and ordered configurations were identified during this study. The empirical model predicts ordered alloys at $x = 1/3$ and $2/3$ concentrations. Furthermore, to investigate the temperature dependance of the atomic distribution, Monte Carlo simulations were performed. It was found that the W monomer concentration increases with the decrease in temperature. It reveals that $Mo_{1-x}W_xS_2$ ordered alloys

can only appear at low temperatures. This results is in agreement with the experimental observation stating the synthesis of random distribution of $Mo_{1-x}W_xS_2$ monolayer at high temperature [16]. These studies suggest the possibility of obtaining different alloys at specific temperatures.

2.2.2 Alloying at S sites

For alloying at the S sites, the selenium (Se) and tellurium (Te) alloys are most popular studied. There are different techniques to synthesize the $MoS_{2(1-x)}Se_{2x}$ monolayer: by mechanical exfoliation from the $MoS_{2(1-x)}Se_{2x}$ bulk alloy [25] or by controlling the ratio of S and Se atoms [26, 27, 28, 29]. In this regard, Ma *et al.* [29] synthesized the $MoS_{2(1-x)}Se_{2x}$ monolayer using a simple sputtering-based method. The S atoms of a MoS_2 monolayer grown using CVD were removed via exposure of the sample to a 500V Ar^+-beam. Thereafter, the Se atoms substituted the S vacancies through evaporation of Se powder from a glass capillary. In the other side, Su *et al.* [28] synthesized the $MoS_{2(1-x)}Se_{2x}$ by selenization of the as-grown MoS_2 monolayer in a hot-wall furnace. The X-ray photoelectron spectroscopy (XPS) images [29] revealed the successful incorporation of the Se atoms into the MoS_2 monolayer [28, 29]. The properties of the MoS_2 monolayer can be controlled by the selenization temperatures 600°C, 700°C, 800°C and 900°C.

Feng *et al.* [26, 27] presented a different technique to synthesize this 2D semiconductor alloy. The $MoS_{2(1-x)}Se_{2x}$ monolayer was prepared by direct vaporization of the MoS_2 and $MoSe_2$ powders using a SiO_2/Si as substrates and annealed at 800°C. The atomic-resolution high-angle ADF STEM imaging shows that the S and Se atoms are distributed randomly in the 2D alloy system. By controlling the growth conditions, it was found that the morphology of the 2D alloys depends on the deposition temperature but not on the composition [27]. A large-area of up to 20 μm of $MoS_{2(1-x)}Se_{2x}$ monolayer alloys were achieved with a different concentration of Se atoms [27]. This

study is beneficial for manufacturing a large-area optoelectronic devices.

Gong *et al.* [30] also reported the synthesis of a MoS_2 monolayer alloyed with Se atoms at different concentrations. The 2D alloys were directly grown on a SiO_2 substrate using CVD at ∼800°C. A mixture of S and Se powder was used as chalcogen sources and molybdenum oxide (MoO_3) powder as a source of Mo atoms. The single peak observed in the PL spectra of the MoS_2-alloyed with Se atoms sample indicates the homogeneous mixture of Se and S atoms on the sample.

The electronic properties of the $MoS_{2(1-x)}Se_{2x}$ monolayer can experimentally analyzed using a PL spectroscopy. The PL emission depicts a redshift ranging from 667 nm to 790 nm [26, 27, 30] with strong PL emissions. The band gap of the MoS_2 monolayer is fine-tuned from 1.86 eV to 1.57 eV [26]. This suggests that $MoS_{2(1-x)}Se_{2x}$ monolayer is a good candidate for a nanoelectronic devices.

Recently, Yin *et al.* [31] successfully synthesized a $MoS_{2(1-x)}Te_{2x}$ monolayer at different concentrations via a hydrogen-assisted post-growth CVD process. The STEM imaging indicates a random distribution of the Te atoms in the MoS_2 monolayer. The Te atoms fine-tunes the band gap of the MoS_2 monolayer with a range of about 0.7 eV.

Experimental studies of alloying at the S sites of the MoS_2 monolayer showed that random distribution can occur spontaneously at a sufficient growth conditions. PL analysis revealed that the band gap of the MoS_2 monolayer is fine-tuned by the composition of the alloy system. In the following section, a theoretical point of view of the chalcogen alloying is investigated.

Komsa *et al.* [21] performed first-principles studies to investigate the thermodynamic stability and electronic properties of random $MoS_{2(1-x)}Se_{2x}$ and $MoS_{2(1-x)}Te_{2x}$ monolayers. The formation energies for $MoS_{2(1-x)}Te_{2x}$ alloys are found to be positive while that ones of $MoS_{2(1-x)}Se_{2x}$ are negative. Generally, a MoS_2 monolayer alloyed with Se and Te atoms are favorable as their formation energy values are very low [21, 32]. The electronic properties of the alloyed materials were studied using an

effective band structure (EBS) approach [33]. It was shown that the band gap is continuously changed with the concentration of Te or Se atoms. In fact, it is fine-tuned in between the band gap value of the pristine MoS_2 monolayer and the corresponding band gap of the other TMD (i.e. $MoSe_2$ and $MoTe_2$). The obtained band gap values of the $MoS_{2(1-x)}Se_{2x}$ alloys rely mostly in the red part of the visible spectrum (1.65-2.0 eV) while the gaps for $MoS_{2(1-x)}Te_{2x}$ monolayers even reach the infrared region. Therefore, alloying TMD materials can be beneficial for optoelectronic applications. Rajbanshi *et al.* [32] gave a detailed study of the structural and electronic structure of the monolayer $MoS_{2(1-x)}Se_{2x}$ and $MoS_{2(1-x)}Te_{2x}$ random alloys. The structural analysis of these alloys revealed that the lattice constants increase with the increase in Se and Te concentrations due to their large atomic radii [32, 34]. The DOS analysis confirms the EBS study of Komsa *et al.* [21] that the concentrations fine-tune the band gap of the MoS_2 monolayer from 1.62 eV to 1.48 eV for the Se atoms and 1.62 eV to 1.04 eV for the Te atoms. Additionally, the band gap of $MoS_{2(1-x)}Se_{2x}$ nanosheets changes linearly with the Se concentration while that of $MoS_{2(1-x)}Te_{2x}$ deviates from linearity.

A particular theoretical study was performed by Kang *et al.* in Ref [34]. They showed that stable ordered alloy structures can be obtained with the $MoS_{2(1-x)}Se_{2x}$ alloys in a MoS_2 monolayer at 1/3, 1/2, and 2/3 concentrations. This is due to the lattice mismatch between the two chalcogens S and Se atoms, while no ordered stable configuration can be formed for $MoS_{2(1-x)}Te_{2x}$ alloys at zero Kelvin.

In this chapter, previous experimental and theoretical works using different techniques to fine-tune the band gap of a MoS_2 monolayer are reported. As seen previously, engineering the band gap of a MoS_2 monolayer through an isolated defect is extensively studied. In the case of alloying, the W atom occupying the Mo site, the Te and Se atoms occupying S sites are most popular studied. The transition metal atom W and the chalcogen atoms Se and Te are situated below the Mo and S atoms on the periodic table respectively. These atoms have slightly large atomic radii compared to

the host atoms. The studies of the influence of foreign atoms that have small atomic radii compared to the Mo or S atoms have not yet reported. These motivated this work to study the alloying of a MoS_2 monolayer with the atoms above the Mo and S atoms in the periodic table such as the transition metal Cr atom and the chalcogen O atom respectively. Furthermore, we also realize that the investigations of the band gap engineering are mostly considered with random distribution of the composition. There are other alloy shapes missing in the literature such as ordered, clustered, line and triplet (triangle-like) alloy configurations [35]. A knowledge of a consistent study of alloying in a MoS_2 monolayer with a particular shape at every concentration should be beneficial for its fabrications and applications. Therefore, a theoretical study of the thermodynamic stability, structural and electronic properties of the line-ordered alloy configurations at each concentration are systematically considered in this thesis. The results are compared with the other well-known shapes such as random and cluster configurations. Moreover, the previous works have studied the effects of alloying on the electronic properties of the MoS_2 monolayer using the standard DFT. We qualitatively improve the tuned band gap values of the alloyed systems using hybrid functional. In the next chapter, the theoretical background of DFT and its related implementations are discussed.

Bibliography

[1] J. Hong, Z. Hu, M. Probert, K. Li, D. Lv, X. Yang, L. Gu, N. Mao, Q. Feng, L. Xie, J. Zhang, D. Wu, Z. Zhang, C. Jin, W. Ji, X. Zhang, J. Yuan, and Z. Zhang, Nature Communications 6 (2015) 6293. [17]

[2] W. Zhou, X. Zou, S. Najmaei, Z. Liu, Y. Shi, J. Kong, J. Lou, P. M. Ajayan, B. I. Yakobson, J.-C. Idrobo, Nano letters 13 (6) (2013) 2615-2622. [17]

[3] Y.-C. Lin, D. O. Dumcenco, H.-P. Komsa, Y. Niimi, A. V. Krasheninnikov, Y.-S. Huang, K. Suenaga, Advanced Materials 26 (18) (2014) 28572861. [17, 18, 19]

[4] K. Santosh, R. C. Longo, R. Addou, R. M. Wallace, K. Cho, Nanotechnology 25 (37) (2014) 375703. [17]

[5] H.-P. Komsa, A. V. Krasheninnikov, Physical Review B 91 (12) (2015) 125304. [17]

[6] J.-Y. Noh, H. Kim, Y.-S. Kim, Physical Review B 89 (20) (2014) 205417. [17]

[7] H.-P. Komsa, S. Kurasch, O. Lehtinen, U. Kaiser, A. V. Krasheninnikov, Physical Review B 88 (3) (2013) 035301. [17, 18]

[8] Y. Han, T. Hu, R. Li, J. Zhou, J. Dong, Physical Chemistry Chemical Physics 17 (5) (2015) 3813-3819. [18]

[9] K. Zhang, S. Feng, J. Wang, A. Azcatl, N. Lu, R. Addou, N. Wang, C. Zhou, J. Lerach, V. Bojan, et al., Nano letters 15 (10) (2015) 6586-6591. [18, 19]

[10] J. Suh, T.-E. Park, D.-Y. Lin, D. Fu, J. Park, H. J. Jung, Y. Chen, C. Ko, C. Jang, Y. Sun, et al., Nano letters 14 (12) (2014) 6976-6982. [18, 19]

[11] S. Y. Wang, T. S. Ko, C. C. Huang, Y. S. Huang, et al., Japanese Journal of Applied Physics 53 (4S) (2014) 04EH07. [18, 19]

[12] K. Dolui, I. Rungger, C. D. Pemmaraju, S. Sanvito, Physical Review B 88 (7) (2013) 075420. [19, 20]

[13] S.-C. Lu, J.-P. Leburton, Nanoscale research letters 9 (1) (2014) 676. [19, 20, 21]

[14] T. Momose, A. Nakamura, M. Daniel, M. Shimomura, AIP Advances 8 (2) (2018) 025009. [20]

[15] A. V. Krivosheeva, V. L. Shaposhnikov, V. E. Borisenko, J.-L. Lazzari, C. Waileong, J. Gusakova, B. K. Tay, Journal of Semiconductors 36 (12) (2015) 122002. [20, 21]

[16] Y. Chen, J. Xi, Do Dumcenco, Z. Liu, K. Suenaga, D. Wang, Z. Shuai, Y.-S. Huang, and L. Xie, ACS Nano 7 (2013) 4610. [22, 23, 24]

[17] Z. Wang, P. Liu, Y. Ito, S. Ning, Y. Tan, T. Fujita, A. Hirata, M. Chen, Scientific reports 6 (2016) 21536. [22, 23]

[18] W. Zhang, X. Li, T. Jiang, J. Song, Y. Lin, L. Zhu, X. Xu, Nanoscale 7 (32) (2015) 13554-13560. [22]

[19] N. Al-Dulaimi, D. J. Lewis, X. L. Zhong, M. A. Malik, P. OBrien, Journal of Materials Chemistry C 4 (12) (2016) 2312-2318. [22]

[20] D. J. Lewis, A. A. Tedstone, X. L. Zhong, E. A. Lewis, A. Rooney, N. Savjani, J. R. Brent, S. J. Haigh, M. G. Burke, C. A. Muryn, et al., Chemistry of Materials 27 (4) (2015) 13671374. [23]

[21] H.-P. Komsa, A. V. Krasheninnikov, The journal of physical chemistry letters 3 (23) (2012) 3652-3656. [23, 25, 26]

[22] J. Xi, T. Zhao, D. Wang, Z. Shuai, The journal of physical chemistry letters 5 (2) (2013) 285-291. [23]

[23] A. Kuc, T. Heine, Electronics 5 (1) (2015) 1. [23]

[24] L.Y. Gan, Q. Zhang, Y.J. Zhao, Y. Cheng, U. Schwingenschl ogl Scientific reports 4 (2014) 6691. [23]

[25] C. Tan, W. Zhao, A. Chaturvedi, Z. Fei, Z. Zeng, J. Chen, Y. Huang, P. Ercius, Z. Luo, X. Qi, et al., Small 12 (14) (2016) 1866-1874. [24]

[26] Q. Feng, Y. Zhu, J. Hong, M. Zhang, W. Duan, N. Mao, J. Wu, H. Xu, F. Dong, F. Lin, et al., Advanced Materials 26 (17) (2014) 2648-2653. [24, 25]

[27] Q. Feng, N. Mao, J. Wu, H. Xu, C. Wang, J. Zhang, L. Xie, ACS nano 9 (7) (2015) 7450-7455. [24, 25]

[28] S.-H. Su, Y.-T. Hsu, Y.-H. Chang, M.-H. Chiu, C.-L. Hsu, W.-T. Hsu, W.-H. Chang, J.-H. He, L.-J. Li, Small 10 (13) (2014) 2589-2594. [24]

[29] Q. Ma, M. Isarraraz, C. S. Wang, E. Preciado, V. Klee, S. Bobek, K. Yamaguchi, E. Li, P. M. Odenthal, A. Nguyen, D. Barroso, D. Sun, G. Von Son Palacio, M. Gomez, A. Nguyen, D. Le, G. Pawin, J. Mann, T. F. Heinz, T. S. Rahman, and L. Bartels, ACS Nano 8 (2014) 4672. [24]

[30] Y. Gong, Z. Liu, A. R. Lupini, G. Shi, J. Lin, S. Najmaei, Z. Lin, A. L. El as, A. Berkdemir, G. You, et al., Nano letters 14 (2) (2013) 442-449. [25]

[31] G. Yin, D. Zhu, D. Lv, A. Hashemi, Z. Fei, F. Lin, A. V. Krasheninnikov, Z. Zhang, H.-P. Komsa, C. Jin, Nanotechnology 29 (14) (2018) 145603. [25]

[32] B. Rajbanshi, S. Sarkar, P. Sarkar, Physical Chemistry Chemical Physics 17 (39) (2015) 26166-26174. [25, 26]

[33] V. Popescu, A. Zunger, Physical review letters 104 (23) (2010) 236403. [26]

[34] J. Kang, S. Tongay, J. Li, J. Wu, Journal of Applied Physics 113 (14) (2013) 143703. [26]

[35] P. M. Larsen, A. R. Kalidindi, S. Schmidt, C. A. Schuh, Acta Materialia 139 (2017) 254-260. [27]

Chapter 3

Electronic structure methods

In this chapter, various theoretical methods used to study the electronic structure of real material systems are discussed. The material system treated in this thesis is classified as a many-body system. The problems associated with the electronic structure calculation of a many-body system are introduced. To solve these issues, different approaches have been developed in the past and are listed here. Firstly, we describe the Hartree method and Hartree-Fock (HF) method, and introduce their limitations. Next, the density functional theory (DFT) method is discussed in detail. The central part of the DFT method, which is the exchange-correlation functional, is discussed. Various flavors of the standard local density approximation (LDA) and generalized gradient approximation (GGA) exchange-correlation functionals are introduced and their failures are discussed. We also describe the hybrid exchange-correlation functionals that can more accurately predict the band gap of the insulating materials amongst other properties. In addition, a detailed description of the Kohn-Sham (KS) equations and their implementation are introduced. In the last section, the pseudopotential construction used in this thesis is described.

3.1 The many-body problem

In general, any real material is constituted by a dense number of electrons and nuclei. They interact with each other, and their interactions govern the properties of the material. Since we are dealing with electromagnetic interactions at the electronic level, the behaviour of the system is described by quantum mechanics. In this chapter, we ignore the impact of the relativistic effects. The fundamental equation that describes a quantum mechanical system is the many-body Schrödinger equation [1, 2] given by:

$$H\Psi = E\Psi, \tag{3.1}$$

where Ψ is the wavefunction, E is the energy and H is the Hamiltonian operator of the system. The latter is generally split into five terms:

$$H = T_I + T_e + V_{ee} + V_{II} + V_{eI} \tag{3.2}$$

where T_I and T_e are the kinetic energy operators for the electrons and ions respectively. The V_{ee}, V_{II} and V_{eI} terms are the potential energy operators describing the electron-electron, the ion-ion, and the ion-electron Coulomb interactions respectively

$$\begin{aligned} T_I &= -\hbar^2 \sum_I \frac{\nabla_I^2}{2M_I}, \\ T_e &= -\hbar^2 \sum_i \frac{\nabla_i^2}{2m_e}, \\ V_{ee} &= \frac{1}{2} \sum_{i \neq j} \frac{e^2}{|\mathbf{r}_i - \mathbf{r}_j|}, \\ V_{II} &= \frac{1}{2} \sum_{I \neq J} \frac{Z_I Z_J e^2}{|\mathbf{R}_I - \mathbf{R}_J|}, \\ V_{eI} &= -\sum_{i,I} \frac{Z_I e^2}{|\mathbf{r}_i - \mathbf{R}_I|} \end{aligned} \tag{3.3}$$

where the $\sum_{i,j}$ refer to the summations over electrons, and $\sum_{I,J}$ refer to the sum-

mations over the nuclei. The symbol ∇ in the kinetic energy terms refers to the spatial gradient operator. Z_I and M_I are the atomic number and mass of the ion respectively. $\mathbf{r}_i$ and $\mathbf{R}_I$ correspond to the three dimensional position vectors of the i^{th} electron and I^{th} ion respectively. The wavefunction Ψ depends on both the ionic and electronic degrees of freedom $\Psi(\mathbf{r}_i, \mathbf{R}_I)$ such that eqn. 3.1 is then written as

$$(T_I + T_e + V_{ee} + V_{II} + V_{eI})\Psi(\mathbf{r}_i, \mathbf{R}_I) = E\Psi(\mathbf{r}_i, \mathbf{R}_I) \tag{3.4}$$

The properties of a system can be obtained by finding the solution of the Schrödinger equation in eqn. 3.4, however solving this equation is not tractable. For instance, for a neutral system, if the material contains N nuclei, the number of interacting particles in the system is $N + \sum_{i=1}^{N} Z_i$; therefore approximation is necessary. The first approximation used is the Born-Oppenheimer (BO) approximation [3]. Since the mass of a nuclei is more than a few thousand times heavier than that of an electron [1] (the mass of a proton is 1800 times the mass of an electron), the electron moves relatively faster than the nuclei. Consequently, the BO approximation allows us to neglect the T_I term of the nuclei in eqn. 3.4. Fixing the position R_I of the nuclei, eqn. 3.4 becomes

$$\left(-\hbar^2 \sum_i \frac{\nabla_i^2}{2m_e} + \frac{1}{2}\sum_{i\neq j} \frac{e^2}{|\mathbf{r}_i - \mathbf{r}_j|} - \sum_{i,I} \frac{Z_I e^2}{|\mathbf{r}_i - \mathbf{R}_I|} + \frac{1}{2}\sum_{I\neq J} \frac{Z_I Z_J e^2}{|\mathbf{R}_I - \mathbf{R}_J|}\right)\Psi(\mathbf{r}_i) = E\Psi(\mathbf{r}_i). \tag{3.5}$$

Although the nuclei are considered as stationary particles, finding the solution of eqn. 3.5 is not an easy task due to the large number of electrons interacting with each other and also interacting with the immobile nuclei. Moreover, the wavefunction has to be antisymmetric due to the fermion nature of the electrons, making the calculations more complicated. Therefore, systematic methods are needed to solve this equation. The next section briefly introduces and describes the methods developed to

solve eqn. 3.5.

3.2 Hartree-Fock approximation

To reduce the complexity of eqn. 3.5, the Hartree approximation was proposed in 1928 [4] in which the many-body wavefunction $\Psi(\mathbf{r}_i)$ is considered as the product of the single independent electron wavefunctions [4], i.e,

$$\Psi(\mathbf{r}_i) = \psi_1(\mathbf{r}_1)\psi_2(\mathbf{r}_2)\psi_3(\mathbf{r}_3)...\psi_N(\mathbf{r}_N). \tag{3.6}$$

Thus, the problem is reduced to a single independent particle Schrödinger equation. Substituting eqn. 3.6 in eqn. 3.5 gives the Hartree equation [4] as

$$[T_e + V_{eff}]\psi_i(\mathbf{r}) = \varepsilon_i(\mathbf{r})\psi_i(\mathbf{r}) \tag{3.7}$$

$\varepsilon_i(\mathbf{r})$ is the ith electron energy eigenvalue. The first term T_e represents the one-electron kinetic energy and the second term V_{eff} is an effective potential given by

$$V_{eff} = V_{ext} + \sum_{i \neq j}^{N} \int \frac{d\mathbf{r}'}{|\mathbf{r} - \mathbf{r}'|} n_j(\mathbf{r}'). \tag{3.8}$$

The electron density $n_j(\mathbf{r})$ of the j^{th} particle is given by

$$n_j(\mathbf{r}) = |\psi_j(\mathbf{r})|^2. \tag{3.9}$$

V_{ext} in eqn. 3.8 indicates the interaction of one orbital with the other ions. The second term, also called Hartree potential ($V_{Hartree}$) [5] describes the potential due to the other electrons in a mean field way, i.e the electron at a position $\mathbf{r}$ sees the average distribution effect of the other electrons everywhere in the space. Eqn. 3.7 is solved by applying the self-consistent field method. In order to construct the electronic density,

the calculation must start by guessing an initial wavefunction that is necessary to build the effective potential V_{eff}. Now, eqn. 3.7 can be solved and provide a new set of eigenfunctions which, in its turn, becomes the inputs for the next step. We stop the cycle when the output and input wavefunctions, and hence charge densities are the same. However, the Hartree approximation presents a very important drawback. It assumes that electrons are distinguishable while electrons are fermions, swapping two electrons changes the functions.

This issue was addressed by Fock in 1930 [6]. He improved the Hartree approximation by considering the wavefunction as antisymmetric in order to obey the Pauli exclusion principle. It states that two electrons with the same spin cannot occupy the same quantum state. To ensure the latter, Fock introduced the notion of the Slater determinant [7] that is written as

$$\Psi(\mathbf{r}_i, s_i) = \frac{1}{\sqrt{N!}} \begin{vmatrix} \psi_1(\mathbf{r}_1, s_1) & \psi_1(\mathbf{r}_2, s_2) & \dots & \psi_1(\mathbf{r}_N, s_N) \\ \psi_2(\mathbf{r}_1, s_1) & \psi_2(\mathbf{r}_2, s_2) & \dots & \psi_2(\mathbf{r}_N, s_N) \\ \vdots & \vdots & \ddots & \vdots \\ \psi_N(\mathbf{r}_1, s_1) & \psi_N(\mathbf{r}_2, s_2) & \dots & \psi_N(\mathbf{r}_N, s_N) \end{vmatrix}. \tag{3.10}$$

We can transform this complex matrix representation into a simple form:
$\Psi = A\left[\psi_1, \psi_2, ..., \psi_N\right]$ where $A = \frac{1}{\sqrt{N!}} \sum_i (-1)^{\varepsilon(p)} P$. P is called a permutation operator.

Defining a one body operator O_1 and a two body operator O_2 as

$$\begin{cases} O_1 = \left[-\hbar^2 \sum_i \frac{{\nabla_i}^2}{2m_e} + V_{ext}(\mathbf{r}_i)\right] = \sum_{i=1}^{N} h(\mathbf{r}_i), \\ O_2 = \frac{1}{2} \sum_{i,j} \frac{e^2}{|\mathbf{r}_i - \mathbf{r}_j|} = \frac{1}{2} \sum_{i,j} w(\mathbf{r}_i, \mathbf{r}_j). \end{cases} \tag{3.11}$$

The expectation value of the Hamiltonian with the wavefunction given by eqn. 3.10 can be written as

$$< \Psi\,|H|\,\Psi > = < \Psi\,|O_1|\,\Psi > + < \Psi\,|O_2|\,\Psi >, \tag{3.12}$$

with

$$\begin{cases} < \Psi \,|O_1|\, \Psi > = < \Psi_1, \Psi_2, ..., \Psi_N | A^+ (\sum_{i=1}^{N} h(\mathbf{r}_i)) A | \Psi_1, \Psi_2, ..., \Psi_N > \\ < \Psi \,|O_2|\, \Psi > = < \Psi_1, \psi_2, ..., \Psi_N | A^+ (\frac{1}{2} \sum_{i,j} w(\mathbf{r}_i, \mathbf{r}_j)) A | \Psi_1, \Psi_2, ..., \Psi_N > . \end{cases} \tag{3.13}$$

In eqn. 3.10, the single particle spin-orbital wavefunction $\psi_i(\mathbf{r}_j, s_j)$ can be split into a spatial and spin term:

$$\psi_i(\mathbf{r}_j, s_j) = \psi_i^s(\mathbf{r}_j)\alpha_i(s_j) \tag{3.14}$$

After implementing some algebra, the expectation value of the Hamiltonian using the Slater determinant has the form:

$$\begin{aligned} \langle \Psi | H | \Psi \rangle = \quad & \sum_{i,s} \int d\mathbf{r}\, \psi_i^{s*}(\mathbf{r}) [T_e + V_{ext}]\, \psi_i^s(\mathbf{r}) \\ & + \frac{1}{2} \int n(\mathbf{r})\, \frac{1}{|\mathbf{r} - \mathbf{r}'|}\, n(\mathbf{r}')\, d\mathbf{r}\; d\mathbf{r}' \\ & - \frac{1}{2} \sum_{i,j,s} \int d\mathbf{r}\; d\mathbf{r}'\; \psi_i^{s*}(\mathbf{r})\, \psi_j^{s*}(\mathbf{r}') \frac{1}{|\mathbf{r} - \mathbf{r}'|}\, \psi_j^s(\mathbf{r}_i)\, \psi_i^s(\mathbf{r}'). \end{aligned} \tag{3.15}$$

The first term in eqn 3.15 is defined as the sum of kinetic energy and the external energy due to the frozen nuclei. The second term is the classical Coulomb energy known as Hartree energy and the third term is the exchange energy due to the Coulomb interaction between electrons of the same spin. A fraction of $\frac{1}{2}$ is added in order to avoid the double counting of the electrons. To simplify the expression of the energy, we use the atomic units $\hbar = m_e = e = 4\pi/\varepsilon_0 = 1$. Minimizing the energy expression in eqn. 3.15 by applying the variation theorem gives the ground state energy and leads to the single-electron Hartree-Fock (HF) equations [5] as

$$\left[-\frac{1}{2}\nabla^2 + V_{ext}(\mathbf{r}) + \int n(\mathbf{r}')\,\frac{1}{|\mathbf{r}-\mathbf{r}'|}d\mathbf{r}'\right]\psi_i^s(\mathbf{r}) + \int v_x(\mathbf{r},\mathbf{r}')\psi_i^s(\mathbf{r}')d\mathbf{r}' = \varepsilon_i^s(\mathbf{r})\psi_i^s(\mathbf{r}) \tag{3.16}$$

where v_x is the non-local exchange potential given by

$$\int v_x(\mathbf{r},\mathbf{r}')\psi_i^s(\mathbf{r}')d\mathbf{r}' = -\sum_j \int_{parallel\ spin} \psi_j^s(\mathbf{r})\,\psi_i^s(\mathbf{r}')\frac{1}{|\mathbf{r}-\mathbf{r}'|}\,\psi_j^{s*}(\mathbf{r}')d\mathbf{r}'. \tag{3.17}$$

The Pauli exclusion principle is correctly included in the HF approximation through the term v_x. To solve the HF equations (eqn. 3.16), a set of basis functions can be built so that eqn. 3.16 can be written as a function of the expansion coefficients for the orbitals. This is solvable for a system of relatively small such as single atom or molecular systems in quantum chemistry. Contrary, the application of the HF approximation in a large system is impracticable due to the requirement of a large number of electron basis functions (formally as N^4, N corresponds to the system size). Moreover, a very important failure of this approximation is the negligence of the correlations due to the many-body interactions, however, its effects on the energy of the system is not minimal. In the case of many-electron systems, the consideration of the correlations makes the problem very difficult to solve. HF approximation also fails to describe the properties of the homogeneous electron gas as well as metals. At the vicinity of the Fermi level, it predicts infinite velocities that results in a zero density of states (DOS) [8]. Generally, the HF method presents significant failures in the study of electronic structure of solids. Therefore, an approximation beyond the HF approximation that takes into account the correlation effects is needed to predict more accurately the properties of a material. The most popular method that includes both the exchange and the correlation effects is the DFT method.

3.3 Density functional theory

The DFT method is the most commonly used theory in condensed matter physics and quantum chemistry to describe the behavior of electrons in materials [9, 10]. It is the foundation of the majority of electronic structure calculation codes. Revisiting the HF method first, its solution to the Schrödinger equation is summarized as follow:

$V_{ext}(\mathbf{r}, \mathbf{R}) \implies \psi(\mathbf{r}, \mathbf{R})$ *and* $E(\mathbf{R}) \implies$ *Properties*

It starts with a 3N dimensional potential that is a function of the electronic position $\mathbf{r}$, followed by the construction of the Hamiltonian and the evaluation of the wavefunction and the energy. Thereafter, the information about the properties of the material can be obtained. In a HF calculation, the wavefunction (3N dimensional) is the central quantity to be solved. However, the DFT method has a different approach in its foundations compared to the HF approximation as described above. In DFT method, the electron density $n(\mathbf{r})$ plays the fundamental central role instead of the very complicated many-body wavefunction $\Psi(\mathbf{r})$. This conceptual difference reduces the problem from 3N dimensions to 3 dimensions.

$n(\mathbf{r}) \implies \psi(\mathbf{r}, \mathbf{R})$ *and* $E(\mathbf{R}) \implies$ *Properties*

The charge density $n(\mathbf{r})$ is defined as [2]

$$n(\mathbf{r}) = N \int |\Psi(\mathbf{r}, \mathbf{r}_2, \mathbf{r}_3, ..., \mathbf{r}_N)|^2 d^3r_2, d^3r_3, ...d^3r_N \tag{3.18}$$

subject to the constraint:

$$\int n(\mathbf{r}) d^3r = N \tag{3.19}$$

N is the total number of electrons.

The external potential contribution V_{ext} to the energy expectation value can be only

expressed in terms of the electron density $n(\mathbf{r})$.

$$
\begin{aligned}
< \Psi|V_{ext}(\mathbf{r})|\Psi > &=< \Psi| \sum_{i=1}^{N} V_{ext}(\mathbf{r}_i)|\Psi > \\
&= \int d^3r_1 d^3r_2 ... d^3r_N \ \Psi^*(\mathbf{r}_1, \mathbf{r}_2, ..., \mathbf{r}_N) \left[\sum_i^N V_{ext}(\mathbf{r}_i) \right] \Psi(\mathbf{r}_1, \mathbf{r}_2, ..., \mathbf{r}_N) \\
&= \sum_i^N \int d^3r_1 d^3r_2 ... d^3r_N \Psi^*(\mathbf{r}_1, \mathbf{r}_2, ..., \mathbf{r}_N) V_{ext}(\mathbf{r}_i) \Psi(\mathbf{r}_1, \mathbf{r}_2, ..., \mathbf{r}_N) \\
&= N \int d^3r V_{ext}(\mathbf{r}) \int d^3r_2 ... d^3r_N \, |\Psi(\mathbf{r}, \mathbf{r}_2, ..., \mathbf{r}_N)|^2 \\
\text{so,} \qquad < \Psi|V_{ext}(\mathbf{r})|\Psi > &= \int V_{ext}(\mathbf{r}) n(\mathbf{r}) d^3r
\end{aligned}
\tag{3.20}
$$

Generally, the DFT method is based on the two principal theorems of Hohenberg and Kohn [11]. The first theorem states that the ground state electron density $n(\mathbf{r})$ uniquely determine the external potential [5, 11] (and consequently the wavefunction, energies, etc.). The proof of this theorem is done by contradiction i.e adopting that the present theorem is incorrect. Suppose there are two potentials $V_{ext}^{(1)}$ and $V_{ext}^{(2)}$ that differ by more than a constant, and with the same ground state density.

$$
\begin{aligned}
\text{potential 1} : V_{ext}^{(1)} \quad &\Longrightarrow \quad \Psi^{(1)}(\mathbf{r}) \quad \Longrightarrow \quad n^{(1)}(\mathbf{r}) \\
\text{potential 2} : V_{ext}^{(2)} \quad &\Longrightarrow \quad \Psi^{(2)}(\mathbf{r}) \quad \Longrightarrow \quad n^{(2)}(\mathbf{r})
\end{aligned}
\tag{3.21}
$$

with $n^{(1)}(\mathbf{r}) = n^{(2)}(\mathbf{r})$

According to the Rayleigh-Ritz variational principle, the expectation value of $\Psi^{(1)}$ in Hamiltonian $H^{(1)}$ should be lower than that of $\Psi^{(2)}$, i.e.

$$
E^{(1)} = \langle \Psi^{(1)}|H^{(1)}|\Psi^{(1)}\rangle < \langle \Psi^{(2)}|H^{(1)}|\Psi^{(2)}\rangle. \tag{3.22}
$$

Hence,

$$\langle\Psi^{(1)}|H^{(1)}|\Psi^{(1)}\rangle = \langle\Psi^{(1)}|T|\Psi^{(1)}\rangle + \langle\Psi^{(1)}|V_{ee}|\Psi^{(1)}\rangle + \int V_{ext}^{(1)}(\mathbf{r})n^{(1)}(\mathbf{r})d^3r,$$
$$\langle\Psi^{(2)}|H^{(1)}|\Psi^{(2)}\rangle = \langle\Psi^{(2)}|T|\Psi^{(2)}\rangle + \langle\Psi^{(2)}|V_{ee}|\Psi^{(2)}\rangle + \int V_{ext}^{(1)}(\mathbf{r})n^{(2)}(\mathbf{r})d^3r. \quad (3.23)$$

Using eqn. 3.22 and eqn. 3.23, we have

$$\langle\Psi^{(1)}|T|\Psi^{(1)}\rangle + \langle\Psi^{(1)}|V_{ee}|\Psi^{(1)}\rangle < \langle\Psi^{(2)}|T|\Psi^{(2)}\rangle + \langle\Psi^{(2)}|V_{ee}|\Psi^{(2)}\rangle. \quad (3.24)$$

Similarly, the expectation value of $\Psi^{(2)}$ in Hamiltonian $H^{(2)}$ should be lower than that of $\Psi^{(1)}$:

$$E^{(2)} = \langle\Psi^{(2)}|H^{(2)}|\Psi^{(2)}\rangle < \langle\Psi^{(1)}|H^{(2)}|\Psi^{(1)}\rangle. \quad (3.25)$$

Then we get

$$\langle\Psi^{(2)}|T|\Psi^{(2)}\rangle + \langle\Psi^{(2)}|V_{ee}|\Psi^{(2)}\rangle < \langle\Psi^{(1)}|T|\Psi^{(1)}\rangle + \langle\Psi^{(1)}|V_{ee}|\Psi^{(1)}\rangle. \quad (3.26)$$

Eqn. 3.24 and eqn. 3.26 give an absurd result. This reveals that no two different potentials $V_{ext}^{(1)}$ and $V_{ext}^{(2)}$ differing to within a constant can have the same ground state electron density $n(\mathbf{r})$. A straightforward consequence of this first Hohenberg and Kohn theorem is that the ground state energy is also a functional of the ground state density, i.e, if the ground state density is known, in principle, the ground state energy is a function of the density.

$$E_0 = E[n(\mathbf{r})] \quad (3.27)$$

The second Hohenberg and Kohn theorem affirms that the energy functional $E[n(\mathbf{r})]$ has a variational property in the sense that its minimum gives the exact ground state energy, and the electron density $n(\mathbf{r})$ that minimizes this functional is the exact ground

state density $n_0(\mathbf{r})$. To show this, a system with an external potential $V_{ext}^{(1)}$ having a ground state density $n^{(1)}(\mathbf{r})$ and a different density $n^{(2)}(\mathbf{r})$ with wavefunctions $\Psi^{(1)}$ and $\Psi^{(2)}$ respectively, are considered.

$$E^{(2)} = E[n^{(2)}(\mathbf{r})] = \langle \Psi^{(2)} | H^{(1)} | \Psi^{(2)} \rangle > \langle \Psi^{(1)} | H^{(1)} | \Psi^{(1)} \rangle = E^{(1)} = E[n^{(1)}(\mathbf{r})] = E_0. \tag{3.28}$$

Therefore, the energy functional with the ground state density $n^{(1)}(\mathbf{r})$ is the ground state energy for the Hamiltonian with the external potential determined by $n^{(1)}(\mathbf{r})$.

The energy that is a functional of the electron density $n(\mathbf{r})$, can be divided into two part such as

$$E[n(\mathbf{r})] = F[n(\mathbf{r})] + \int d^3r V_{ext}(\mathbf{r}) n(\mathbf{r}), \tag{3.29}$$

where $F[n(\mathbf{r})] = \langle \Psi | T + V_{ee} | \Psi \rangle$ is an universal functional, i.e. it is independent of $V_{ext}(\mathbf{r})$. The minimum of this functional is obtained when the input density is equal to the exact ground state density. In principle, by minimizing $E[n(\mathbf{r})]$ with respect to the electron density $n(\mathbf{r})$, the exact ground state density and energy can be obtained. However, the functional $F[n(\mathbf{r})]$ is not known explicitly and approximation is needed.

3.4 Kohn-Sham equations

In the previous section, it is clearly shown that the ground state energy is a functional of the electron density but we do not know what exactly this functional is. This was a huge challenge for DFT to be an accessible method. In 1965, DFT was made in practice due the KS theory [13]. The main idea of this theory is to replace the fully interacting many-body system with an auxiliary system that can be solved more easily. The KS ansatz assumes that the ground state density of the difficult interacting system is the

same as a system of non-interacting electrons moving in a mean field way [10].

The kinetic energy of the non-interacting electrons denoted by T_s with a density of $n(\mathbf{r})$ is given by

$$T_s[n(\mathbf{r})] = -\frac{1}{2}\sum_i \int \psi_i^*(\mathbf{r})\nabla^2\psi_i(\mathbf{r})d^3r, \tag{3.30}$$

where $\psi_i(\mathbf{r})$ is a single electron wavefunction. In the real system, the correlation will change the kinetic energy and the additional term is denoted by $T_c[n(\mathbf{r})]$. So

$$T[n(\mathbf{r})] = T_s[n(\mathbf{r})] + T_c[n(\mathbf{r})] \tag{3.31}$$

$T_c[n(\mathbf{r})]$ is generally unknown.

For the electron-electron interaction, similar to that of the kinetic energy $T[n(\mathbf{r})]$, KS represented it as a sum of the classical Coulomb electron repulsion and a correction term that is unknown:

$$\begin{aligned} E_{ee}[n(\mathbf{r})] = \frac{1}{2}\int\int \frac{n(\mathbf{r}_1)n(\mathbf{r}_2)}{|\mathbf{r}_1-\mathbf{r}_2|}d^3r_1d^3r_2 + U_{xc}[n(\mathbf{r})], \\ E_{ee}[n(\mathbf{r})] = E_{Hartree}[n(\mathbf{r})] + U_{xc}[n(\mathbf{r})]. \end{aligned} \tag{3.32}$$

The functional $F[n(\mathbf{r})]$ in eqn. 3.29 can then be written as

$$\begin{aligned} F[n(\mathbf{r})] = T_s[n(\mathbf{r})] + E_{Hartree}[n(\mathbf{r})] + \underbrace{T_c[n(\mathbf{r})] + U_{xc}[n(\mathbf{r})]}_{E_{xc}[n(\mathbf{r})]}, \\ F[n(\mathbf{r})] = T_s[n(\mathbf{r})] + E_{Hartree}[n(\mathbf{r})] + E_{xc}[n(\mathbf{r})]. \end{aligned} \tag{3.33}$$

Therefore, the total energy in eqn. 3.29 of the real (interacting) system is written as :

$$E[n(\mathbf{r})] = T_s[n(\mathbf{r})] + E_{Hartree}[n(\mathbf{r})] + E_{xc}[n(\mathbf{r})] + \int V_{ext}n(\mathbf{r})d^3r. \tag{3.34}$$

The application of the variational principle subject to the orthogonality constraint $\int \psi_i^*(\mathbf{r})\psi_j(\mathbf{r})d\mathbf{r} = \delta_{ij}$,

$$\frac{\delta\, E[n(\mathbf{r})]}{\delta\psi_i^*(\mathbf{r})} = \frac{\delta\, T_s[n(\mathbf{r})]}{\delta\psi_i^*(\mathbf{r})} + \left[\frac{\delta \int V_{ext}(\mathbf{r})n(\mathbf{r})d^3r}{\delta\, n(\mathbf{r})} + \frac{\delta\, E_{Hartree}[n(\mathbf{r})]}{\delta\, n(\mathbf{r})} + \frac{\delta E_{xc}[n(\mathbf{r})]}{\delta n(\mathbf{r})}\right] \frac{\delta n(\mathbf{r})}{\delta\psi_i^*(\mathbf{r})} = 0, \tag{3.35}$$

leads to the set of KS equations for electrons moving in an effective potential:

$$\left[[-\frac{1}{2}\nabla^2 + V_{eff}(\mathbf{r})\right] \psi_i(\mathbf{r}) = \epsilon_i\psi_i(\mathbf{r}), \tag{3.36}$$

where ϵ_i is the one electron KS energy and $V_{eff}(\mathbf{r})$ is the effective potential given by

$$V_{eff}(\mathbf{r}) = V_{ext}(\mathbf{r}) + V_{Hartree}(\mathbf{r}) + V_{xc}(\mathbf{r}). \tag{3.37}$$

obtained by considering each term in eqn. 3.35.

$$\begin{aligned} V_{ext}(\mathbf{r}) &= \frac{\delta \int V_{ext}(\mathbf{r})n(\mathbf{r})d^3r}{\delta\, n(\mathbf{r})}, \\ V_{Hartree}(\mathbf{r}) &= \frac{\delta\, E_{Hartree}[n(\mathbf{r})]}{\delta\, n(\mathbf{r})}, \\ V_{xc}(\mathbf{r}) &= \frac{\delta E_{xc}[n(\mathbf{r})]}{\delta n(\mathbf{r})}. \end{aligned} \tag{3.38}$$

3.5 Exchange-correlation energy functional

As seen earlier, the KS ansatz consists of solving the many-body problem by mapping the original interacting many-body system onto a set of independent single particle equations (see eqn. 3.36). However, the KS equations remain unsolvable unless the exchange-correlation energy functional $E_{xc}[n(\mathbf{r})]$ in eqn. 3.34 is exactly defined. In practice, the exact expression of this energy functional is not known explicitly and

approximations are adopted. To give a perspective on these approximations, it is necessary to describe the analytical features of the exchange-correlation energy.

The many-body Hamiltonian can be written in such a way that the fictitious non-interacting system and the fully interacting system are connected using a coupling constant λ [1, 12]

$$H_\lambda = T + \lambda V_{ee} + \lambda V_{ext}^\lambda, \tag{3.39}$$

where $\lambda = 0$ corresponds to the case of noninteracting system and $\lambda = 1$ to the original interacting one. This allows the exchange-correlation energy to have the form of [1, 12]

$$E_{xc}[n] = \left\langle \Psi^\lambda[n]|T + \lambda V_{ee}|\Psi^\lambda[n]\right\rangle\Big|_{\lambda=1} - \left\langle \Psi^\lambda[n]|T + \lambda V_{ee}|\Psi^\lambda[n]\right\rangle\Big|_{\lambda=0} - E_{Hartree}. \tag{3.40}$$

$\Psi^\lambda[n]$ is the minimizing wavefunction for each λ.

Eqn 3.40 can be expressed into an integral over the parameter λ

$$\begin{aligned} E_{xc}[n] &= \int_0^1 d\lambda \frac{d}{d\lambda}\left\langle \Psi^\lambda[n]|T + \lambda V_{ee}|\Psi^\lambda[n]\right\rangle - E_{Hartree} \\ &= \int_0^1 d\lambda \left\langle \Psi^\lambda[n]|\frac{dV_{ee}}{d\lambda}|\Psi^\lambda[n]\right\rangle - E_{Hartree}. \end{aligned} \tag{3.41}$$

Finally, eqn. 3.41 can be rewritten as a Coulomb type integral [5, 12] and the exact form of the exchange-correlation energy is obtained

$$E_{xc}[n] = \frac{1}{2}\int\int \frac{n(\mathbf{r})n_{xc}(\mathbf{r},\mathbf{r}')}{|\mathbf{r}-\mathbf{r}'|}d\mathbf{r}d\mathbf{r}', \tag{3.42}$$

where $n_{xc}(\mathbf{r},\mathbf{r}')$ is called exchange-correlation hole. Its physical meaning is that the presence of an electron at point $\mathbf{r}$ decreases the probability of having another electron

at a position $\mathbf{r}'$ due to the Pauli antisymmetry and to the Coulomb repulsion. From eqn. 3.42, the exact exchange-correlation energy can be interpreted as the interaction between the electron density $n(\mathbf{r})$ and the density $n_{xc}(\mathbf{r}, \mathbf{r}')$ of the hole. An important nature of the exchange-correlation hole is that it obeys a sum rule

$$\int d\mathbf{r}' n_{xc}(\mathbf{r}, \mathbf{r}') = -1. \tag{3.43}$$

Furthermore, the exchange-correlation hole can be decomposed as a sum of the separate exchange and correlation hole $n_{xc}(\mathbf{r}, \mathbf{r}') = n_x(\mathbf{r}, \mathbf{r}') + n_c(\mathbf{r}, \mathbf{r}')$. They also respect the sum rules

$$\int d\mathbf{r}' n_x(\mathbf{r}, \mathbf{r}') = -1, \qquad \int d\mathbf{r}' n_c(\mathbf{r}, \mathbf{r}') = 0. \tag{3.44}$$

These sum rules are among the primary requirement for developing approximation to the $E_{xc}[n]$ functional. Various approximations have already been developed to define the exchange-correlation energy. The standard DFT functional including the flavor of the LDA and the GGA are the most popular one. Since these types of functional are known to underestimate the band gap of the system, the idea of the hybrid functional is introduced to improve their accuracy.

3.5.1 Local density approximation

The LDA approximation [13] is the most popular exchange-correlation energy in DFT calculations for a long time. The main idea of this approximation is to assume the exchange-correlation energy per electron at each point $\mathbf{r}$ ($\varepsilon_{xc}(\mathbf{r})$) to be similar to that of homogeneous electron gas ($\varepsilon_{xc}^{\mathrm{HEG}}(\mathbf{r})$). Noting that the exchange-correlation energy for a homogeneous electron gas has good and exact numerical approximations such as in quantum Monte Carlo (QMC). Within this approximation, the exchange-correlation energy density of the inhomogeneous electronic systems [5, 9, 13] is written as

$$E_{xc}^{\mathrm{LDA}}[n(\mathbf{r})] = \int \varepsilon_{xc}[n(\mathbf{r})]\; d^3r, \tag{3.45}$$

with

$$\varepsilon_{xc}[n(\mathbf{r})] = \varepsilon_{xc}^{\mathrm{HEG}}[n(\mathbf{r})]. \tag{3.46}$$

Eqn. 3.45 is applicable for non magnetic cases. In magnetic systems, the introduction of the two spin densities $(n^{\uparrow}(\mathbf{r}), n^{\downarrow}(\mathbf{r}))$ is crucial in order to obtain better approximation. In this case, the exchange-correlation functional system is given by

$$E_{xc}^{\mathrm{LSDA}}[n^{\uparrow}(\mathbf{r}), n^{\downarrow}(\mathbf{r})] = \int d^3r\, n(\mathbf{r})\, \varepsilon_{xc}^{\mathrm{HEG}}[n^{\uparrow}(\mathbf{r}), n^{\downarrow}(\mathbf{r})], \tag{3.47}$$

The energy per electron $\varepsilon_{xc}[n(\mathbf{r})]$ can be separated into exchange and correlation terms

$$\varepsilon_{xc}[n(\mathbf{r})] = \varepsilon_x[n(\mathbf{r})] + \varepsilon_c[n(\mathbf{r})]. \tag{3.48}$$

The exchange term $\varepsilon_x[n(\mathbf{r})]$ was derived by Bloch and Dirac in 1930 [14]. It is equivalent to the exchange used by Slater in the HF approximation [6]

$$\varepsilon_x[n(\mathbf{r})] = C_x n(\mathbf{r})^{\frac{1}{3}} \quad \text{with} \quad C_x = -\frac{3}{4}\left(\frac{3}{\pi}\right)^{\frac{1}{3}} \approx -0.738. \tag{3.49}$$

The spin polarized system is described in the local density approach with two parameters : the Wigner-Seitzs radius r_s which is defined as the radius of a sphere considered to have on average one electron, and a parameter ζ with the relation

$$n(\mathbf{r}) = n^{\uparrow}(\mathbf{r}) + n^{\downarrow}(\mathbf{r}), \quad \zeta = \frac{n^{\uparrow}(\mathbf{r}) - n^{\downarrow}(\mathbf{r})}{n(\mathbf{r})}, \quad r_s = \left(\frac{3}{4\pi n(\mathbf{r})}\right)^{\frac{1}{3}}. \tag{3.50}$$

By introducing these parameters into the eqn. 3.49, the exchange energy for an unpolarized ($\zeta = 0$) system is given by

$$\varepsilon_x[\zeta = 0, r_s] = \frac{3}{4\pi r_s}\left(\frac{9\pi}{4}\right)^{\frac{1}{3}}, \tag{3.51}$$

and that one of polarized ($\zeta = 1$) is given by

$$\varepsilon_x[\zeta = 1, r_s] = \frac{3}{4\pi r_s}\left(\frac{18\pi}{4}\right)^{\frac{1}{3}}. \tag{3.52}$$

The exchange term can be calculated exactly but for the correlation contribution, there is no explicit expression. The standard approximation is to use the QMC simulations of the homogeneous electron gas as Ceperley and Alder proposed in 1980 [15]. Based on their simulation results, analytical expressions of the correlation energy $\varepsilon_c[n(\mathbf{r})]$ have been deduced from interpolation. The most popular ones are those described by Vosko, Wilk and Nusair (VWN) in Ref. [16], Perdew and Wang (PW) in Ref. [17] and Perdew and Zunger (PZ) in Ref [18].

L(S)DA is by construction an exact approximation for a homogeneous electron system. It is a good approximation for the systems of slowly varying density. The advantage of this approximation is that the energy error occurred in the exchange terms cancel out with that one in the correlation terms. A comparison study between QMC and LDA calculations of bulk silicon shows that there are huge errors in the exchange and correlation energies of the LDA but they tend to cancel as the $\varepsilon_c[n(\mathbf{r})]$ value is underestimated while that one of $\varepsilon_x[n(\mathbf{r})]$ is overestimated [19]. Moreover, the LDA exchange-correlation hole obeys the sum rule described earlier. Although L(S)DA remains a popular approximation in solid state calculations, it presents several failures such as underestimation of the bond lengths due to the over binding the atoms, overestimation of the atomization energies, underestimation of the volume of a bulk material, underestimation of the band gap of a semiconductor material, etc. Therefore, improvement of the approximation is needed to increase the accuracy of the DFT method.

3.5.2 Generalized gradient approximation

In the LDA approximation, the exchange energy at one point depends only on the charge density at that point. To improve the LDA approximation, some additional non local information are added by incorporating the gradient of the electron density. This method is known as GGA approximation. Actually, the gradient-corrected functional is constructed in order to take into account the inhomogeneity of the true electron density and its expression is given by

$$E_{xc}^{\mathrm{GGA}}[n^{\uparrow}(\mathbf{r}), n^{\downarrow}(\mathbf{r})] = \int \varepsilon_{xc}[n(\mathbf{r})]n(\mathbf{r})g[n^{\uparrow}(\mathbf{r}), n^{\downarrow}(\mathbf{r}), \nabla n(\mathbf{r})^{\uparrow}, \nabla n(\mathbf{r})^{\downarrow}]d^3r, \tag{3.53}$$

where $\varepsilon_{xc}[n(\mathbf{r})]$ is the homogeneous electron gas energy density as described in the LDA.

There are different flavors of GGA functional depending on the parametrization of the function g and $\varepsilon_{xc}[n(\mathbf{r})]$. The GGA functional proposed by PBE is the popular one and is used in this thesis. Similar to the idea in the LDA approximation, it consists of separating the expression of the exchange-correlation energy functional into two parts. The first part is the exchange contribution given by

$$E_x^{\mathrm{GGA(PBE)}}[n(\mathbf{r})] = \int \varepsilon_x^{\mathrm{HEG}}[n(\mathbf{r})]\, F_x(\gamma)\, n(\mathbf{r})\, d^3r, \tag{3.54}$$

This expression means that the exchange energy per electron for a homogeneous gas is improved by multiplying a factor F_x that depends on the reduced dimensionless gradient of the density $\gamma = \frac{|\lambda_n|}{[2(3\pi^2)^{\frac{1}{3}} n^{\frac{4}{3}}]}$ [20]. The expression of the F_x is given by

$$F_x(s) = 1 + k - \frac{k}{1 + \frac{\beta(\pi\gamma)^2}{3k}}, \tag{3.55}$$

The parameter k value is equal to 0.804 in the GGA functional proposed by Perdew, Burke, Ernzerhof (PBE) and is chosen in such a way that the Lieb-Oxford bound written

as [21]

$$E_x^{\mathrm{GGA}}[n^{\uparrow}(\mathbf{r}), n^{\downarrow}(\mathbf{r})] \geq E_{xc}^{\mathrm{GGA}}[n^{\uparrow}(\mathbf{r}), n^{\downarrow}(\mathbf{r})] \geq 2.273 E_x^{\mathrm{LDA}}[n], \tag{3.56}$$

is satisfied. $\frac{\beta(\pi\gamma)^2}{3k}$ term in eqn. 3.55 is set to 0.219 in PBE to ensure that the second-order exchange term cancels with the second-order of the correlation contribution [20, 22].

The second part is the correlation contribution. For the PBE parameterization, it is defined as:

$$E_c^{\mathrm{GGA(PBE)}}[n^{\uparrow}, n^{\downarrow}] = \int d^3r\, n(\mathbf{r})\, \left[\varepsilon_c^{\mathrm{HEG}}(r_s, \zeta) + H_{\mathrm{PBE}}(r_s, \zeta, t)\right]. \tag{3.57}$$

The term $H_{\mathrm{PBE}}(r_s, \zeta, t)$ is a gradient contribution added to the homogeneous gas feature and the parameter t is a dimensionless quantity given by the gradient of the density.

The GGA-PBE exchange-correlation at the same time presents success and failures. It is known to accurately predict the energy and geometry of some atoms, molecules, and solids. It improves the binding energies, the atomization energies and geometries of those systems for large varying density $n(\mathbf{r})$ up to certain limit [9]. However, the Hartree self-interaction and the lack of integer discontinuity in the exchange and correlation energy have been the important issues in the standard DFT method which extremely need further improvement.

3.5.3 Hybrid functionals

The hybrid functionals are the promising approximations in describing the exchange and correlation energy of the many-body system. They enhance the accuracy of the many-body properties obtained with the semilocal functionals, although their application in a solid is still problematic. The idea for constructing the hybrid functionals is to combine

some part of the exact exchange in the HF method with the semilocal exchange in the DFT method in order to complement their failures [23]. Various hybrid exchange-correlation functionals have been developed.

Becke [24] proposed a combination of the local exchange-correlation functionals (LDA) with the HF exchange. This mixture gives accurate result since the HF method is exact for a noninteracting system and the local exchange-correlation functionals provide a good description of the interacting system. An adiabatic connection between the noninteracting and fully interacting systems at a constant density was proposed in this method and is given by

$$E_{xc}[n] = \int_0^1 d\lambda E_{xc,\lambda}[n]. \tag{3.58}$$

$E_{xc}[n]$ is the exchange-correlation energy and λ represents the strength of the electron-electron interaction. The term $E_{xc,\lambda}[n]$ involves all exchange and correlation effects for a specific value of λ and it is written as

$$E_{xc,\lambda}[n] = (1-\lambda)E_x^{\mathrm{HF}}[n] + \lambda E_{xc}^{\mathrm{LDA}}[n], \tag{3.59}$$

where $E_x^{\mathrm{HF}}[n]$ is the exchange energy of the HF method and $E_x^{\mathrm{LDA}}[n]$ is the exchange-correlation energy of the LDA functional. Incorporating eqn. 3.59 into eqn. 3.58, and evaluating the integral, we have

$$E_{xc}[n] = \frac{1}{2}E_x^{\mathrm{HF}}[n] + \frac{1}{2}E_{xc}^{\mathrm{LDA}}[n]. \tag{3.60}$$

This means that 50% of the HF exchange and 50% of the LDA exchange-correlation are combined. Thereafter, Becke improved this first hybrid functional approach by considering a semi-empirical approach and by adding non local functional. These functionals are known as Becke's three parameter hybrid functional denoted by B3X [25, 26]

$$E_{\mathrm{xc}}^{\mathrm{B3X}} = E_{\mathrm{xc}}^{\mathrm{LDA}} + \alpha_0(E_{\mathrm{x}}^{\mathrm{HF}} - E_{\mathrm{x}}^{\mathrm{LDA}}) + \alpha_{\mathrm{x}}(E_{\mathrm{x}}^{\mathrm{X}} - E_{\mathrm{x}}^{\mathrm{LDA}}) + \alpha_{\mathrm{c}}(E_{\mathrm{c}}^{\mathrm{X}} - E_{\mathrm{c}}^{\mathrm{LDA}}), \qquad (3.61)$$

and B1X, a one parameter hybrid functional

$$E_{\mathrm{xc}}^{\mathrm{B1X}} = \alpha E_{\mathrm{xc}}^{\mathrm{X}} + \alpha(E_{\mathrm{x}}^{\mathrm{HF}} - E_{\mathrm{x}}^{\mathrm{X}}), \qquad (3.62)$$

where X in eqn. 3.61 and eqn. 3.62 corresponds to a flavor of GGA functional.

Perdew et al. [27, 28] proposed the mixture of the popular PBE and HF exchange in the B1X functional. This hybrid functional is known as PBE0 hybrid functional and the exchange-correlation energy is written as

$$E_{\mathrm{xc}}^{\mathrm{PBE0}} = \alpha E_{\mathrm{xc}}^{\mathrm{PBE}} + \alpha(E_{\mathrm{x}}^{\mathrm{HF}} - E_{\mathrm{x}}^{\mathrm{PBE}}), \qquad (3.63)$$

In this approximation, the value of α was chosen to be equal to $\frac{1}{4}$. By separating the exchange and correlation of the PBE part and replacing α with its value, the PBE0 exchange-correlation energy becomes

$$\begin{aligned} E_{\mathrm{xc}}^{\mathrm{PBE0}} &= \alpha E_{\mathrm{x}}^{\mathrm{HF}} + (1-\alpha)E_{\mathrm{x}}^{\mathrm{PBE}} + E_{\mathrm{c}}^{\mathrm{PBE}} \\ &= \frac{1}{4}E_{\mathrm{x}}^{\mathrm{HF}} + \frac{3}{4}E_{\mathrm{x}}^{\mathrm{PBE}} + E_{\mathrm{c}}^{\mathrm{PBE}} \end{aligned} \qquad (3.64)$$

where $E_{\mathrm{x}}^{\mathrm{HF}}$, $E_{\mathrm{x}}^{\mathrm{PBE}}$ and $E_{\mathrm{c}}^{\mathrm{PBE}}$ are the HF exact exchange functional, the PBE exchange functional and correlation functional respectively. From eqn. 3.64, it is clearly seen that in a PBE0 hybrid functional, the PBE and HF exchange is mixed with a percentage of 75% and 25% respectively .

Although the methods proposed by Becke [24] and Perdew [27] give accurate results, they are computationally very expensive compared to the standard DFT, especially

for a large system due to the long-range (LR) feature of the Coulomb potential in the HF exchange [23]. To address this issue, Heyd *et al.* [23] introduced the new flavor of hybrid exchange-correlation functional known as the Heyd, Scuseria, Ernzerhof (HSE) functional. Heyd *et al.* [23] decided to divide the Coulomb operator into two ranges using the error function $erf(y)$ and the complementary error function $erfc(y) = 1 - erf(y)$

$$\frac{1}{r_{12}} = \underbrace{\frac{erfc(\eta r_{12})}{r_{12}}}_{Short\ Range\ (\mathrm{SR})} + \underbrace{\frac{erf(\eta r_{12})}{r_{12}}}_{Long\ Range(\mathrm{LR})} . \tag{3.65}$$

The parameter η is called screening parameter. It is an adjustable parameter which controls the definition of the two ranges (SR and LR). If η is equal to zero, the SR term correspond to the full Coulomb operator and the LR term is equal to zero.

By splitting all exchange terms in eqn. 3.64 into their short and long range parts, we have

$$E_{\mathrm{xc}}^{\mathrm{PBE0}} = \alpha E_{\mathrm{x}}^{\mathrm{HF,SR}}(\eta) + \alpha E_{\mathrm{x}}^{\mathrm{HF,LR}}(\eta) + (1-\alpha) E_{\mathrm{x}}^{\mathrm{PBE,SR}}(\eta) + E_{\mathrm{x}}^{\mathrm{PBE,LR}}(\eta) - \alpha E_{\mathrm{x}}^{\mathrm{PBE,LR}}(\eta) + E_{\mathrm{c}}^{\mathrm{PBE}}, \tag{3.66}$$

It was reported that $E_{\mathrm{x}}^{\mathrm{HF,LR}}$ and $E_{\mathrm{x}}^{\mathrm{PBE,LR}}$ are very small and negligible [29]. Therefore, the exchange-correlation energy of the HSE functional is obtained and written as

$$E_{\mathrm{xc}}^{\mathrm{HSE}} = \alpha E_{\mathrm{x}}^{\mathrm{HF,SR}}(\eta) + (1-\alpha) E_{\mathrm{x}}^{\mathrm{PBE,SR}}(\eta) + E_{\mathrm{x}}^{\mathrm{PBE,LR}}(\eta) + E_{\mathrm{c}}^{\mathrm{PBE}}, \tag{3.67}$$

The mixing parameter α is equal to $\frac{1}{4}$. $E_{\mathrm{x}}^{\mathrm{HF,SR}}(\eta)$ and $E_{\mathrm{x}}^{\mathrm{PBE,SR}}(\eta)$ are the short range of HF and PBE exchange functionals respectively. $E_{\mathrm{x}}^{\mathrm{PBE,LR}}(\eta)$ and $E_{\mathrm{c}}^{\mathrm{PBE}}(\eta)$ are

the long range and the correlation part of the PBE exchange functional. The HSE flavors are named depending on the screening parameters η, HSE03 for $\eta = 0.15$ and HSE06 for $\eta = 0.11$. In this study, we use the HSE06 screened hybrid functionals since it has been reported to predict the band gap of materials close to the experiment values [30].

3.6 Solution to Khon-Sham equations

Various methods can be used to solve the one particle KS equations. The most popular ones are: (i) firstly, the use of atomic basis sets also called localized basis sets in quantum chemistry. This method uses the Gaussian basis sets to expand all wavefunctions. (ii) Secondly, the Green's function method invented by Korringa, Kohn and Rostoker called also KKR method. This method transforms the Schrödinger equation into an equivalent integral equation based on the Green's theorem. (iii) Next, the linear method known as the augmented plane wave (APW) method. This method considers the full wavefunctions and treats all elements of the periodic table on the same level. (iv) In a solid, the pseudopotential methods successfully represent the real wavefunctions and successfully describe the electronic and structural properties of a material. For a long time, the norm conserving *ab initio* pseudopotentials proposed by Hamann, Schlüter and Chiang was widely used. To date, the pseudopotential method using the plane wave basis set has become popular due to its efficiency and its formal simplicity. The latter method as implemented in the Vienna *ab initio* simulation packages (VASP) is detailed in this chapter.

3.7 Periodic boundary conditions

The infinite number of electrons in a real system is a huge challenge in the implementation of the KS equation. To address this issue, the periodic boundary conditions

(PBC) [31, 32] are the most common method used. These conditions reveal that the crystal structure of a solid is a repetition of a box called unit cell. The idea is that, if one particle leaves one box its image penetrates into the present box from the opposite side (see Fig. 3.1). These conditions are applicable to all arrangement of unit cell systems such as 1D, 2D and 3D systems.

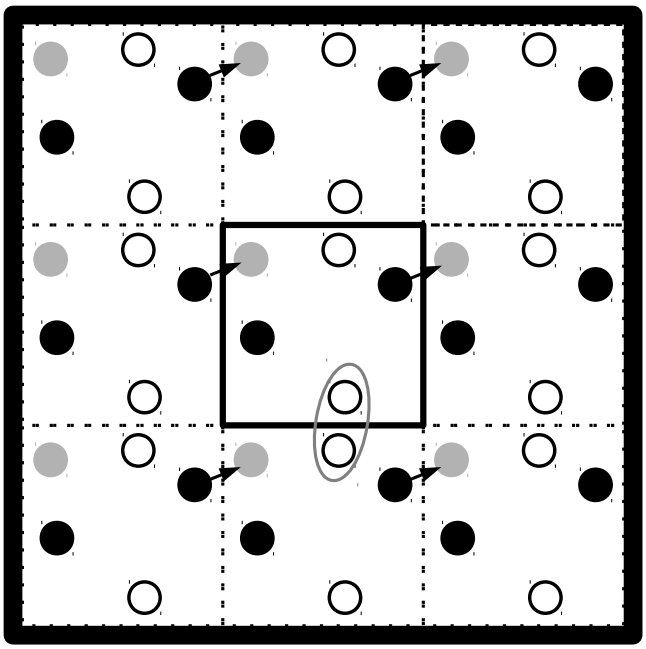

Figure 3.1: Schematic representation of the periodic boundary conditions of a 2D system. The black particle leaves the central box by the right-hand side and consequently re-enters through the left-hand side. The two white particles interact through the boundary.

3.8 Reciprocal lattice and Brillouin zone

Besides the direct lattice, the reciprocal lattice also plays an important role for the study of crystals. The reciprocal lattice in **k**-space is described as the set of all points (Fourier transform) for which the **k**-vector obeys $e^{i\mathbf{k}.\mathbf{R_n}} = 1$, for all position vector $\mathbf{R_n}$ of the direct lattice. If the lattice parameters of the system is denoted by $a,\ b,\ c$, the lattice vectors in the reciprocal space are given by $b_1 = \frac{2\pi}{a}\ \hat{x},\ b_2 = \frac{2\pi}{b}\ \hat{y}$ and $b_3 = \frac{2\pi}{c}\ \hat{z}$.

The equivalent of the Wigner-Seitz primitive cell in real space is called first Brillouin zone (FBZ) in reciprocal space with a volume of $\Omega_{BZ} = b_1.(b_2 \times b_3)$. The concept of FBZ is very useful for the evaluation of some properties of materials using DFT method.

3.9 Bloch's theorem and plane wave basis sets

The problem in solving the KS equations is the presence of the infinite number of moving non-interacting electrons that interact with an infinite static nuclei. For the representation of each existing electron, the wavefunction has to be calculated and an infinite basis set is required. The most common idea to overcome this problem is by employing the the Bloch's theorem. It relates the properties of the electrons in the entire system (infinite) with those of the electrons within a unit cell. Bloch's theorem states that the wavefunction of an electron in a periodic potential can have the form of a wave-like function $e^{i\mathbf{k}\cdot\mathbf{r}}$ multiply by a term that has the lattice periodicity [8, 31].

$$\Psi_j(\mathbf{r}) = e^{i\mathbf{k}\cdot\mathbf{r}} f_j(\mathbf{r}). \tag{3.68}$$

where $\mathbf{k}$ denotes the wave vector along the FBZ.

The periodic term $f_j(\mathbf{r})$ can be expanded in the form of discrete plane wave basis sets having the reciprocal lattice vectors $\mathbf{G}$ as wave vectors. Different basis sets can be used to represent the wavefunction, for instance, one can represent the atomic wavefunctions as a basis set. The choice of plane waves has various advantages, it is mathematically simple, complete and can cover all space equally.

$$f_j(\mathbf{r}) = \sum_{\mathbf{G}} c_{j,\mathbf{G}}\ e^{i\mathbf{G}\cdot\mathbf{r}}. \tag{3.69}$$

The set of vectors $\mathbf{G}$ are the wave vectors in the reciprocal space defined by $\mathbf{G}.\mathbf{R} =$

$2\pi n$, where $\mathbf{R}$ is the bravais lattice vector and n is an integer. The wavefunction is then written as [31]

$$\Psi_j(\mathbf{r}) = \sum_{\mathbf{G}} c_{j,\mathbf{k}+\mathbf{G}}\ e^{i(\mathbf{k}+\mathbf{G})\cdot\mathbf{r}}. \tag{3.70}$$

Eqn 3.70 shows that the KS equation can be solved by finding a finite number of electronic wavefunctions in a unit cell. The calculation of the plane wave coefficient $c_{j,\mathbf{k}+\mathbf{G}}$ can be done self-consistently. In principle, there are an infinite number of allowed $\mathbf{G}$ vectors, therefore, a further truncation of the plane wave expansion is needed so that it can be handled computationally.

3.9.1 Kinetic energy cut-off

The use of plane wave basis set leads to a very simple form of the KS equation in eqn. 3.36. By substituting eqn. 3.70 and integrating over $\mathbf{r}$ region, eqn. 3.36 becomes [10]:

$$\sum_{\mathbf{G}'} \left[\frac{1}{2}|\mathbf{k}+\mathbf{G}|^2\delta_{\mathbf{G}\mathbf{G}'} + V_{II}(\mathbf{G}-\mathbf{G}') + V_{Hartree}(\mathbf{G}-\mathbf{G}') + V_{xc}(\mathbf{G}-\mathbf{G}')\right] c_{j,\mathbf{k}+\mathbf{G}'}$$

$$= \varepsilon_j c_{j,\mathbf{k}+\mathbf{G}}. \tag{3.71}$$

The term in between brackets represent the Hamiltonian matrix and its diagonalisation leads to the solution of eqn. 3.71. The first term $\frac{1}{2}|\mathbf{k}+\mathbf{G}|^2$ describes the kinetic energy of a particular plane wave in the reciprocal space. Each coefficient $c_{j,\mathbf{k}+\mathbf{G}'}$ is associated with a kinetic energy that constitutes the diagonal element of the Hamiltonian matrix. Therefore, the size of the Hamiltonian matrix is related to the kinetic energy term. However, the coefficients correspond to the high kinetic energies are typically more significant than the one with high kinetic energies [33]. In a DFT calculation, an essential parameter known as cut-off energy (E_{cutoff}) is defined to restrict the number of plane waves.

$$E_{cutoff} = \frac{1}{2}|\mathbf{k} + \mathbf{G}_{cut}|^2. \tag{3.72}$$

Thus, the energy lower than E_{cutoff} is kept in the expansion and the remaining coefficients are set to zero. The size of the matrix depends on the kinetic energy cut-off chosen. The use of kinetic energy cut-off concept definitely introduces an error in the total energy calculation but the error can be minimized by increasing the size of the basis set with the use of a large enough energy cut-off, obtained by performing a convergence test.

3.9.2 k-point grid sampling of the Brillouin zone

For a periodic system, the integral in real space over the system (infinite) can be expressed into an integral over the FBZ in reciprocal space (finite) due to Bloch's theorem. Many quantities such as charge density, matrix elements, DOS etc. require this concept for their evaluation. The integral over the FBZ is written as :

$$f(\mathbf{r}) = \frac{\Omega_R}{(2\pi)^3} \int_{BZ} F(\mathbf{k})\ d^3k, \tag{3.73}$$

where $F(\mathbf{k})$ is the Fourier transformation of the functions $f(\mathbf{r})$ and Ω_R is the volume of the unit cell. Unfortunately, there is an unlimited block vectors $\mathbf{k}$ that can be chosen in the FBZ. The evaluation of these integrals are done by considering the fact that the orbitals at the Bloch vectors $\mathbf{k}$ are similar. Because of this, it follows that the integrals over the FBZ can be approximated by a weighted sum over a discrete set of k-points. By introducing the theory of symmetrized plane-waves (SPW) [34]

$$A_m(\mathbf{k}) = \sum_R e^{i\mathbf{k}\cdot\mathbf{R}}, \tag{3.74}$$

the function $F(\mathbf{k})$ can be expressed in terms of Fourier-series :

$$F(\mathbf{k}) = F_o + \sum_{m=1} A_m(\mathbf{k}) \tag{3.75}$$

In practice, the calculations are carried out on a grid of points in the FBZ which are referred to **k**-points. Monkhorst and Pack [35] have developed a scheme generating the discrete **k**-points that delimit the FBZ. They suggest that the **k**-point grid can be obtained using the equation [5]

$$\mathbf{k}_{n_1,n_2,n_3} = \sum_{i=1}^{3} \frac{2n_i - N_i - 1}{2N_i}\mathbf{G}_i. \tag{3.76}$$

where $n_i = 1, \ldots, N_i$. N_i correspond to the number of **k**-points to be chosen in each direction and the vectors $\mathbf{G}_i$ are the primitive reciprocal lattice vectors.

In practice, the **k**-integration for an insulator does not cause problems since the Fermi level falls inside the gap and the density of states goes smoothly to zero before the gap. For a metal, the integration over the FBZ have the form :

$$I = \int_{BZ} F(\mathbf{k})[1 - \theta(E_k - E_F)]d^3\mathbf{k}. \tag{3.77}$$

This integration is challenging since the functions need to be multiplied by a sharp Fermi occupation before integrating. The smearing method proposed by Methfessel and Paxton [36] address this shortcoming. It consists on smoothen the sharp drop in electron occupation just below the Fermi level. They proposed an expansion in terms of Hermite functions which are simply Hermite polynomials multiplied by Gaussian. Thereafter, the partial occupancies around the Fermi level allow a faster convergence to be achieved with the use of small grid sizes.

3.10 Hellmann-Feynman theorem

The KS Hamiltonian is parameterized in ionic coordinates $\mathbf{R}_I$ by virtue of the BO approximation. During the atomic relaxations, one has to move the ion at different positions in order to find the equilibrium position. Using the forces acting on the ion to find the minimum is much more efficient than just looking at the value of the energy alone. Note that the minimum energy corresponds to zero force. For a given set of atomic positions, the ions will experience a force described by the Hellmann-Feynman theorem [37, 38]:

$$\mathbf{F}_I = -\frac{dE}{d\mathbf{R}_I} = -\frac{d}{d\mathbf{R}_I}\langle\Psi|H|\Psi\rangle = -\langle\Psi|\frac{dH}{d\mathbf{R}_I}|\Psi\rangle. \tag{3.78}$$

where E corresponds to the total energy of the system and $\mathbf{R}_I$ is the ionic position.

The atomic relaxation is based on the self-consistent of the total energy calculations. After moving the atom to a new position, the total energy for the new configuration is calculated followed by the the forces on each ion. Then, the ions is slightly moved depending on the calculated forces. The calculation goes back to step 2 until the ions reach their zero force equilibrium positions. In practice, a tolerance value of the force is always given.

3.11 Pseudopotentials

3.11.1 Background

As described earlier, plane wave basis set can be used to describe the wavefunctions of a periodic system. Unfortunately, for the study of electronic structure of a material, the presence of the core states around the nucleus hinders the use of plane wave since their wavefunction oscillates rapidly and requires a huge number of plane waves. However, most of the physical and chemical properties of a material depend mostly

on the valence electrons rather than the core electrons states. For the valence region (chemical bonding region), the wavefunction is smooth. This suggests that the motion of the core electron can be ignored in the electronic structure calculations. The main idea of the pseudopotential approximation is to freeze the core electrons, such that the valence electrons only experience an effective pseudo potential (electron-nuclear and core-valence interactions), which is much smoother than the nuclear Coulomb potential. The advantages of using a pseudopotential is to decrease the number of expansion coefficients used for the KS orbitals.

The idea of pseudopotential was first introduced by Fermi in 1934 followed by Hellmann in 1935 [39, 40] to study the energy level of alkali atoms. However, the accurate band structures using pseudopotential method was not achieved until the so called empirical pseudopotential method (EPM) [41, 42, 43] was developed. With this method, the energy levels of various semiconductor materials were used to obtain empirically the potentials needed to construct the atomic wavefunctions. The drawback of this method is that it depends heavily on the experimental results.

The more recent pseudopotential approximation is the *ab initio* pseudopotential method. There are various flavors of *ab initio* pseudopotential available including the norm-conserving, ultrasoft and projector augmented wave (PAW) pseudopotentials.

Norm-conserving pseudopotential was proposed by Hamann, Schlüter, and Chiang in 1979 [44]. It requires that (*i*) the energy of the all-electron (AE) and pseudo-wavefunctions must be identical and (*ii*) they must be the same outside the core radius denoted by $\mathbf{r_{cut}}$. (*iii*) The pseudo-charge and the true charge in the region inside $\mathbf{r_{cut}}$ must be equal. Norm-conserving pseudopotential is still considered as hard pseudopotential since it requires a huge number of Fourier components. Then, it was extended by Blöchl and Vanderbilt in 1990 and emerged the so called ultrasoft pseudopotential [45]. It ignores the constraint imposed by the norm-conserving and hence reduces the number of basis set as well as Fourier components used to describe valence electrons.

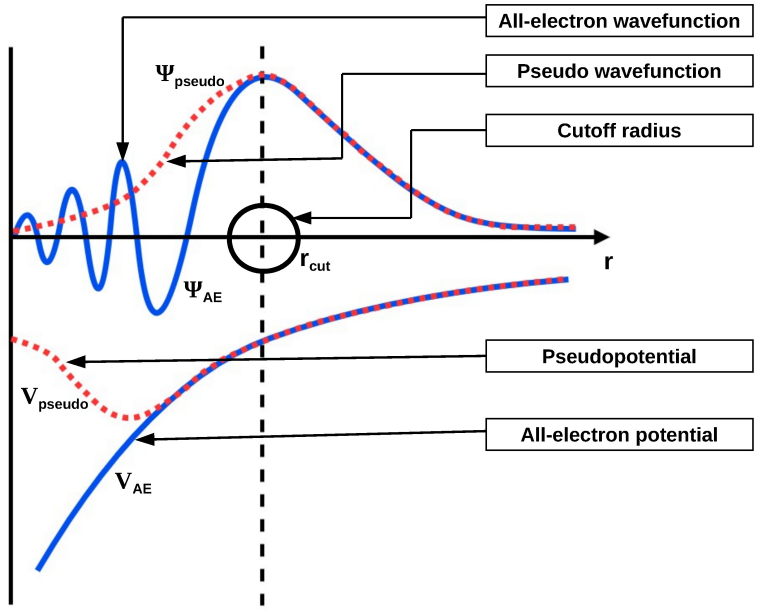

Figure 3.2: Blue solid lines: the all-electron potential and wavefunction for an atom; red dashed lines: the pseudo electron potential and wavefunction for an atom. $\mathbf{r_{cut}}$ indicates a cut-off radius outside of which the pseudo electron and the all-electron values match.

In this thesis, we consider the most recent formalism PAW pseudopotential to treat the core-valence interactions and a detail of its implementation is described in the next setion.

3.11.2 The projector augmented wave pseudopotential

The PAW pseudopotential was developed by Blöchl in 1994 [46]. In principle, it unifies the AE method with the traditional plane wave pseudopotential approach. To replace the rapidly oscillating wavefunctions near the nucleus with a smooth feature, Blöchl *et al.* [46] introduces a linear transformation operator denoted as $\mathcal{T}$ that transforms the pseudo wavefunctions $|\tilde{\Psi}\rangle$ to AE wavefunctions $|\Psi\rangle$:

$$|\Psi\rangle = \mathcal{T}|\tilde{\Psi}\rangle. \tag{3.79}$$

With PAW method, the space is divided into two regions: a non-overlapping atomic region, known as augmentation spheres, and an interstitial region defined by an uniform discretization such as a uniform grid or plane waves. The linear operator $\mathcal{T}$ can also be written in terms of a local atom-centred contribution $\mathcal{T}_R$ that is non-zero in the spherical augmentation region around atom R and is zero outside the sphere.

$$\mathcal{T} = 1 + \sum_R \mathcal{T}_R \tag{3.80}$$

Each atomic region has spherical augmentation functions called partial waves denoted by $|\tilde{\Phi}_i\rangle$. The pseudo wavefunctions $|\tilde{\Psi}\rangle$ can be expanded in terms of this pseudo partial waves in such a way that

$$|\tilde{\Psi}\rangle = \sum_i |\tilde{\Phi}_i\rangle c_i. \tag{3.81}$$

Since $\mathcal{T}$ is linear, the coefficient c_i can be obtained by applying an inner product between the pseudo-wavefunctions $|\tilde{\Psi}\rangle$ and a set of functions $|q_i\rangle$ called projector.

$$c_i = \langle q_i|\tilde{\Psi}\rangle \tag{3.82}$$

where

$$\begin{aligned} \langle q_i|\tilde{\Phi}_j\rangle &= \delta_{ij} \\ |\tilde{\Phi}_i\rangle\langle\tilde{q}_i| &= 1. \end{aligned} \tag{3.83}$$

Then eqn. 3.80 becomes:

$$\mathcal{T} = 1 + \sum_i \left(|\Phi_i\rangle - |\tilde{\Phi}_i\rangle\right) \langle\tilde{q}_i|, \tag{3.84}$$

Using this expression of the linear transformation, the AE wavefunction is given by

:

$$|\Psi\rangle = |\tilde{\Psi}\rangle + \sum_i (|\Phi_i\rangle - |\tilde{\Phi}_i\rangle)\langle\tilde{q}_i|\tilde{\Psi}\rangle. \tag{3.85}$$

The eqn. 3.85 allows any physical properties of a material to be calculated using PAW pseudopotential approach. For instance, the charge density can be expressed in terms of partial charge densities

$$n(\mathbf{r}) = \tilde{n}(\mathbf{r}) + n'(\mathbf{r}) - \tilde{n}'(\mathbf{r}), \tag{3.86}$$

The pseudo charge density $\tilde{n}(\mathbf{r})$ is obtained from the pseudo wavefunction $\tilde{\Psi}$ as

$$\tilde{n}(\mathbf{r}) = \sum_k f_k \langle\tilde{\Psi}_k|r\rangle\langle r|\tilde{\Psi}_k\rangle|, \tag{3.87}$$

k is the band index and f_k is the occupation of the state. The second and third part of the charge density in eqn. 3.86 are the AE density and pseudo density within spheres and given by :

$$n'(\mathbf{r}) = \sum_{k,(i,j)} f_k \langle\tilde{\Psi}_k|\tilde{q}_i\rangle\langle\Phi_i|\mathbf{r}\rangle\langle\mathbf{r}|\Phi_j\rangle\langle\tilde{q}_j|\tilde{\Psi}_k\rangle \tag{3.88}$$

and

$$\tilde{n}'(\mathbf{r}) = \sum_{k,(i,j)} f_k \langle\tilde{\Psi}_k|\tilde{q}_i\rangle\langle\tilde{\phi}_i|\mathbf{r}\rangle\langle\mathbf{r}|\tilde{\phi}_j\rangle\langle\tilde{q}_j|\tilde{\Psi}_k\rangle \tag{3.89}$$

respectively.

To have a better understanding, a pictorial representation of the calculated charge density using the PAW method is represented Fig. 3.3.

The same procedure as the charge density is applied to calculate the total energy E_{tot} of the system.

$$E_{tot} = \tilde{E} + E' - \tilde{E}', \tag{3.90}$$

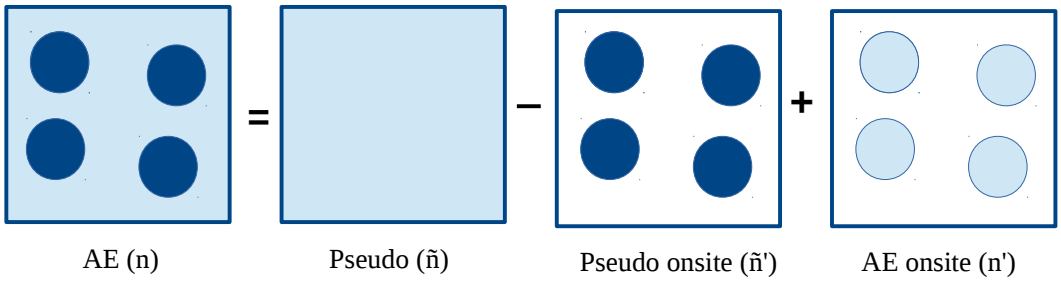

Figure 3.3: Representation of the calculation of the charge density using PAW pseudopotential.

$\tilde{E}$ is the pseudo energy given by:

$$\tilde{E} = \sum_n f_k \langle \tilde{\Psi}_k | -\frac{1}{2}\Delta | \tilde{\Psi}_k \rangle + E_{xc}[\tilde{n} + \hat{n} + \tilde{n_c}] + E_{Hartree}[\tilde{n} + \hat{n}] \\ + \int v_{Hartree}[\tilde{n}_{Zc}][\tilde{n}(\mathbf{r}) + \hat{n}(\mathbf{r})] d\mathbf{r} + U(\mathbf{R}, Z_{ion}). \tag{3.91}$$

The two energy terms E' and $\tilde{E}'$ can be expanded as:

$$E' = \sum_{ij} \rho_{ij} \langle \tilde{\phi}_i | -\frac{1}{2}\Delta | \tilde{\phi}_j \rangle + E_{xc}[n' + n_c] + E_{Hartree}[n'] \\ + \int_{\Omega_r} v_{Hartree}[n_{Zc}] n'(\mathbf{r})] d\mathbf{r}. \tag{3.92}$$

and

$$\tilde{E}' = \sum_{ij} \rho_{ij} \langle \tilde{\phi}_i | -\frac{1}{2}\Delta | \tilde{\phi}_j \rangle + E_{xc}[\tilde{n}' + \hat{n} + \tilde{n_c}] + E_{Hartree}[\tilde{n}' + \hat{n}] \\ + \int_{\Omega_r} v_{Hartree}[\tilde{n}_{Zc}][\tilde{n}'(\mathbf{r}) + \hat{n}(\mathbf{r})] d\mathbf{r} \tag{3.93}$$

An additional compensation charges $\hat{n}(\mathbf{r})$ is introduced to treat the long range electrostatic interactions between the PAW spheres. Eqn. 3.91 is evaluated on a regular grid whereas eqn. 3.92 and eqn. 3.93 are calculated on radial grids centered around each ion. These two terms are introduced to correct the shape difference between the AE and pseudo wavefunctions: the first one is the nodal features of the AE wavefunctions near the core, and the second is the orthogonality between core and valence states.

In this thesis, the PAW method was employed due to the tremendous advantages of its application. Generally, the PAW method is an AE and full-potential method. It does not deal with the tightly bonded core electrons resulting the reduction of the computational cost.

3.12 Tests of convergence

The accuracy of the DFT simulation depends on the various parameters used to compute the properties of the system. A test of convergence of the different parameters such as the plane wave kinetic energy cut-off and the number of k-points have been performed for this study.

Fig 3.4 shows the variation of the total energy of a MoS_2 monolayer with respect to the cut-off energy. It is clearly seen that the value of the total energy does not present a huge difference after 300 meV. Thus, It is not necessary to use an energy cut-off greater than 300 eV since the effects on the accuracy of the simulations will not change significantly. Therefore, all calculations in this thesis are carried out using an energy cut-off of 300 meV.

For the integration over the FBZ, the convergence of the k-points is also tested. Fig 3.5 presents the variation of the total energy with respect to the number of k-point chosen to sample the FBZ. It is noted that a choice of Monkhorst pack grid greater or equal to $2 \times 2 \times 1$ is preferable since the total energy value converges at this

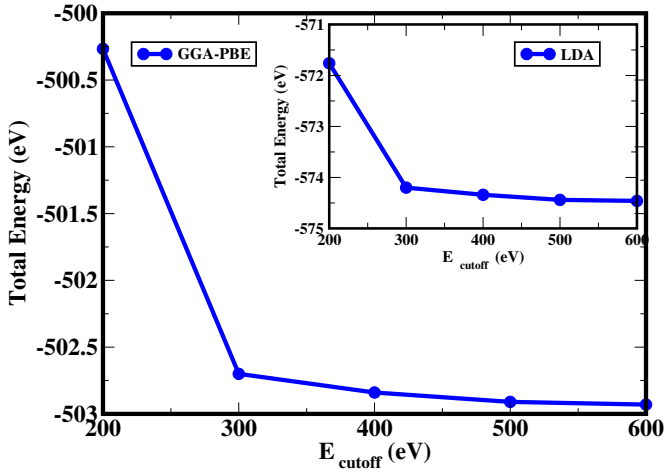

Figure 3.4: Plot of the total energy computed with GGA and LDA (inset plot) exchange-correlation functionals versus the cut-off energy as a test of convergence for a 5 × 5 × 1 supercell of a MoS_2 monolayer.

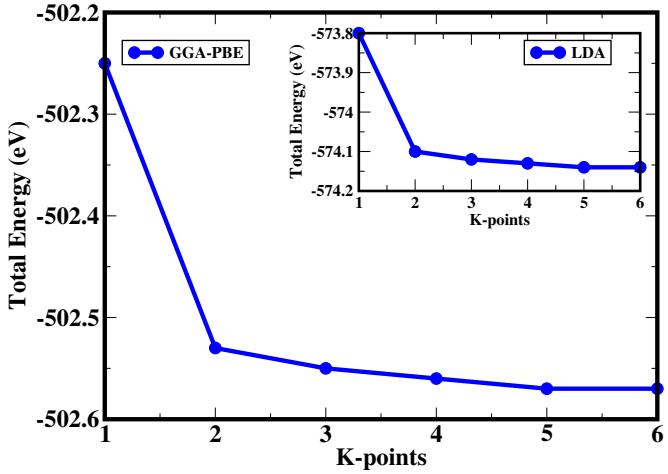

Figure 3.5: Plot of the total energy obtained from GGA and LDA (inset plot) exchange-correlation functionals with respect to a $n \times n \times 1$ k-point mesh as a test of convergence for a 5 × 5 × 1 supercell of a MoS_2 monolayer.

point. These convergences were also tested using different exchange-correlation for comparison, but no significant differences were observed on the plots as seen in fig. 3.4 and fig. 3.5.

The next chapter discusses the results for transition metal and chalcogen alloying in a MoS_2 monolayer obtained using DFT method as implemented in the VASP codes.

Bibliography

[1] D. Joubert, African School on Electronic Structure Methods: Density Functional Theory Basics, lecture notes, 3-45 (2008). [33, 34, 45]

[2] Paolo Giannozzi. Metodi Numerici in Struttura Elettronica. 2010. lecture notes. [33, 39]

[3] M. Born, R. Oppenheimer, Annalen der Physik 389 (20) (1927) 457-484. [34]

[4] D. R. Hartree, Mathematical Proceedings of the Cambridge Philosophical Society 24 (03) (1928) 426. [35]

[5] R. M. Martin, Electronic structure: basic theory and practical methods, Cambridge university press, 2004. [35, 37, 40, 45, 46, 59]

[6] V. Fock, Zeitschrift für Physik 61 (1-2) (1930) 126-148. [36, 47]

[7] J. C. Slater, Physical Review 35 (2) (1930) 210. [36]

[8] G. Grosso, G. Parravicini, Solid State Physics, Elsevier Science, 2000. [38, 56]

[9] J. Kohanoff, N. Gidopoulos, 2 (Part 5) (2003) 532-568. [39, 46, 50]

[10] M. C. Payne, M. P. Teter, D. C. Allan, T. A. Arias, J. D. Joannopoulos, Reviews of Modern Physics 64 (1992) 1045-1097. [39, 43, 57]

[11] P. Hohenberg, W. Kohn, Inhomogeneous electron gas, Physical review 136 (3B) (1964) B864. [40]

[12] D. Joubert (Ed.), Density Functionals: Theory and Applications, Springer Berlin Heidelberg, 1998. [45]

[13] W. Kohn, L. J. Sham, Physical review 140 (4A) (1965) A1133. [42, 46]

[14] P. A. Dirac, Vol. 26, Cambridge University Press, 1930, pp. 376-385. [47]

[15] D. M. Ceperley, B. Alder, Physical Review Letters 45 (7) (1980) 566. [48]

[16] S. Vosko, L. Wilk, and M. Nusair, Canadian Journal of Physics 58 (1980) 1200. [48]

[17] J. P. Perdew, Y. Wang, Physical Review B 45 (23) (1992) 13244. [48]

[18] J. P. Perdew, A. Zunger, Physical Review B 23 (10) (1981) 5048. [48]

[19] R. Q. Hood, M. Chou, A. Williamson, G. Rajagopal, R. Needs, W. Foulkes, Physical review letters 78 (17) (1997) 3350. [48]

[20] J. P. Perdew, K. Burke, M. Ernzerhof, Physical review letters 77 (18) (1996) 3865. [49, 50]

[21] E. H. Lieb, S. Oxford, International Journal of Quantum Chemistry 19 (3) (1981) 427-439. [50]

[22] P. Haas, F. Tran, P. Blaha, K. Schwarz, R. Laskowski, Physical Review B 80 (19) (2009) 195109. [50]

[23] J. Heyd, G. E. Scuseria, M. Ernzerhof, The Journal of chemical physics 118 (18) (2003) 8207-8215. [51, 53]

[24] A. D. Becke, Physical review A 38 (6) (1988) 3098. [51, 52]

[25] K. Kim, K. Jordan, The Journal of Physical Chemistry 98 (40) (1994) 10089-10094. [51]

[26] J. Piprek, no. vol. 1 in Series in Optics and Optoelectronics, CRC Press, 2017. [51]

[27] J. P. Perdew, M. Ernzerhof, K. Burke, The Journal of chemical physics 105 (22) (1996) 9982-9985. [52]

[28] C. Adamo, V. Barone, The Journal of chemical physics 110 (13) (1999) 6158-6170. [52]

[29] J. Heyd, Screened coulomb hybrid density functionals, Ph.D. thesis, Rice University (2004). [53]

[30] Y. Zhao, D. G. Truhlar, The Journal of Physical Chemistry A 110 (49) (2006) 1312613130. [54]

[31] N. Ashcroft, N. Mermin, Solid State Physics, HRW international editions, Holt, Rinehart and Winston, 1976. [55, 56, 57]

[32] M. P. Allen, D. J. Tildesley, Computer simulation of liquids, Oxford university press, 2017. [55]

[33] K. D. Brommer, B. Larson, M. Needels, J. Joannopoulos, Computers in Physics 7 (3) (1993) 350-362. [57]

[34] D. J. Chadi, M. L. Cohen, Physical Review B 8 (12) (1973) 5747. [58]

[35] H. J. Monkhorst, J. D. Pack, Physical review B 13 (12) (1976) 5188. [59]

[36] M. Methfessel and A. T. Paxton, Physical review B 40 (1989) 3616. [59]

[37] R. P. Feynman, Physical Review 56 (4) (1939) 340. [60]

[38] S. T. Epstein, A. C. Hurley, R. E. Wyatt, R. G. Parr, The Journal of Chemical Physics 47 (4) (1967) 1275-1286. [60]

[39] E. Fermi, Ricerca sci 7 (1936) 13-52. [61]

[40] H. Hellmann, W. Kassatotschkin, The Journal of Chemical Physics 4 (5) (1936) 324-325. [61]

[41] J. C. Phillips, Physical Review 112 (3) (1958) 685. [61]

[42] J. C. Phillips, Physical Review 116 (2) (1959) 287. [61]

[43] L. Kleinman, J. C. Phillips, Physical Review 118 (5) (1960) 1153. [61]

[44] D. R. Hamann, M. Schlüter, C. Chiang, Physical Review Letters 43 (1979) 1494-1497. [61]

[45] D. Vanderbilt, Physical Review B 41 (11) (1990) 7892. [61]

[46] P. E. Blöchl, Physical review B 50 (24) (1994) 17953. [62]

Chapter 4

Published paper: First-principles studies of chromium line-ordered in a MoS_2 monolayer

The results reported in this chapter has been published as N. F. Andriambelaza, R. E. Mapasha, N. Chetty, Journal of Physics: Condensed Matter 29 (32) (2017) 325504.

In this work, the influence of Cr atom concentration and configuration on the properties of a MoS_2 monolayer is reported. Firstly, detailed studies of a single and double Cr doping in a MoS_2 monolayer are considered. Secondly, the thermodynamic stability, structural and electronic properties of the hypothetical Cr line-ordered alloy are investigated. Various random alloy configurations are also considered in order to analyze the alloy shape effects on the properties of the MoS_2 monolayer. The complete results are found in the attached publication below. It contains the computational details used, the entire results and the conclusions of the study.

First-principles studies of chromium line-ordered alloys in a molybdenum disulfide monolayer

N.F. Andriambelaza[a,*], R.E. Mapasha[a], N. Chetty[a,b]

[a]*Department of Physics, University of Pretoria, Pretoria 0002, South Africa*
[b]*National Institute for Theoretical Physics, Johannesburg, 2000, South Africa*

Abstract

Density functional theory (DFT) calculations have been performed to study the thermodynamic stability, structural and electronic properties of various chromium (Cr) line-ordered alloy configurations in a molybdenum disulfide (MoS_2) hexagonal monolayer for band gap engineering. Only the molybdenum (Mo) sites were substituted at each concentration in this study. For comparison purpose, different Cr line-ordered alloy and random alloy configurations were studied and the most thermodynamically stable ones at each concentration were identified. The configurations formed by the nearest neighbor pair of Cr atoms are energetically most favorable. The line-ordered alloys are constantly lower in formation energy than the random alloys at each concentration. An increase in Cr concentration reduces the lattice constant of the MoS_2 system following the Vegard's law. From density of states (DOS) analysis, we found that the MoS_2 band gap is tunable by both the Cr line-ordered alloys and random alloys with the same magnitudes. The reduction of the band gap is mainly due to the hybridization of the Cr 3*d* and Mo 4*d* orbitals at the vicinity of the band edges. The band gap engineering and magnitudes (1.65 eV to 0.86 eV) suggest that the Cr alloys in a MoS_2 monolayer are good candidates for nanotechnology devices.

Keywords: Two dimensional material, Molybdenum disulfide, Density functional theory, Alloys.

1. Introduction

In the last few years, two dimensional (2D) layered materials have become an important area of research in material science. Due to their reduced dimensionality, they possess unique electronic and optical properties different from their bulk counterparts [1, 2, 3, 4]. These fascinating properties make 2D materials suitable candidates for various applications in nanoelectronic technologies [2, 5, 4]. The successful synthesis of graphene [6] was the starting point for the extensive exploration of different types of 2D materials. Graphene has extremely high charge carrier mobility and exceptional mechanical flexibility [1, 4]. However, it is a zero band gap material [1]. Consequently, this limits the direct application of graphene in the nanotechnological devices. Many experimental and theoretical efforts have been made to open a band gap in a graphene system [7, 8, 9, 10, 11]. A sizable band gap was achieved, but it was found to be either too small [7, 8, 9] or too large [10, 11]. This issue drove researchers to explore other 2D materials such as boronitrene (h-BN) [12] and transition metal dichalcogenides (TMD) [13]. Some of the TMD 2D systems are particularly interesting due to their tremendous properties such as high mechanical strength, direct band gap and optical transparency [14, 15, 16, 17]. Because of these exotic properties, TMD materials are suitable for applications in the nanoelectronic and optoelectronic devices [15, 18, 19].

TMD materials have the chemical formula MX_2, where M is a transition metal element and X stands for chalcogen from group VIB element. Depending on the type of the transition element and the chalcogen, TMD 2D systems can be an insu-

lator (e.g. Zirconium disulfide (ZrS_2)), metal (e.g. Niobium disulfide (NbS_2)), semimetal (e.g. Tungsten telluride (WTe_2)) and semiconductor (e.g. Chromium disulfide (CrS_2), Molybdenum disulfide (MoS_2) and Tungsten disulfide (WS_2)) [20]. Amongst the various TMD monolayers, MoS_2 monolayer is the most widely studied material owing to some of its special semiconducting properties similar to those of carbon-based graphene [21, 22]. As in other semiconductors, the electronic and optical properties of MoS_2 2D material are usually controllable by tuning the band gap. Thus, engineering the band gap of MoS_2 monolayer is important for designing nanoelectronic devices.

Historically, alloying has been used as an effective method to tune electronic structures of 3D semiconductor materials [23, 24, 25]. Recently, several experimental and theoretical studies have investigated the formation possibilities and electronic properties of alloys in the 2D TMD materials [26, 27, 28, 29]. For instance, Xu *et al*. [26] reported a chemical vapor deposition (CVD) strategy for the growth of $Mo_{1-x}W_xS_2$ and $MoS_{1-x}Se_x$ monolayers. It was found that W (Se) alloys increase (reduce) the band gap of pristine MoS_2 monolayer from 1.83 eV to 1.97 eV (1.55 eV). It was suggested that this band gap engineering is important to further optimize the performance of nanoscale photoelectronic devices. Tongay *et al*. [29] successfully synthesized $Mo_{1-x}W_xSe_2$ and reported that the band gap of a MoS_2 monolayer can be tuned by varying the W concentration. Using density functional theory (DFT) approach, Xi *et al*. [27] reported that the band gap of MoS_2 monolayer is tunable by W alloying and its enthalpy of formation is exothermic. Komsa *et al*. [28] investigated the thermodynamic stability and electronic properties of random $Mo_{1-x}W_xS_2$, $MoS_{1-x}Se_x$, $MoS_{1-x}Te_x$ and $MoSe_{1-x}Te_x$ alloys using DFT. They found that the formation energies for $MoS_{1-x}Te_x$ and $MoSe_{1-x}Te_x$ alloys are positive although very small and for $Mo_{1-x}W_xS_2$ and $MoS_{1-x}Se_x$ are negative. They also noted that the chalcogen alloys usually reduce the band gap of a MoS_2 monolayer, whereas W alloys raise it during the increase in concentration. In general, Se, Te and W alloys in a MoS_2 monolayer are exothermic and fine tune the band gap. This band gap engineering in a MoS_2 system is essential for the fabrication of nanoelectronic devices. Chromium (Cr) is in the same periodic table group with Mo and W, and thus deserve to be investigated as well. Ref. [30] reported that creating TMD alloys within the same transition metal group is usually feasible. This has been noted in the case of W replacing Mo or Se and Te replacing S in a MoS_2 monolayer. These type of systems have a very small lattice mismatch with the MoS_2 monolayer. To the best of our knowledge, there is no detailed publications on the study of $Mo_{1-x}Cr_xS_2$ and the transition from MoS_2 to CrS_2 monolayer through Cr alloying.

Studying all the possible configurations of alloys in a MoS_2 monolayer using a DFT method is not a tractable task. Alloys in a 2D materials can appear in different configurations such as clusters (many shapes : triangle-like, square, circular, etc), lines and can randomly scattered away from each other in different forms. The number of possible distinct configurations at any concentration with a number n of the Cr atoms is obtained by :

$$\frac{N!}{n!(N-n)!}\,, \tag{1}$$

where N is the total number of Mo sites in a monolayer. For instance, in the case of 20% concentration constituted by a total of 5 Cr atoms replacing the Mo atoms in a 5×5 supercell, there are 53130 possible configurations. Computing all of these possible configurations is practically impossible as this requires huge computational resources. To reduce this difficulty, adopting typical configurations is helpful. Experimentally, it was reported that the TMD alloys are usually synthesized in random phases at high temperatures [30]. However, DFT studies at 0 Kelvin have reported that ordered phases have a lower formation energy than random phases [30, 31, 32]. Most of the previous studies on TMD alloys considered various cluster configurations using a DFT approach [30, 31, 33]. A line alloy which is another form of ordered alloy can appear in different configurations in a MoS_2 monolayer, therefore worth to be studied and to know the most energetically favorable configuration. Komsa *et al*. [34] have studied line-ordered alloys of the

Se atoms substituting the S atoms in a MoS_2 monolayer. They stated that line-ordered alloy can be a way to alter the electronic properties of MoS_2 monolayer. The knowledge of the transition metal line-ordered alloys substituting the Mo sites is scarce.

In this paper, we present a comparative study of the physical properties of line-ordered alloys and random alloys of Cr atoms in a MoS_2 monolayer using a DFT approach. In a MoS_2 monolayer supercell, the possible line-ordered alloy configurations are few and can easily be identified at each Cr concentration. However, for the random alloys, a large number of different configurations are possible. Special quasi-random structure (SQS) method [35] is a tool that can mimic the possible random alloy configurations at each concentration. This method has been successfully applied to various alloys in a MoS_2 monolayer [33].

Based on the alloy formation energy analysis, we identify the lowest energy configurations for line-ordered alloys as well as random alloys at each concentration, when the Cr atoms substitute the Mo atoms. To have an insight to the electronic properties of the lowest energy configurations, the densities of states (DOS) were plotted. As opposed to W alloys, the band gap of $Mo_{1-x}Cr_xS_2$ decreases with the increase in Cr concentration. The band gap of MoS_2 monolayer is finite but tunable, making it a good candidate in nanoelectronic devices.

2. Methodology

We have systematically investigated the thermodynamic stability, the structural and electronic properties of $Mo_{1-x}Cr_xS_2$ alloys using the DFT method implemented in the Vienna *ab-initio* simulation package (VASP) [36, 37]. To describe the core electron interactions, projector augmented wave (PAW) pseudopotential [38] were used. The generalized gradient approximation (GGA) exchange correlation parameterized by Perdew, Burke, and Ernzerhof (PBE) [39] was employed to treat the exchange correlation interactions. The supercell size, kinetic energy cut-off and Brillouin zone sampling convergence tests were conducted, and a 5×5 supercell was chosen. A kinetic energy cutoff of 300 eV for the plane wave expansion and $2 \times 2 \times 1$ k-point mesh were used. All the structures were fully relaxed. The convergence threshold was 10^{-5} eV for energies and 2×10^{-2} eV/Å for forces. To suppress interactions between adjacent supercells, a vacuum spacing of 15 Å was constructed in the perpendicular direction.

To examine the relative stability of the distinct possible configurations of $Mo_{1-x}Cr_xS_2$ alloys, the formation energy of each configuration was evaluated. The formation energy (E_{form}) is given by:

$$E_{form} = E_{Mo_{1-x}Cr_xS_2} - (1-x)E_{MoS_2} - xE_{CrS_2}\ , \qquad (2)$$

where $E_{Mo_{1-x}Cr_xS_2}$, E_{MoS_2} and E_{CrS_2} are the total energies of the mixed compound, the pristine MoS_2 and the pristine CrS_2 monolayers, respectively. The x parameter is the concentration of Cr introduced in a MoS_2 monolayer [40].

The different flavors of GGA functional [41, 42, 43, 39, 44] are known to underestimate the energy band gap of a material. In order to improve our band gap values, the hybrid functional of Heyd, Scuseria, and Ernzerhof (HSE06) [45] was also used. At the end of our discussion, we briefly compare the band gap values obtained from GGA functional with those obtained from the HSE functional.

The Cr substitution alloys in a MoS_2 monolayer ($Mo_{1-x}Cr_xS_2$) can be generalized as a binary $A_{1-x}B_x$ alloy. For a perfect random alloy, the correlation function is given by $\prod_{k,m}(R) = (2x-1)^k$, where $k = 2, 3, ...$ indicates the pair (2), triple (3),... correlation functions; $m = 1, 2, 3, ...$ indicates the first, second and third,...,nearest-neighbor distances and x represent the concentration of the substituted atoms [46]. In the SQS method, the sites i occupied by atoms A or B are assigned to a variable σ_i equals to -1 or 1, respectively. The correlation function for this binary alloy can be written as $\prod_{k,m} = \frac{1}{N_{k,m}} \sum_{\{k,m\}} \sigma_1\sigma_2...\sigma_k$, where $N_{k,m}$ is the total number of shape that can be obtained when varying k and m. In the present study, only the nearest-neighbor pairs are scrutinized, since the interactions between far distant neighbors have been reported not to have much effect on the total energy [33]. In this model (nearest neighbor pair), the correlation function

$\Pi_{2,1}$ is given by $\Pi_{2,1} = \frac{1}{N_{bond}} \sum_{j,h=1,N}^{j>h} \sigma_j \sigma_h$, where N_{bond} is the number of bonds between nearest neighbor metals, N is the total number of transition metal in the supercell, j and h represent the two pair sites considered. If the total number of the nearest-neighbor bonds between $A-A$ (Mo-Mo), $B-B$ (Cr-Cr) and $A-B$ (Mo-Cr) atoms are denoted by N_{AA}, N_{BB} and N_{AB}, respectively, the correlation function can be written as :

$$\Pi_{2,1} = \frac{N_{AA} + N_{BB} - N_{AB}}{N_{AA} + N_{BB} + N_{AB}}. \quad (3)$$

The number of atoms A (Mo) and B (Cr) in an $A_{1-x}B_x$ alloy is given by: $N_A = N(1-x)$ and $N_B = Nx$. In addition, assuming that z is the coordination number of atoms in the system, N_A and N_B are related to the number of bonds as:

$$\begin{cases} N_A = \frac{N_{AB}+2N_{AA}}{z} \\ N_B = \frac{N_{AB}+2N_{BB}}{z} \end{cases} \quad (4)$$

Therefore, the correlation function in Eq. 3 becomes :

$$\Pi_{2,1} = 1 - 4x + \frac{8N_{BB}}{Nz}. \quad (5)$$

Thus, Eq. 5 shows that the correlation function can be completely described by N_{BB}. The SQS configurations are considered to have the same correlation functions as the perfect random alloys: $\prod_{2,1}(R) = \prod_{2,1}(SQS)$ [46]. Using this equality and Eq. 5, we found that the number of $N_{BB} = \frac{1}{2}x^2Nz$ in a TMD monolayer. In our study, $N = 25$ and $z = 6$ in a 5×5 supercell of MoS_2 monolayer. It can be shown that at $x = 0.2, 0.4, 0.6$ and 0.8 the $N_{BB} = 3, 12, 27$ and 48 respectively, yielding the SQS random alloy configurations. Many random alloys configurations are possible but the optimum SQS configurations are those that have the same correlation function as the perfect random alloy, i.e, pair, triple, etc.

3. Results and discussion

In order to study the effect of the Cr substitutional dopants on the thermodynamic stability, structural and electronic properties of a MoS_2 monolayer, the physical properties of the pristine MoS_2 and CrS_2 monolayers need to be understood first. In this section, we investigate the structural and electronic properties of these pristine systems. Thereafter, the Cr atoms are introduced into a MoS_2 monolayer by occupying the Mo sites only. An incorporation of the Cr atoms into a MoS_2 monolayer is treated in two cases; firstly, the low Cr concentration has been considered and secondly, the high concentration has been taken into account to form the alloys.

3.1. Pristine MoS_2 and CrS_2 monolayers

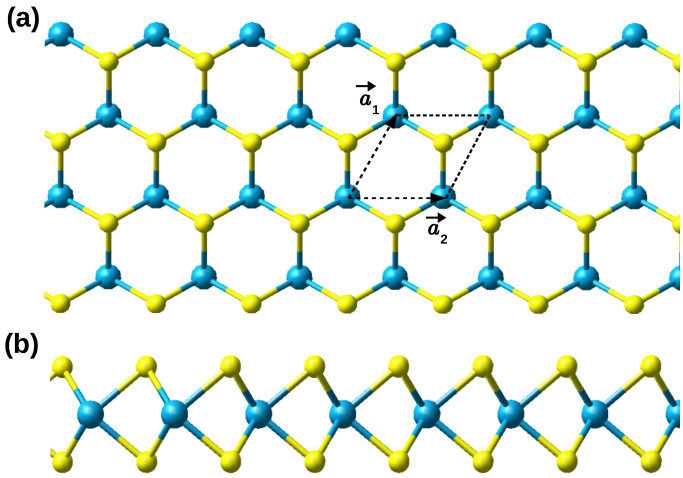

Figure 1: (a) Top view and (b) side view of the 2D TMD MoS_2 or CrS_2. The blue spheres indicate the transition metal atoms and the light yellow spheres indicate the sulfur (S) atoms. $\vec{a_1}$ and $\vec{a_2}$ are the lattice vectors. A unit cell is drawn with dashed lines.

The 2D TMD (MoS_2 and CrS_2) have different polymorphs such as the hexagonal and tetragonal [47]. Previous studies reported that the hexagonal structures of MoS_2 and CrS_2 monolayers are the most stable ones [20]. Top view and side view of the hexagonal TMD monolayer are shown in Fig. 1. The transition metal (Mo or Cr) layer is sandwiched between the two adjacent sulfur (S) layers and form covalent bonds. The transition metal atoms occupy one sublattice of the hexagon and the S atoms occupy the other.

The fully optimized lattice constant for the MoS_2 and CrS_2 monolayers are found to be 3.18 Å and 3.05 Å, respectively. The bond lengths Mo-S and Cr-S are 2.41 Å and 2.29 Å, re-

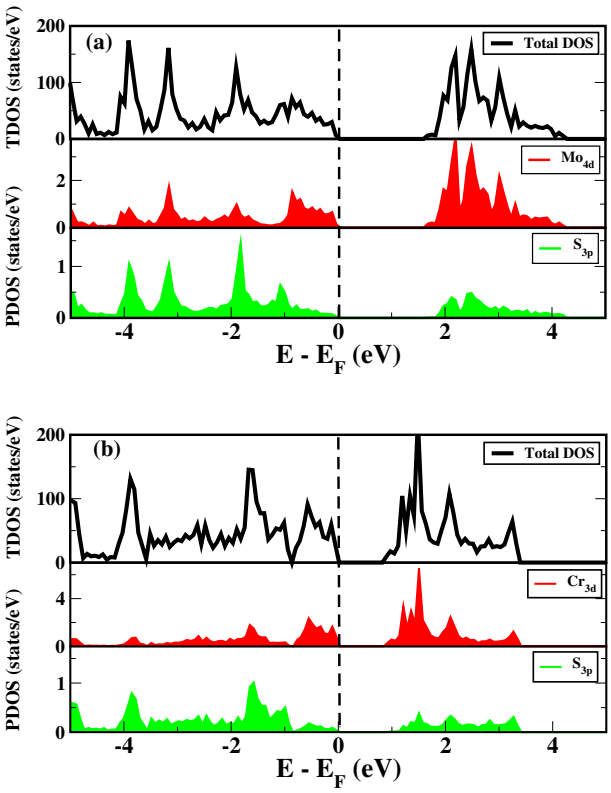

Figure 2: The total density of states (TDOS) for the pristine (a) MoS_2 and (b) CrS_2 monolayers (black lines). The red and green curves are the projected density of states (PDOS) for the transition metal d orbitals and S $3p$ orbitals, respectively. The dashed vertical lines indicate the Fermi level.

spectively. These values agree quite well with the experimental and the previous DFT data [48, 49, 50].

To study the electronic properties of the pristine MoS_2 and CrS_2 monolayers, density of states (DOS) were evaluated. Fig. 2 shows the total DOS (TDOS) for pristine MoS_2 (Fig. 2a) and CrS_2 (Fig. 2b) monolayers. These plots present a gap between the top of the valence band (VBM) and the bottom of the conduction band (CBM) indicating that both the pristine systems are semiconductors. We found that the band gaps of MoS_2 and CrS_2 monolayers are 1.65 eV and 0.86 eV, respectively. These values are consistent with the previous theoretical and experimental data shown in Table. 1. The PDOS in Fig. 2 show that the VBM and CBM states of MoS_2 and CrS_2 monolayers arise mainly from the $4d$ and $3d$ orbitals of the transition metal, respectively. Small contribution from the $3p$ orbitals of the S atoms is noted in both figures. This is in agreement with the results of Dolui *et al*. [55] and Zhuang *et al*. [54].

Table 1: The theoretical and experimental energy band gaps of the pristine MoS_2 and CrS_2 monolayers.

Structure	Method	Band gap (eV)	Ref.
MoS_2	Experimental	1.9	[51]
	Experimental	1.75	[52]
	GGA	1.67	[49]
	GGA	1.65	This work
	HSE	2.25	[49]
	HSE	2.14	[53]
	HSE	2.17	This work
CrS_2	GGA	0.89	[33]
	GGA	0.86	This work
	HSE	1.48	[54]
	HSE	1.31	This work

Spin polarized calculations were carried out for all of the calculations in this paper. However, the majority spin DOS are symmetrical to the minority spin DOS, indicating that the systems are non magnetic in nature [33, 56]. Therefore, we only show the DOS for spin-up channel, for the entire paper.

3.2. *Isolated Cr dopants in a MoS_2 monolayer*

Next, we examine the effect of isolated (I) one and two Cr dopants on the thermodynamic stability, structural and electronic properties of a MoS_2 monolayer. As mentioned earlier, the Mo and S atoms occupy different sublattices of the hexagonal MoS_2 monolayer as shown in Fig. 1.

The Mo atoms occupy one sublattice for the entire structure, and due to the symmetry of the system, we only have one possible unique configuration for single Cr doping shown in Fig. 3a called $C_{1(I)}$. However, in the case of the two Cr dopants, different configurations are possible. All the distinct configurations of the two Cr dopants are shown in Fig. 3(b-e), namely configurations $C_{2(I)}$, $C_{3(I)}$, $C_{4(I)}$ and $C_{5(I)}$. Configuration $C_{2(I)}$ is constructed by introducing the two Cr atoms at the Mo sites within the same hexagonal ring-like in a 5×5 supercell of a MoS_2 monolayer. These two dopants are first nearest neighbor to each other (see Fig. 3b). The second possible configuration

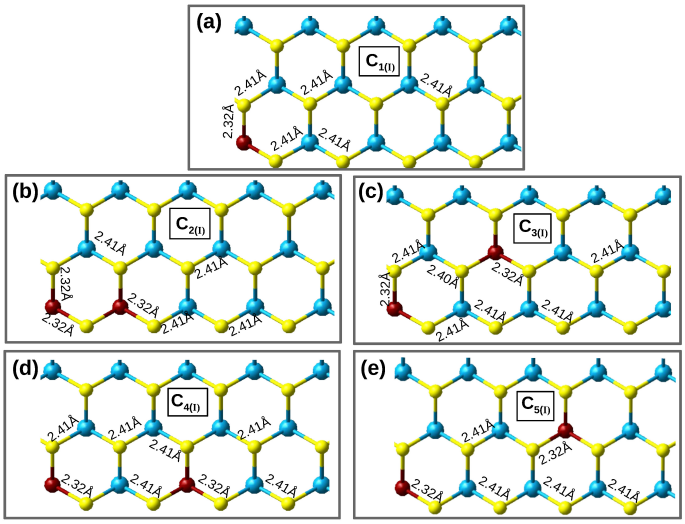

Figure 3: (a) The relaxed structure of a single Cr doping in a MoS_2 monolayer. The various configurations of the two Cr dopants (b) $C_{2(I)}$, (c) $C_{3(I)}$, (d) $C_{4(I)}$ and (e) $C_{5(I)}$. The blue, red and light yellow spheres indicate the Mo, Cr and S atoms, respectively.

$C_{3(I)}$ involves the second hexagonal ring-like. $C_{3(I)}$ is obtained when the second Cr atom is the second nearest neighbor of the first Cr atom (see Fig. 3c). Configuration $C_{4(I)}$ is obtained when the second Cr atom is placed as the third nearest neighbor with the first Cr atom (see Fig. 3d). The last configuration $C_{5(I)}$ is obtained when the second atom is the forth nearest neighbor of the first Cr atom (see Fig. 3e) considering only the Mo sites.

In order to study the stability of these different configurations, we calculated the formation energies using Eq. 2. The formation energy for $C_{1(I)}$ is 2 meV, revealing an endothermic reaction. Fig. 4 summarizes the formation energies for the different configurations of the two dopants in a MoS_2 monolayer ($C_{2(I)}$, $C_{3(I)}$, $C_{4(I)}$ and $C_{5(I)}$). It can be seen that $C_{4(I)}$ has the highest formation energy, while $C_{2(I)}$ possessing the lowest. We realize that the Cr-doped system becomes more unstable when the Cr atoms move farther away from each other. Thus, this is an evidence that the two Cr dopants prefer to be closer to each other in a MoS_2 supercell, when considering the Mo sites only. Although positive, the formation energies shown in Fig. 4 are very low, suggesting that Cr-doped configurations can form under reasonable conditions.

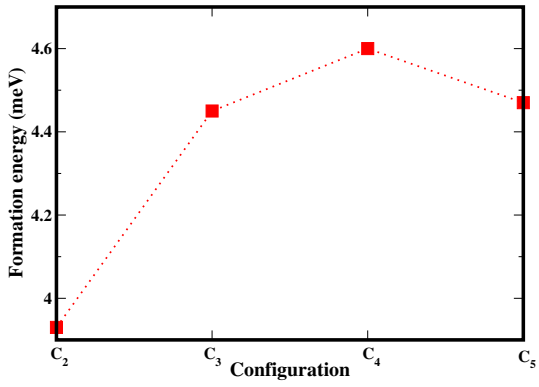

Figure 4: The formation energies for distinct configurations of the two dopants in a MoS_2 monolayer. Along the x axis, configurations $C_{2(I)}$, $C_{3(I)}$, $C_{4(I)}$ and $C_{5(I)}$ denote the first, second, third and forth nearest neighbor Cr atoms.

In all configurations considered, the Cr-S bond distance is 0.10 Å on average lower than the initial bond length of the MoS_2 monolayer. Various bond lengths can be read from Fig. 3. This relatively small value reveals that Cr does not cause significant structural distortions in a MoS_2 monolayer.

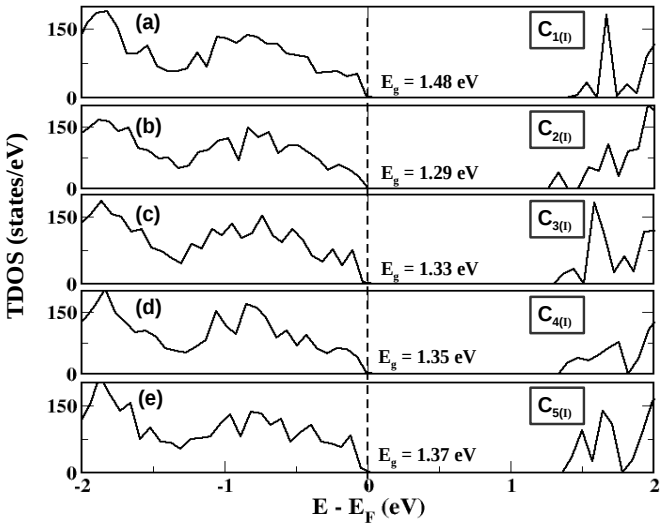

Figure 5: (a) The TDOS of single Cr doping in a MoS_2 monolayer ($C_{1(I)}$). The TDOS of the configurations (b) $C_{2(I)}$, (c) $C_{3(I)}$, (d) $C_{4(I)}$ and (e) $C_{5(I)}$. The black dashed vertical lines indicate the Fermi level.

Fig. 5 presents the TDOS of our distinct Cr configurations in a MoS_2 monolayer. It is found that the incorporation of the Cr dopants preserves the semiconducting properties of MoS_2 monolayer but reduces the band gap of the system significantly. Even at a very low concentration of 4% Cr dopant (one Cr

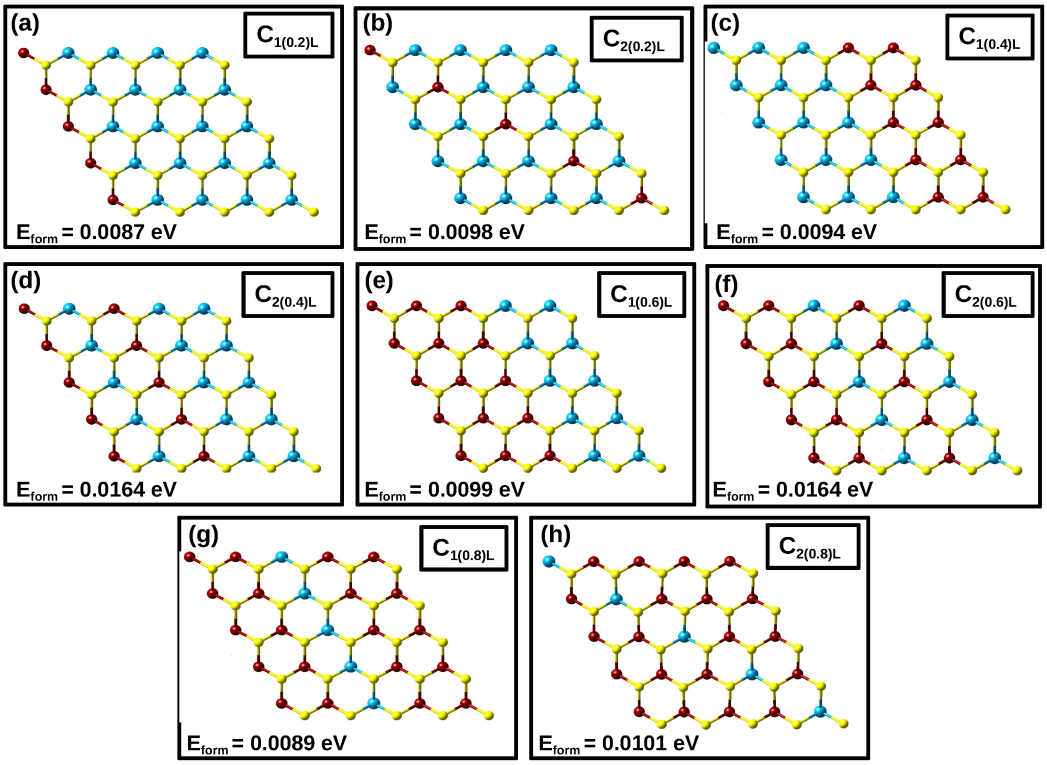

Figure 6: All the possible configurations of line-ordered alloys of $Mo_{1-x}Cr_xS_2$ at each concentration. Configurations (a) $C_{1(0.2)L}$ and (b) $C_{2(0.2)L}$ correspond to 20%, (c) $C_{1(0.4)L}$ and (d) $C_{2(0.4)L}$ to 40%, (e) $C_{1(0.6)L}$ and (f) $C_{2(0.6)L}$ to 60%, and (g) $C_{1(0.8)L}$ and (h) $C_{2(0.8)L}$ to 80% of the Cr atoms. The blue, red and yellow spheres represent the Mo, Cr and S atoms, respectively. The formation energy (E_{form}) of each configuration obtained using Eq. 2 is shown at the bottom of each diagram.

dopant), the band gap has been reduced from 1.65 eV (pristine MoS_2) to 1.48 eV. Comparing different configurations of the two dopants, it is noted that the most stable configuration $C_{2(I)}$ has the smallest band gap (see Fig. 5b), while $C_{5(I)}$ possessing the largest (see Fig. 5e). Revealing that the band gap can be fine tuned by variation of the distance between the two Cr dopants.

Since these preliminary results suggest that the Cr atoms prefer to be closer to each other, it is important to examine the effect of Cr dopants at high concentrations. In this study, the Cr line-ordered alloy and random alloy at different concentrations and in various configurations are studied. This is further supported by Lewis *et al*. [57] who reported that Cr substituting Mo in a MoS_2 monolayer can be synthesized at high concentration.

3.3. Line-ordered and random alloys of Cr atoms in a MoS_2 monolayer

3.3.1. Thermodynamic stability and structural properties of $Mo_{1-x}Cr_xS_2$ alloys

As mentioned earlier, simulation of the alloys in a layered systems is a great challenge due to thousands of possible atomic arrangements. In this section, a systematic study of Cr line-ordered alloys and random alloys has been considered. Five concentrations ($x = 0.2, x = 0.4, x = 0.6$ and $x = 0.8$ correspond to 20%, 40%, 60%, 80% and 100% Cr atoms) have been chosen.

To create the line-ordered alloys, we substitute the Mo atoms in a MoS_2 monolayer with the Cr atoms at different concentrations, along a particular direction (zigzag and diagonal). At each concentration, distinct configurations are identified and examined. All the possible Cr configurations are shown in Fig. 6 named $C_{1(0.2)L}$, $C_{2(0.2)L}$, $C_{1(0.4)L}$, $C_{2(0.4)L}$, $C_{1(0.6)L}$, $C_{2(0.6)L}$,

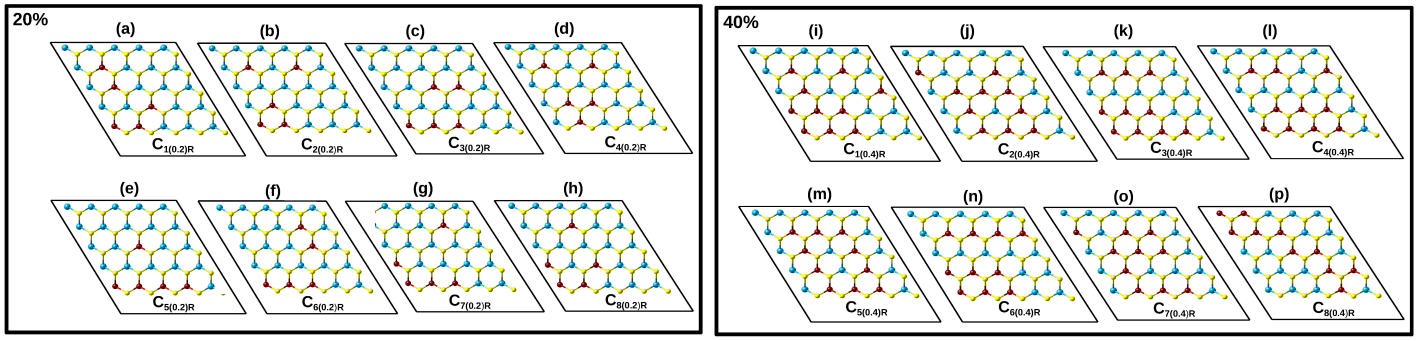

Figure 7: Various selected unique Cr random alloy configurations at 20% of Cr atoms (left panel): (a) $C_{1(0.2)R}$, (b) $C_{2(0.2)R}$, (c) $C_{3(0.2)R}$, (d) $C_{4(0.2)R}$, (e) $C_{5(0.2)R}$, (f) $C_{6(0.2)R}$, (g) $C_{7(0.2)R}$ and (h) $C_{8(0.2)R}$. Those obtained at 40% (right panel) are : (i) $C_{1(0.4)R}$, (j) $C_{2(0.4)R}$, (k) $C_{3(0.4)R}$, (l) $C_{4(0.4)R}$, (m) $C_{5(0.4)R}$, (n) $C_{6(0.4)R}$, (o) $C_{7(0.4)R}$ and (p) $C_{8(0.4)R}$. At 60% and 80% concentrations, the selected configurations are the same as those obtained at 40% and 20%, respectively, but with transition metals swapped. The blue, red and yellow spheres represent the Mo, Cr and S atoms, respectively.

$C_{1(0.8)L}$ and $C_{1(0.8)L}$. To avoid repetition, the periodic boundary conditions are always taken into account when constructing the line-ordered alloys. Configurations $C_{1(0.2)L}$ and $C_{2(0.2)L}$ correspond to 20% of the Cr atoms. Configuration $C_{1(0.2)L}$ is obtained when the Cr atoms are placed along a zigzag path of the hexagonal MoS_2 monolayer occupying the same Mo sublattice (see Fig. 6a) and configuration $C_{2(0.2)L}$ is formed by substituting the Mo atoms along the diagonal of the supercell, also occupying the same Mo sites (see Fig. 6b).

Configurations $C_{1(0.4)L}$ and $C_{2(0.4)L}$ correspond to 40% of the Cr atoms. In $C_{1(0.4)L}$, the Cr atoms constitute two adjacent parallel lines along the zigzag path (see Fig. 6c). Configuration $C_{2(0.4)L}$ is constructed by two lines of the Cr atoms along the zigzag, but separated by a line of the Mo atoms (see Fig. 6d). At 40% concentration, the line-ordered alloy along the diagonal is not possible. Following the same pattern, configurations $C_{1(0.6)L}$ and $C_{2(0.6)L}$ are identified in 60% concentration (see Fig. 6e and Fig. 6f). Lastly, configurations $C_{1(0.8)L}$ and $C_{2(0.8)L}$ are obtained when 80% of the Cr atoms substitute the Mo atoms. These configurations are similar to those of $C_{1(0.2)L}$ and $C_{2(0.2)L}$ but the transition metal elements are swapped (as shown in Fig. 6g and Fig. 6h). It is clear that at each Cr concentration, only two distinct line-ordered alloy configurations are possible.

For random alloys, many unique configurations at each concentration are identified using SQS method. Fig. 7 presents the selected unique configurations at 20% and 40% concentrations. For a perfect alloy (optimum pair correlation function of the SQS) at 20% concentration, three Cr-Cr bonds (N_{BB} = 3) should be formed at each configuration as described in the methodology. For instance in configuration $C_{1(0.2)R}$ shown in Fig. 7a, the three Cr atoms adjacent to each other form two Cr-Cr bonds (N_{BB}) and the third Cr-Cr bond is formed relatively far away. In configuration $C_{2(0.2)R}$, three of the introduced Cr atoms substitute the three Mo atoms in the hexagonal ringlike showing a triangular arrangement, forming the required three bonds (Fig. 7b). The remaining two Cr atoms do not necessarily need to form N_{BB} (Cr-Cr bond). Following the same procedure, configurations $C_{3(0.2)R}$, $C_{4(0.2)R}$, $C_{5(0.2)R}$, $C_{6(0.2)R}$, $C_{7(0.2)R}$ and $C_{8(0.2)R}$ are also identified. The same procedure (SQS model for nearest-neighbor pair) has been applied at 40% concentration. Hence, at 40%, the required N_{BB} = 12 has been met and all the identified configurations are also presented in Fig. 7. At 60% and 80% concentrations, all the selected configurations are the same as those obtained at 40% and 20%, respectively, but with transition metals swapped. Some of our configurations are the same as those in ref. [58] for $Mo_{(1-x)}W_xS_2$.

In order to compare the relative stabilities of the Cr line-ordered alloys and random alloys, we have calculated the formation energies using Eq. 2. The calculated formation energies of the line-ordered alloys are presented in the bottom of each diagram in Fig. 6. Although formation of the Cr line-ordered alloys seems to be endothermic (positive formation en-

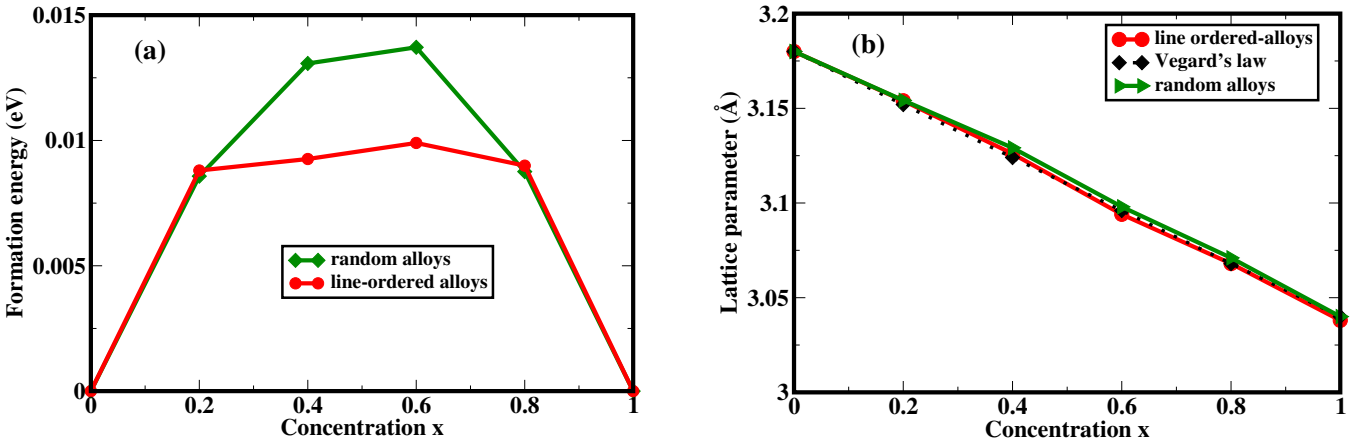

Figure 8: (a) The calculated formation energies of the lowest energy configurations for the Cr line-ordered alloys and random alloys at different concentrations. (b) The lattice constant for $Mo_{1-x}Cr_xS_2$ alloys at different concentrations. The red line connects the lowest energy configurations for the line-ordered alloys while the green line connects those for the Cr random alloys.

ergy), their magnitude values are relatively very small, suggesting that formation of the Cr alloys in a MoS_2 monolayer can be spontaneous. Comparing the formation energies of the line-ordered alloy configurations at each concentration, we found that $C_{1(0.2)L}$, $C_{1(0.4)L}$, $C_{1(0.6)L}$ and $C_{1(0.8)L}$ are energetically the most stable configurations at 20%, 40%, 60% and 80%, respectively. Configuration $C_{1(0.2)L}$ is 1.1 meV lower than $C_{2(0.2)L}$ in energy at 20% concentration. Since the separations between the Cr atoms are larger in configuration $C_{2(0.2)L}$ than in configuration $C_{1(0.2)L}$, this observation suggests that the interaction of Cr alloys in a MoS_2 monolayer is desirable. Moreover, the major driving force on the stability of these systems is the concentration, because Fig. 8a shows a parabolic curve revealing that the formation energies of the configurations rise with the increase in Cr or Mo concentration. At 40%, it is noted that configuration $C_{1(0.4)L}$ is more energetically favorable than configuration $C_{2(0.4)L}$. This emphasize an idea that the Cr atoms prefer to be grouped together. It can be seen that when the two Cr lines alloys are separated by a line of the Mo atoms (see Fig. 6d), the relative stability of configuration $C_{1(0.4)L}$ reduces significantly. This trend is also noted in 60% of the Cr atoms. In configuration $C_{1(0.6)L}$, three Cr lines alloy are grouped together (see Fig. 6e) but in configuration $C_{2(0.6)L}$, three Cr lines alloy are separated by a line of the Mo atoms (see Fig. 6f). We observe that configuration $C_{1(0.6)L}$ is more energetically favorable than configuration $C_{2(0.6)L}$. At 80% concentration, we note the same behavior as that of 20%. This is not surprising because in 80% concentration, the Cr atoms occupy the sites of Mo in 20%.

Table. 2 presents the stability of the various Cr random alloy configurations. Just like in the line-ordered alloys, the formation energies of all configurations are positive. Although positive formation energies indicate that $Mo_{1-x}Cr_xS_2$ would prefer segregation at 0K [33], their magnitudes are very small suggesting that they can form at temperatures of few degrees Celsius. These Cr random alloys are plausible structures and some of these configurations were synthesized at low concentra-

Table 2: Formation energies of the selected unique Cr random alloy configurations at different concentrations x. The bold values represent the lowest energy configurations at each concentration.

	Formation energies (eV)			
Conf.	$x = 0.2$	$x = 0.4$	$x = 0.6$	$x = 0.8$
C_{1R}	**0.0086**	0.0139	0.0149	**0.0090**
C_{2R}	0.0104	0.0181	0.0169	0.0997
C_{3R}	0.0089	0.0149	0.0147	0.0122
C_{4R}	0.0103	0.0144	0.0146	0.0119
C_{5R}	0.0102	0.0185	0.0179	0.0124
C_{6R}	0.0095	**0.0130**	**0.0145**	0.0095
C_{7R}	0.0097	0.0182	0.0169	0.0091
C_{8R}	0.0100	0.0167	0.0161	0.0124

tion [57]. The thermodynamic stability of these alloys greatly depends on the Cr pair coordination (Cr-Cr), see the lowest energy configuration $C_{1(0.2)R}$ shown in Fig. 7a. Apart from $C_{1(0.2)R}$ and $C_{3(0.2)R}$, all other configurations have slighty high formation energies since they possess an unpaired Cr atoms. This is in agreement with Wei *et al*. [33] who reported that the long distance neighbors interaction contribute less energy than nearest-neighbor. Following the pair correlation function, the same behavior is noted at 40% concentration. The most energetically favorable configuration at 40% concentration, $C_{6(0.4)R}$ is shown in Fig. 7n. In this configuration, it is noted that all the Cr atoms are paired showing N_{BB} correlation. All the selected configurations at 60% behave as those at 40%. Similar finding is observed also for 20% and 80% concentrations. Configurations $C_{6(0.6)R}$ and $C_{1(0.8)R}$ to be the most stable at 60% and 80% reveal that even Mo alloys in CrS_2 monolayer would prefer pair coordination.

The formation energies of the most stable structures at each concentration for the two types of alloys considered are plotted in Fig. 8a. We found that at $x = 0.2$ and $x = 0.8$, the energy difference between the Cr line-ordered alloys and Cr random alloys are very small. This might originates from the fact that in both configurations $C_{1(0.2)L}$ and $C_{1(0.2)R}$, the Cr atoms are completely paired to each other enhancing the stability. However, at $x = 0.4$ and $x = 0.6$, the line-ordered alloys have significant lower formation energy than the random alloys. The most stable configurations for the Cr line-ordered alloys $C_{1(0.4)L}$ and $C_{1(0.6)L}$ present a continuous Cr atom pair coordination, whereas in the Cr random alloy configurations ($C_{6(0.4)R}$ and $C_{6(0.6)R}$), there is a Mo line separating the group of paired Cr atoms compromising the stability. Therefore, our results reveal that the line-ordered alloys are plausible structures and can be synthesized at the same conditions as random alloy structures.

We now study the effect of the Cr line-ordered alloys and random alloys on the structural properties of a MoS_2 monolayer. After full relaxation, we note that the incorporation of the Cr atoms into MoS_2 monolayer preserves the hexagonal symmetry of the system but the area changes due to the change in lattice constants. Fig. 8b shows how lattice constants of $Mo_{1-x}Cr_xS_2$ alloys change as a function of Cr concentration. We find that the values of the lattice constants for the alloys range between those of pristine MoS_2 and CrS_2 monolayers in both cases. It is also noted in Fig. 8b that the lattice constants of the configurations are inversely proportional to the Cr concentration. This reduction is specifically due to the smaller atomic radius of Cr atom compared to that of Mo atom. The atomic radii of Cr and Mo are 166 picometers and 190 picometers, respectively [59].

Usually, the physical properties (e.g. lattice constant and band gap) of an alloy $Mo_{1-x}Cr_xS_2$ as a function of the dopants concentration x are described by the following quadratic equation [25, 31, 60]:

$$P(x) = (1 - x)P(MoS_2) + xP(CrS_2) - bx(1 - x)\,, \qquad (6)$$

where $P(MoS_2)$ and $P(CrS_2)$ are the physical properties of the pristine MoS_2 and CrS_2 monolayers, respectively and b is called bowing parameter. It characterizes the degree of deviation from linearity trend.

If b in Equation. 6 is equal to zero, the so called Vergard's law is obeyed. This law states that there is a linear relationship between the physical properties of a host material and the concentration of alloys [61, 31]. Then Eq. 6 reduces to:

$$P(x) = xP(NX_2) + (1 - x)P(MX_2)\,. \qquad (7)$$

We plotted in Fig. 8b the lattice constants of the lowest energy configurations for the line-ordered alloys and random alloys as a function of Cr concentration. For comparison purpose, we have plotted also in Fig. 8b, the lattice constants of the alloys using Eq. 7. We note that the three plots, for the random and line-ordered alloys and Eq. 7, are superimposed on top of each other. It can also be seen in Fig. 8b that the lattice parameters change almost linearly with the Cr concentration. This characteristic of the line-ordered and random alloys obeys Vergard's law.

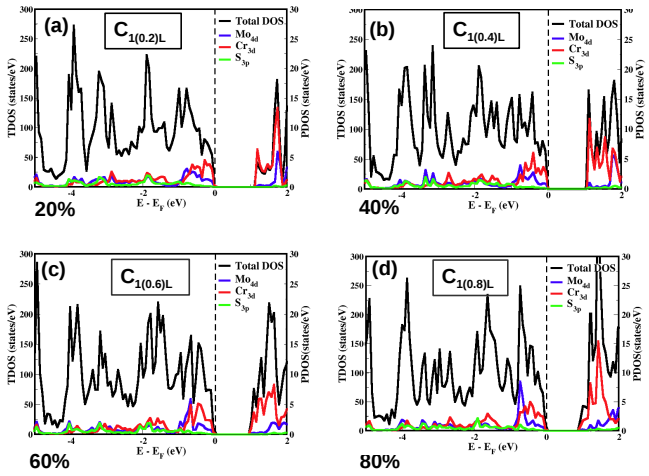

Figure 9: TDOS and PDOS of the stable structures for the Cr line-ordered alloys in a MoS_2 monolayer: (a) $C_{1(0.2)L}$, (b) $C_{1(0.4)L}$, (c) $C_{1(0.6)L}$ and (d) $C_{1(0.8)L}$. The black dashed vertical lines indicate the Fermi level.

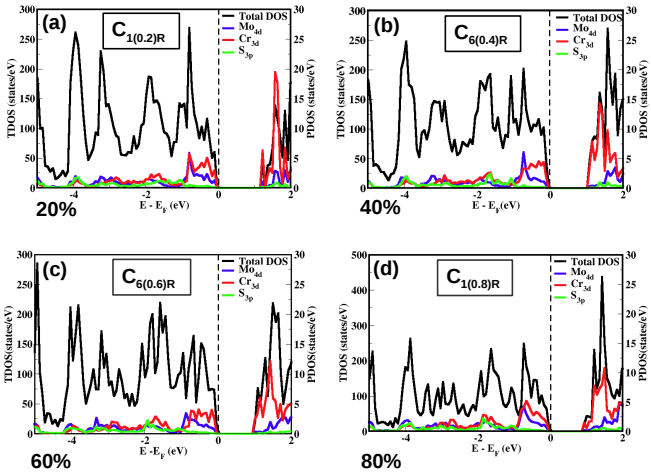

Figure 10: TDOS and PDOS of the stable structures for the Cr random alloys in a MoS_2 monolayer: (a) $C_{1(0.2)R}$, (b) $C_{6(0.4)R}$, (c) $C_{6(0.6)R}$ and (d) $C_{1(0.8)R}$. The black dashed vertical lines indicate the Fermi level.

3.3.2. *Electronic properties of $Mo_{1-x}Cr_xS_2$ alloys*

To examine the electronic properties of the $Mo_{1-x}Cr_xS_2$ alloys, DOS calculations were carried out. Fig. 9 and Fig. 10 show the TDOS and PDOS of the stable structures at 20%, 40%, 60% and 80% of the Cr atoms for the line-ordered alloys and random alloys, respectively. We find that these two types of alloys significantly fine tune the band gap of a MoS_2 monolayer. For all Cr concentrations considered, the semiconducting behavior of a MoS_2 monolayer is preserved but the band gap is reduced.

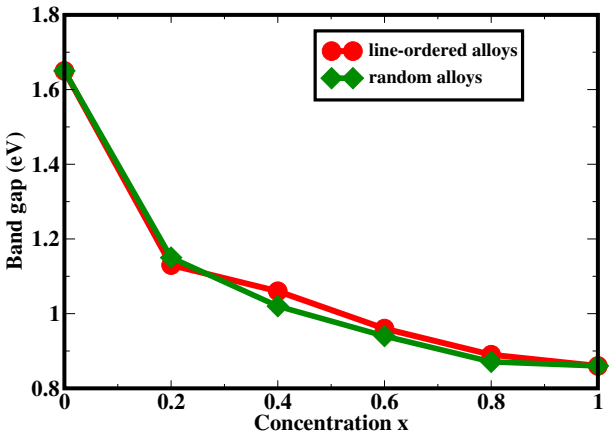

Figure 11: The band gaps of $Mo_{1-x}Cr_xS_2$ line-ordered alloys and random alloys as a function of Cr concentration. Red line connects the band gaps of the most energetically favorable configurations for the line-ordered alloys at each concentration $C_{1(0.2)L}$, $C_{1(0.4)L}$, $C_{1(0.6)L}$ and $C_{1(0.8)L}$, while the green line connects those for the random alloys $C_{1(0.2)R}$, $C_{6(0.4)R}$, $C_{6(0.6)R}$ and $C_{1(0.8)R}$.

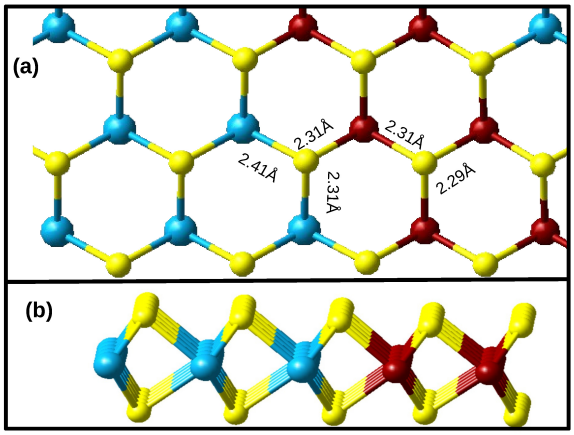

Figure 12: (a)Top view of $Mo_{1-x}Cr_xS_2$ line-ordered alloys showing the deviation in bond lengths due to Cr atoms. (b) Side view of the same $Mo_{1-x}Cr_xS_2$ structure. The blue, red and yellow spheres indicate the Mo, Cr and S atoms, respectively.

Fig. 11 presents the band gap values of the $Mo_{1-x}Cr_xS_2$ alloys calculated at different Cr concentrations. We find that the band gap decreases when the Cr concentration increases. The reason might be due to the inward strain along the *xy*-plane induced by small atomic radii of the Cr atoms compared to those of Mo atoms. No Cr buckling is noted along the *z*-axis of

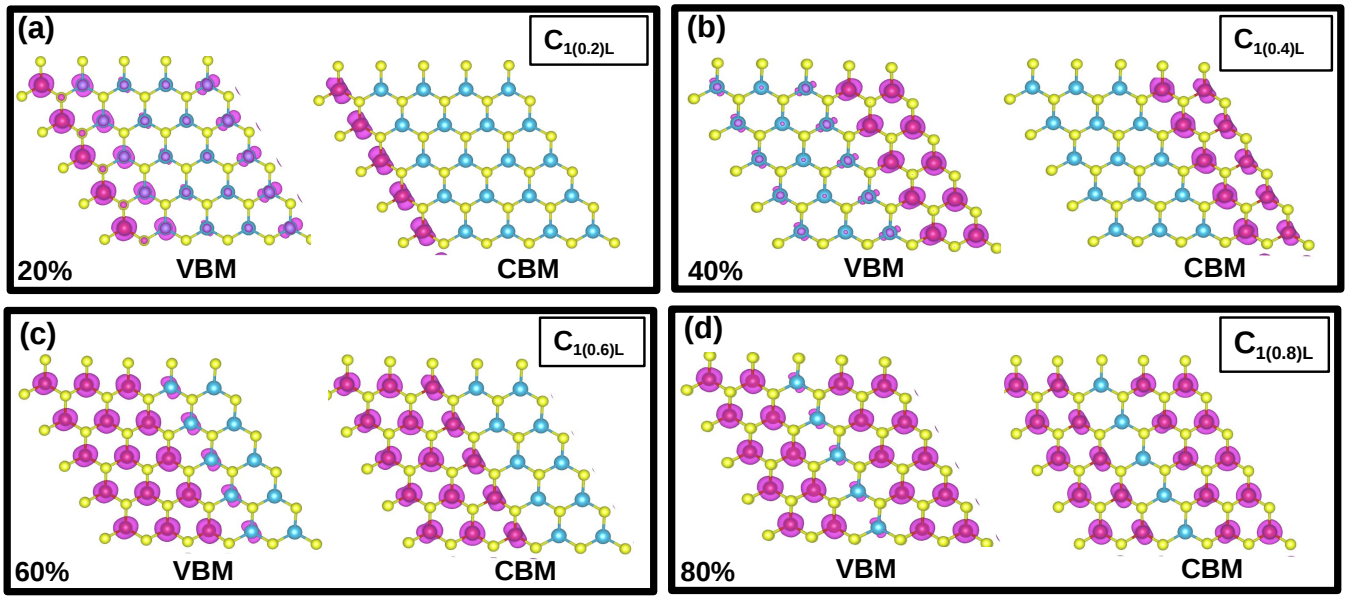

Figure 13: Partial charge densities of the VBM and CBM for the lowest energy line-ordered alloy configurations at (a) 20%, (b) 40%, (c) 60% and (d) 80% Cr concentrations.

the MoS_2 monolayer (see Fig. 12b). Bond lengths of the line-ordered alloys are displayed in Fig. 12a . The relaxed Cr-S bond length is about 2.31 Å on average (same for both line-ordered alloys and random alloys). This value is 0.1 Å less than that of Mo-S of about 2.41 Å. The deviation in bond lengths should be responsible for reduction of the MoS_2 monolayer band gap as well as the lattice constant. This is opposite to the previous result on isovalent substitution $Mo_xW_{1-x}S_2$, where the band gap increases with the concentration of W atoms [28]. The band gap of $Mo_{1-x}Cr_xS_2$ line-ordered alloys as well as random alloys range between 1.65 ($x = 0$) and 0.86 eV ($x = 1$). This range of band gap is suitable for solar spectrum and thus tuning the band gap of a MoS_2 monolayer has an important role in the solar energy conversion [53]. These values might improve when using other exchange-correlation functionals such as HSE or Green's function (GW) [62].

Subsequently, in order to study the contribution of the Cr orbital states on the reduction of band gap, we analyze the PDOS for stable configurations at 20%, 40%, 60% and 80% shown in Fig. 9 and Fig. 10. This is to examine if there is any hybridization of Cr, Mo and S orbitals. For all cases, it is noted that the 4*d* orbitals of the Mo atoms and 3*d* orbitals of the Cr atoms are the major contributors for the VBM. The 3*p* orbitals of the S atoms also contribute for the VBM but in a small magnitude. We also find that CBM state is mainly contributed by the 3*d* orbitals of the Cr atoms. These Cr 3*d* orbitals states get more populated at the band edges when the Cr concentration increases, thus reducing the band gap significantly as shown in Fig. 9d and Fig. 10d. We further analyze the partial charge density distribution for VBM and CBM states for the lowest energy line-ordered alloy configurations shown in Fig. 13. It is noted indeed that the VBM state is mainly dominated by Mo and Cr charge densities (see Fig. 13a). The small cloud of charge on the S atoms next to Cr atoms is also noted. On the other hand, the CBM state only arises from the Cr atoms charge density at each concentration. These partial charge densities results confirm the PDOS analysis.

The GGA exchange correlation is known to severely underestimate the band gap of a real material. In order to check the reliability of our previous GGA calculations, we have calculated the TDOS using HSE functional. For the pristine MoS_2 and CrS_2 monolayers, our HSE band gaps are 2.17 eV and 1.31 eV.

Our results are in agreement with the previously reported HSE values (as shown in Table. 1). Compared to the experimental data, HSE overestimates the band gap of MoS_2 monolayer (∼+0.25 eV). Due to the high computational cost consuming of the HSE calculations, we calculated the band gaps of lowest energy configurations. At 20% of the Cr atoms, the HSE band gap is 1.62 eV (1.71 eV) for line-ordered (random) alloys more than the GGA value by 0.49 eV (0.64 eV). At 40%, a HSE band gap of 1.53 eV (1.52 eV) has been obtained also more than the GGA predicted value. Although HSE values are more than the GGA values in magnitude, their trends are the same. This suggests that GGA functional can qualitatively describe the line-ordered alloys in a MoS_2 monolayer. Our results suggest that $Mo_{1-x}Cr_xS_2$ line-ordered alloys are essential for nanotechnology devices.

4. Conclusions

In conclusion, using a DFT approach, we have successfully performed a comparative study of the thermodynamic stability, structural and electronic properties of $Mo_{1-x}Cr_xS_2$ line-ordered alloys and random alloys. The lowest energy configuration has been identified at each concentration to predict new plausible materials for nanotechnological device applications. The line-ordered alloys are constantly lower in formation energies than the random alloys at each concentration. Generally, the formation energies for all configurations are found to be very small (close to zero) suggesting that the $Mo_{1-x}Cr_xS_2$ alloys can be synthesized under ambient conditions.

Interestingly, both the line-ordered alloys and random alloys fine tuned the band gap of a MoS_2 monolayer. The Cr concentrations are found to be the major driving force in tuning the band gap of a MoS_2 monolayer. The small atomic radii of the Cr atoms compared to those of Mo atoms induces inward strain in the structure affecting the electronic properties of the MoS_2 monolayer. The hybridization of the Cr $3d$ and Mo $4d$ orbitals occurs at the vicinity of the band edges resulting in the reduction of the band gap. The magnitude of the $Mo_{1-x}Cr_xS_2$ alloys band gap values obtained from GGA and HSE functionals meets the requirements for solar energy conversion and nanotechnological devices applications. The further study of line-ordered alloys is encouraged for other TMD, both theoretically and experimentally.

Acknowledgment

The authors acknowledge the University of Pretoria for financial and computational resources support. REM and NC are also grateful to NRF and NITheP for financial support. We also thank R.C. Andrew and O. Olaniyan for useful discussions.

References

[1] A. K. Geim, K. S. Novoselov, The rise of graphene, Nature materials 6 (3) (2007) 183–191. doi:10.1038/nmat1849.

[2] K. Novoselov, D. Jiang, F. Schedin, T. Booth, V. Khotkevich, S. Morozov, A. Geim, Two-dimensional atomic crystals, Proceedings of the National Academy of Sciences of the United States of America 102 (30) (2005) 10451–10453. doi:10.1073/pnas.0502848102.

[3] H. Zhang, Ultrathin two-dimensional nanomaterials, ACS nano 9 (10) (2015) 9451–9469. doi:10.1021/acsnano.5b05040.

[4] A. C. Neto, F. Guinea, N. M. Peres, K. S. Novoselov, A. K. Geim, The electronic properties of graphene, Reviews of modern physics 81 (1) (2009) 109. doi:10.1103/revmodphys.81.109.

[5] M. Xu, T. Liang, M. Shi, H. Chen, Graphene-like two-dimensional materials, Chemical reviews 113 (5) (2013) 3766–3798. doi:10.1021/cr300263a.

[6] K. S. Novoselov, A. K. Geim, S. V. Morozov, D. Jiang, Y. Zhang, S. V. Dubonos, I. V. Grigorieva, A. A. Firsov, Electric field effect in atomically thin carbon films, science 306 (5696) (2004) 666–669. doi:10.1126/science.1102896.

[7] O. Olaniyan, R. Mapasha, D. Momodu, M. Madito, A. Kahleed, F. Ugbo, A. Bello, F. Barzegar, K. Oyedotun, N. Manyala, Exploring the stability and electronic structure of beryllium and sulphur co-doped graphene: a first principles study, RSC Advances 6 (91) (2016) 88392–88402. doi:10.1039/C6RA17640B.

[8] A. Hussain, S. Ullah, M. A. Farhan, Fine tuning of band-gap of graphene by atomic and molecular doping: A density functional theory study, RSC Advancesdoi:10.1039/c6ra04782c.

[9] P. Rani, V. Jindal, Designing band gap of graphene by B and N dopant atoms, RSC Advances 3 (3) (2013) 802–812. doi:10.1039/c2ra22664b.

[10] J. O. Sofo, A. S. Chaudhari, G. D. Barber, Graphane: a two-dimensional hydrocarbon, Physical Review B 75 (15) (2007) 153401. doi:10.1103/physrevb.75.153401.

[11] X. Gao, Z. Wei, V. Meunier, Y. Sun, S. B. Zhang, Opening a large band gap for graphene by covalent addition, Chemical Physics Letters 555 (2013) 1–6. doi:10.1016/j.cplett.2012.10.069.

[12] D. Pacile, J. Meyer, C. O. Girit, A. Zettl, The two-dimensional phase of boron nitride: few-atomic-layer sheets and suspended membranes, Applied Physics Letters 92 (13) (2008) 133107. doi:10.1063/1.2903702.

[13] Q. H. Wang, K. Kalantar-Zadeh, A. Kis, J. N. Coleman, M. S. Strano, Electronics and optoelectronics of two-dimensional transition metal dichalcogenides, Nature nanotechnology 7 (11) (2012) 699–712. doi:10.1038/nnano.2012.193.

[14] A. Kuc, T. Heine, A. Kis, Electronic properties of transition-metal dichalcogenides, MRS Bulletin 40 (07) (2015) 577–584. doi:10.1557/mrs.2015.143.

[15] B. Radisavljevic, A. Radenovic, J. Brivio, i. V. Giacometti, A. Kis, Single-layer MoS_2 transistors, Nature nanotechnology 6 (3) (2011) 147–150. doi:10.1038/nnano.2010.279.

[16] H. Zeng, J. Dai, W. Yao, D. Xiao, X. Cui, Valley polarization in MoS_2 monolayers by optical pumping, Nature nanotechnology 7 (8) (2012) 490–493. doi:10.1038/nnano.2012.95.

[17] A. Castellanos-Gomez, M. Poot, G. A. Steele, H. S. van der Zant, N. Agraït, G. Rubio-Bollinger, Elastic properties of freely suspended MoS_2 nanosheets, Advanced Materials 24 (6) (2012) 772–775. doi:10.1002/adma.201103965.

[18] N. izyumskaya, D. O. Demchenko, V. Avrutin, Ü. ÖZGÜR, H. MorkoÇ, Two-dimensional MoS_2 as a new material for electronic devices, Turkish Journal of Physics 38 (3) (2014) 478–496. doi:10.3906/fiz-1407-16.

[19] H. Wang, H. Yuan, S. S. Hong, Y. Li, Y. Cui, Physical and chemical tuning of two-dimensional transition metal dichalcogenides, Chemical Society Reviews 44 (9) (2015) 2664–2680. doi:10.1039/c4cs00287c.

[20] C. Ataca, H. Sahin, S. Ciraci, Stable, single-layer MX_2 transition-metal oxides and dichalcogenides in a honeycomb-like structure, The Journal of Physical Chemistry C 116 (16) (2012) 8983–8999. doi:10.1021/jp212558p.

[21] M. Berger, Nanotechnology: The Future is Tiny, Royal Society of Chemistry, 2016.

[22] X. Li, H. Zhu, Two-dimensional MoS_2: Properties, preparation, and applications, Journal of Materiomics 1 (1) (2015) 33–44. doi:10.1016/j.jmat.2015.03.003.

[23] I. Vurgaftman, J. Meyer, L. Ram-Mohan, Band parameters for III–V compound semiconductors and their alloys, Journal of applied physics 89 (11) (2001) 5815–5875. doi:10.1063/1.1368156.

[24] M. Ameri, A. Bentouaf, M. Doui-Aici, R. Khenata, F. Boufadi, A. Touia, et al., Structural and electronic properties calculations of $Al_xIn_{1-x}P$ alloy, Materials Sciences and Applications 2 (07) (2011) 729. doi:10.4236/msa.2011.27101.

[25] S. Kumar, S. Joshi, S. Gupta, S. Auluck, Band gap engineering of $CuAl_{(1-x)}In_xS_2$ alloys for photovoltaic applications: a first principles study, Journal of Physics D: Applied Physics 49 (20) (2016) 205103. doi:10.1088/0022-3727/49/20/205103.

[26] W. Zhang, X. Li, T. Jiang, J. Song, Y. Lin, L. Zhu, X. Xu, CVD synthesis of $Mo_{1-x}W_xS_2$ and $MoS_{2(1-x)}Se_{2x}$ alloy monolayers aimed at tuning the bandgap of molybdenum disulfide, Nanoscale 7 (32) (2015) 13554–13560. doi:10.1039/c5nr02515j.

[27] J. Xi, T. Zhao, D. Wang, Z. Shuai, Tunable electronic properties of two-dimensional transition metal dichalcogenide alloys: a first-principles prediction, The journal of physical chemistry letters 5 (2) (2013) 285–291. doi:10.1021/jz402375s.

[28] H.-P. Komsa, A. V. Krasheninnikov, Two-dimensional transition metal dichalcogenide alloys: stability and electronic properties, The journal of physical chemistry letters 3 (23) (2012) 3652–3656. doi:10.1021/jz301673x.

[29] S. Tongay, D. S. Narang, J. Kang, W. Fan, C. Ko, A. V. Luce, K. X. Wang, J. Suh, K. Patel, V. Pathak, et al., Two-dimensional semiconductor alloys: Monolayer $Mo_{1-x}W_xSe_2$, Applied Physics Letters 104 (1) (2014) 012101. doi:10.1063/1.4834358.

[30] L. Xie, Two-dimensional transition metal dichalcogenide alloys: preparation, characterization and applications, Nanoscale 7 (44) (2015) 18392–18401. doi:10.1039/c5nr05712d.

[31] J. Kang, S. Tongay, J. Li, J. Wu, Monolayer semiconducting transition metal dichalcogenide alloys: Stability and band bowing, Journal of Applied Physics 113 (14) (2013) 143703. doi:10.1063/1.4799126.

[32] L.-Y. Gan, Q. Zhang, Y.-J. Zhao, Y. Cheng, U. Schwingenschlögl, Order-disorder phase transitions in the two-dimensional semiconducting transition metal dichalcogenide alloys $Mo_{1-x}W_xX_2$ (X= S, Se, and Te), Scientific reports 4. doi:10.1038/srep06691.

[33] X.-L. Wei, H. Zhang, G.-C. Guo, X.-B. Li, W.-M. Lau, L.-M. Liu, Modulating the atomic and electronic structures through alloying and heterostructure of single-layer MoS_2, Journal of Materials Chemistry A 2 (7) (2014) 2101–2109. doi:10.1039/c3ta13659k.

[34] H.-P. Komsa, S. Kurasch, O. Lehtinen, U. Kaiser, A. V. Krasheninnikov, From point to extended defects in two-dimensional MoS_2: evolution of atomic structure under electron irradiation, Physical Review B 88 (3) (2013) 035301. doi:10.1103/physrevb.88.035301.

[35] A. Zunger, S.-H. Wei, L. Ferreira, J. E. Bernard, Special quasirandom structures, Physical Review Letters 65 (3) (1990) 353. doi:10.1103/physrevlett.65.353.

[36] G. Kresse, J. Hafner, Ab initio molecular dynamics for liquid metals, Physical Review B 47 (1) (1993) 558. doi:10.1103/physrevb.47.558.

[37] G. Kresse, J. Furthmüller, Efficiency of ab-initio total energy calculations for metals and semiconductors using a plane-wave basis set, Computational Materials Science 6 (1) (1996) 15–50. doi:10.1016/

0927-0256(96)00008-0.

[38] P. E. Blöchl, Projector augmented-wave method, Physical Review B 50 (24) (1994) 17953. doi:10.1103/physrevb.50.17953.

[39] J. P. Perdew, K. Burke, M. Ernzerhof, Generalized gradient approximation made simple, Physical review letters 77 (18) (1996) 3865. doi:10.1103/physrevlett.77.3865.

[40] T. L. Tan, M.-F. Ng, G. Eda, Stable monolayer transition metal dichalcogenide ordered alloys with tunable electronic properties, The Journal of Physical Chemistry C 120 (5) (2016) 2501–2508. doi:10.1021/acs.jpcc.5b10739.

[41] A. D. Becke, Density-functional exchange-energy approximation with correct asymptotic behavior, Physical review A 38 (6) (1988) 3098. doi:10.1103/PhysRevA.38.3098.

[42] J. P. Perdew, Density-functional approximation for the correlation energy of the inhomogeneous electron gas, Physical Review B 33 (12) (1986) 8822. doi:10.1103/PhysRevB.33.8822.

[43] C. Lee, W. Yang, R. G. Parr, Development of the colle-salvetti correlation-energy formula into a functional of the electron density, Physical review B 37 (2) (1988) 785. doi:10.1103/PhysRevB.37.785.

[44] J. P. Perdew, A. Ruzsinszky, G. I. Csonka, O. A. Vydrov, G. E. Scuseria, L. A. Constantin, X. Zhou, K. Burke, Restoring the density-gradient expansion for exchange in solids and surfaces, Physical Review Letters 100 (13) (2008) 136406. doi:10.1103/PhysRevLett.100.136406.

[45] J. Heyd, G. E. Scuseria, M. Ernzerhof, Hybrid functionals based on a screened coulomb potential, The Journal of Chemical Physics 118 (18) (2003) 8207–8215. doi:10.1063/1.1564060.

[46] C. Jiang, C. Wolverton, J. Sofo, L.-Q. Chen, Z.-K. Liu, First-principles study of binary bcc alloys using special quasirandom structures, Physical Review B 69 (21) (2004) 214202. doi:10.1103/physrevb.69.214202.

[47] X.-L. Fan, Y. Yang, P. Xiao, W.-M. Lau, Site-specific catalytic activity in exfoliated MoS_2 single-layer polytypes for hydrogen evolution: basal plane and edges, Journal of Materials Chemistry A 2 (48) (2014) 20545–20551. doi:10.1039/c4ta05257a.

[48] D. Yang, S. J. Sandoval, W. Divigalpitiya, J. Irwin, R. Frindt, Structure of single-molecular-layer MoS_2, Physical Review B 43 (14) (1991) 12053. doi:10.1103/physrevb.43.12053.

[49] Y. Ding, Y. Wang, J. Ni, L. Shi, S. Shi, W. Tang, First principles study of structural, vibrational and electronic properties of graphene-like MX_2 (M= Mo, Nb, W, Ta; X= S, Se, Te) monolayers, Physica B: Condensed Matter 406 (11) (2011) 2254–2260. doi:10.1016/j.physb.2011.03.044.

[50] H. Guo, N. Lu, L. Wang, X. Wu, X. C. Zeng, Tuning electronic and magnetic properties of early transition-metal dichalcogenides via tensile strain, The Journal of Physical Chemistry C 118 (13) (2014) 7242–7249. doi:10.1021/jp501734s.

[51] K. F. Mak, C. Lee, J. Hone, J. Shan, T. F. Heinz, Atomically thin MoS_2: a new direct-gap semiconductor, Physical Review Letters 105 (13) (2010) 136805. doi:10.1103/physrevlett.105.136805.

[52] A. Splendiani, L. Sun, Y. Zhang, T. Li, J. Kim, C.-Y. Chim, G. Galli, F. Wang, Emerging photoluminescence in monolayer MoS_2, Nano letters 10 (4) (2010) 1271–1275. doi:10.1021/nl903868w.

[53] M. Faraji, M. Sabzali, S. Yousefzadeh, N. Sarikhani, A. Ziashahabi, M. Zirak, A. Moshfegh, Band engineering and charge separation in the $Mo_{1-x}W_xS_2/TiO_2$ heterostructure by alloying: first principle prediction, RSC Advances 5 (36) (2015) 28460–28466. doi:10.1039/c5ra00330j.

[54] H. L. Zhuang, M. D. Johannes, M. N. Blonsky, R. G. Hennig, Computational prediction and characterization of single-layer CrS_2, Applied Physics Letters 104 (2) (2014) 022116. doi:10.1063/1.4861659.

[55] K. Dolui, I. Rungger, C. D. Pemmaraju, S. Sanvito, Possible doping strategies for MoS_2 monolayers: An ab initio study, Physical Review B 88 (7) (2013) 075420. doi:10.1103/physrevb.88.075420.

[56] W. S. Yun, J. Lee, Unexpected strong magnetism of cu doped single-layerMoS_2 and its origin, Physical Chemistry Chemical Physics 16 (19) (2014) 8990–8996. doi:10.1039/c4cp00247d.

[57] D. J. Lewis, A. A. Tedstone, X. L. Zhong, E. A. Lewis, A. Rooney, N. Savjani, J. R. Brent, S. J. Haigh, M. G. Burke, C. A. Muryn, et al., Thin films of molybdenum disulfide doped with chromium by aerosol-assisted chemical vapor deposition (AACVD), Chemistry of Materials 27 (4) (2015) 1367–1374. doi:10.1021/cm504532w.

[58] Y. Chen, J. Xi, D. O. Dumcenco, Z. Liu, K. Suenaga, D. Wang, Z. Shuai, Y.-S. Huang, L. Xie, Tunable band gap photoluminescence from atomically thin transition-metal dichalcogenide alloys, Acs Nano 7 (5) (2013) 4610–4616. doi:10.1021/nn401420h.

[59] E. Clementi, D. Raimondi, W. Reinhardt, Atomic screening constants from scf functions. II. atoms with 37 to 86 electrons, The Journal of chemical physics 47 (4) (1967) 1300–1307. doi:10.1063/1.1712084.

[60] Y. Huang, X. Chen, D. Zhou, H. Liu, C. Wang, J. Du, L. Ning, S. Wang, Stabilities, electronic and optical properties of $SnSe_{2(1-x)}S_{2x}$ alloys: A first-principles study, The Journal of Physical Chemistry C 120 (10) (2016) 5839–5847. doi:10.1021/acs.jpcc.6b00794.

[61] A. R. Denton, N. W. Ashcroft, Vegards law, Physical review A 43 (6) (1991) 3161. doi:10.1103/physreva.43.3161.

[62] P. Rinke, A. Qteish, J. Neugebauer, C. Freysoldt, M. Scheffler, Combining GW calculations with exact-exchange density-functional theory: an analysis of valence-band photoemission for compound semiconductors, New Journal of Physics 7 (1) (2005) 126. doi:10.1088/1367-2630/7/1/126.

Chapter 5

Published paper: Band gap engineering of a MoS_2 monolayer through oxygen alloying: an *ab initio* study

The results reported in this chapter has been published as N. F. Andriambelaza, R. E. Mapasha, N. Chetty, Nanotechnology 29 (50) (2018) 505701.

In this work, the effects of the O line-ordered alloy configuration on the thermodynamic stability, structurale and electronic properties of the MoS_2 monolayer are investigated. The various properties of the most stable O line-ordered configurations at every concentration are compared with that of well-known random and cluster alloy configurations. The details of this study are presented in the attached publication. This publication provides a description of the computational details, a discussion of the obtained results and at the end conclusions of the entire study are given.

Band Gap Engineering of a MoS_2 Monolayer through Oxygen Alloying: an *Ab-Initio* Study

N.F. Andriambelaza[a,*], R.E. Mapasha[a], N. Chetty[a,b]

[a] *Department of Physics, University of Pretoria, Pretoria 0002, South Africa*
[b] *National Institute for Theoretical Physics, Johannesburg, 2000, South Africa*

Abstract

Oxygen (O) alloying in a MoS_2 monolayer appearing in different shapes: line-ordered, cluster and random have been theoretically designed, for band gap engineering in order to extend its nanotechnological applications. The thermodynamic stability, structural and electronic properties of these alloy configurations at each concentration have been comparatively studied using the density functional theory methods. Based on the formation energy analysis, the O line-ordered alloys are most stable compared to the well known random and cluster alloys at high concentration, while at low concentration they compete. The lattice constants of all the alloyed systems decrease linearly with the increase in O concentration, consistent with Vegard's law. The Mo-O bond lengths are shorter than the Mo-S leading to a reduction in the band gap, based on density of state analysis. The partial charge density reconciling with the partial density of states analysis reveals that the band gap reduction is mainly contributed by the Mo $4d$ and O $2p$ orbitals as shown at the band edges of the density of states plots. Creation of stacking

of MoS_2 with MoO_2 gives metallic character, with Mo $4d$ orbital crossing the Fermi level. The O alloys in a MoS_2 monolayer should be considered to be an effective way to engineer the band gap for designing new nanoelectronic devices with novel performance.
Keywords: 2D materials, density functional theory, transition metal dichalcogenides, transition metal oxides, alloying.

---

1. Introduction

Since the emergence of nanotechnology, an advancement of electronic devices has continued unabated, in particular on the speed and size (reduction from three dimension (3D) to two dimension(2D)). In the last decade, 2D hexagonal materials emerged to be promising materials for the design of nanoelectronic devices due to their unique properties. The high charge carrier mobility, mechanical flexibility and strength reduced dimensionality, transparency, etc [1, 2, 3, 4] mostly measured on graphene [5], hexagonal boron nitride (h-BN) [6], transition metal dichalcogenides (TMD) [1, 7] can be mentioned. The recently synthesized 2D hexagonal-like TMD materials such as MoS_2, $MoSe_2$, $MoTe_2$, WS_2, WSe_2, WTe_2 and CrS_2 [1, 7, 8] are particularly interesting due to their robust mechanical character and relatively large band gap [9, 10]. Recently, the hexagonal-like transition metal oxides (TMO) materials such as MoO_2, WO_2 and CrO_2 monolayers were predicted using density functional theory (DFT) and found to be semiconductors with the band gaps of 0.97 eV, 1.37 eV and 0.5 eV respectively [9, 10]. To examine the stability of these oxide based nanomaterials, Ataca *et al.* [9] performed a phonon calculation and no imaginary vibration frequencies were noted sug-

gesting mechanical stability.

Although the pristine TMD and TMO monolayers inherently possess the exotic physical properties [9, 10, 11], tuning their band gaps continuously is essential for designing nanoelectronics devices. Diverse methods such as alloying [12, 13, 14, 15], creation of point defects [16, 17, 18, 19], doping [20, 21, 22, 23, 24], application of an axial strain [25, 26, 27, 28, 29] etc. efficiently engineer the band gap of a TMD material. Alloying in a MoS_2 monolayer has been widely studied experimentally using chemical vapor deposition (CVD) methods [30, 31], and theoretically using density functional theory (DFT) methods [12, 14, 15, 32, 33]. Alloys can appear in different popular ground state configurations such as random, cluster, lines, triplets (form a triangle-like) etc. [34]. Experimental studies of the tungsten (W) alloys at the molybdenum (Mo) sites revealed that random distribution occurs spontaneously at about 1030°C [30, 31]. Photoluminescence experiments revealed that the band gap of the MoS_2 monolayer is fine tuned with the variation of the W concentration. Furthermore, DFT studies revealed that the hybridization of the d orbitals of the W atoms with those of Mo atoms at the vicinity of the band edges is mainly responsible for the increase of the band gap [35, 31]. Very recently, Andriambelaza *et al.* [14] performed a comparative study of chromium (Cr) line-ordered alloys with the random distribution alloys at the Mo sites of a MoS_2 monolayer using the DFT method. It was found that the line-ordered alloys are energetically favorable compared to the random alloys. Both distributions fine tune the band gap with the same magnitudes (1.65 eV to 0.86 eV).

For the sulfur (S) sites, the selenium (Se) and tellurium (Te) alloys are

popular studied and their experimental characterizations [36, 37] revealed the spontaneous random distribution at high temperatures. However, the DFT calculations (at zero Kelvin) indicated the ordered phase to be preferable as compared to the random distribution [8, 36]. Our previous DFT study revealed that the Te line-ordered alloys compete very well with the random alloys in terms of stability [38]. Furthermore, the band gap of the MoS_2 monolayer is fine tuned within a range that can be useful for designing novel nanotechnological devices [15, 36].

Oxygen (O) alloys in a MoS_2 monolayer have not yet been explored, although it belongs to the same group as S, Se, and Te atoms on the periodic table. Moreover, a hexagonal MoO_2 monolayer has been predicted to be isostructural to the MoS_2, $MoSe_2$ and $MoTe_2$ monolayers [9, 10]. Generally, the Se and Te atoms have more atomic radii than the S atoms, whereas the O atom possesses the smallest. Therefore, a comprehensive study on the electronic and structural properties of O alloys is necessary to compare with those of Te and Se alloys.

In this paper, various O alloy configurations in the form of random, line-ordered and cluster distributions in a 5×5 supercell of a MoS_2 monolayer are studied. However, studying all the possible alloy configurations for each distribution at every concentration is intractable and computationally time consuming using the first-principle methods. At each alloy distribution and concentration, selected configurations were optimized. Since the random and cluster distributions are the most popular studied alloys and known to exist experimentally, we compare their results with those of the line-ordered alloys.

2. Computational details

DFT method implemented within the Vienna $Ab-initio$ Simulation Package (VASP) [39] is performed to study the electronic structure of the O alloys in a MoS_2 monolayer. To describe the exchange-correlation interaction, the Perdew-Burke-Ernzerhof (PBE) parametrization within the generalized gradient approximation (GGA) [40] is used. The flavor of GGA exchange correlation functional is known to underestimate the band gap value of semiconductor materials due to the absence of the derivative discontinuity feature and delocalized errors [41]. To overcome this issue, the hybrid functionals have been proposed [42]. In this paper, the screened hybrid functional of Heyd-Scuseria-Ernzerhof (HSE06) is used by mixing 25% (AEXX = 0.25) of the exact nonlocal Hartree-Fock (HF) exchange to the PBE exchange [41, 42]. The projector augmented wave (PAW) method is employed to define the core and valence electron interactions. An energy cut-off of 300 eV is chosen for the expansion of the wave functions in the plane wave basis. A supercell of 5×5 is chosen at each concentration to model the alloys and a k-point sampling of $3 \times 3 \times 1$ is suitable for this large supercell. Atomic positions and lattice vectors are fully relaxed during the calculations with a force and energy convergence threshold of 2×10^{-2} eV/Å and 10^{-5} eV respectively. To avoid periodical interaction along the vertical axis, a vacuum space of 20 Å is considered.

The stability of the various alloy configurations at each concentration confined between to the two pristine materials is defined by the formation energy:

$$E_{form} = E_{MoS_{(1-x)}O_x} - (1-x)E_{MoS_2} - xE_{MoO_2} \ , \tag{1}$$

where $E_{MoS_{(1-x)}O_x}$ is the total energy of the system at each x O concentration. E_{MoS_2} and E_{MoO_2} are the total energies of the pristine MoS_2 and MoO_2 monolayers, respectively.

To generate the random alloy configurations, the special quasirandom structure (SQS) is adopted. The O substitutional alloy in a MoS_2 monolayer can be written in a general form $A_{1-x}B_x$, where A and B correspond to the S and O atoms, respectively. Generally, the correlation functions of an ideal alloy are given by $\prod_{k,m}(ideal) = (2x-1)^k$ [33], where k=2, 3,... indicate the pair, triple correlation, etc. and m=1, 2, 3,... correspond to the first, second and third-nearest distance, etc. Previous studies reported that the alloy nearest-neighbor interaction greatly dominates the properties of host materials, whereas the effects of far away interaction are significantly small [33, 43, 44]. Therefore, only the nearest-neighbor pairs are considered in this study.

In the other side, the pair correlation function can be written as: $\prod_{2,1}(r) = \frac{1}{N_b}\sum_{j,k=1,N}^{j>k} i_j i_k$, where $i = +1$ if the site is occupied by A atom and $i = -1$ if the site is occupied by B atom. N_b and N are the total number of bonds and chalcogen sites in the supercell, respectively. Assume that the total number of pair neighboring bonds of A-A, A-B and B-B in the supercell are denoted by N_{AA}, N_{AB} and N_{BB}, respectively. They can be expressed as [14, 33]:

$$\begin{cases} (N_{AB} + 2N_{AA})/Z = N_A = N(1-x) \\ (N_{AB} + 2N_{BB})/Z = N_B = Nx \\ N_b = N_{AA} + N_{BB} + N_{AB} \end{cases} \quad (2)$$

N_A and N_B indicate the total number of sites occupied by A and B atoms in the supercell, respectively. Z denotes the coordination number of the chalcogen atoms in the lattice. Substituting Eqn. 2 into $\prod_{2,1}(r)$ and applying some algebra we get:

$$\Pi_{2,1}(r) = \frac{N_{AA} + N_{BB} - N_{AB}}{N_{AA} + N_{BB} + N_{AB}} = 1 - 4x + \frac{8N_{BB}}{Nz}. \quad (3)$$

This equation shows clearly that the correlation functions can be expressed in terms of the number of B-B bond (N_{BB}). The random alloy configurations at each concentration are modeled in such a way that the correlation functions are identical to the ideal alloys up to the nearest-neighbor pairs ($\prod_{2,1}(ideal) = \prod_{2,1}(r)$). It results that the number of B-B bond for the random configuration should be $N_{BB} = \frac{1}{2}x^2NZ$ [14, 33]. In this study, N is the total number of chalcogen atoms present in the 5 $\times$ 5 supercell (N=50).

3. Results and discussion

3.1. Pristine MoS_2 and MoO_2 monolayers

The structure of the TMD and TMO monolayers can be classified into two types: 2H and 1T [9]. Ataca *et al.* [9] have established that MoS_2 (TMD) and MoO_2 (TMO) monolayers are more stable in 2H structure. Top and side views of a 5 $\times$ 5 supercell of the MoS_2 and MoO_2 monolayers are shown in Fig. 1(a) and Fig 1(b), respectively. The hexagonal-like pattern of the 2H structure is clearly seen on the top view of the structures, where the Mo and S (O) atoms occupy different sublattices. From the side view, it can be seen that the 2D MoS_2 and MoO_2 are made by one layer of Mo

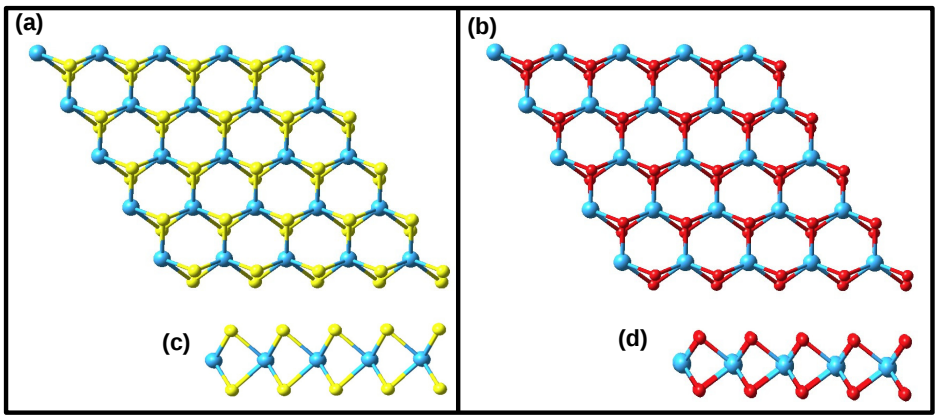

Figure 1: Top and side view of the ((a) and (c)) MoS_2 and ((b) and (d)) MoO_2 monolayers. The blue, red and yellow spheres indicate the Mo, O and S atoms respectively.

atom sandwiched in between two S (O) layers. To understand the nature of bonding between Mo atom and S (O) atom, Bader charge analysis was considered. It was found that the Mo atom has a depletion of 1.18 electron while each S atom accumulates 0.58 electron. This charge sharing reveals a covalent bond between Mo and S atoms [45]. This covalency is also confirmed by the electron localized function (ELF) analysis, where a non spherically symmetry of the regions with high ELF around S atoms and a tendency of the lobes towards the Mo are observed [46, 47].

To study the alloyed real material, the knowledge of the structural, energetics and electronic properties of the pristine host is essential. The structural and energetic properties of the MoS_2 and MoO_2 monolayers are listed in Table. 1. It was found that the HSE06 functional underestimates the lattice parameter while GGA functional overestimates it [52]. These results are in good agreement with the previous experimental and theoretical data as

Table 1: Lattice constant a(Å), bond length d[Mo-X (X = S, O)](Å), cohesive energy E_{coh} (eV/atom), formation energy E_{form} (eV), band gap values E_{gap} (eV) of the pristine MoS_2 and MoO_2 monolayers.

System	Method		a	d[Mo-X]	E_{coh}	E_{form}	E_{gap}
MoS_2	Previous work	Expt.	3.16[a,b]	2.41[i]	-	-	1.90[n]
		GGA	3.18[c], 3.20[g]	2.41[d], 2.408[h]	5.18[g]	-0.842[c]	1.652[e], 1.70[d]
		HSE06	3.153[h], 3.155[f]	2.391[h], 2.39[d]	-	-	2.10[d], 2.23[o]
	This work	GGA	3.18	2.41	6.54	-1.40	1.67
		HSE06	3.153	2.38	5.69	-1.47	2.17
MoO_2	Previous work	Expt.	-	-	-	-	-
		GGA	2.82[c], 2.83[l,j]	2.05[j,l]	7.55[k]	-1.73[c]	0.98[m], 0.97[d]
		HSE	-	-	-	-	1.48[l]
	This work	GGA	2.81	2.05	6.14	-2.25	0.97
		HSE06	2.79	2.02	5.77	-3.02	1.48

[a]ref. [48], [b]ref. [49], [c]ref. [10], [d]ref. [47], [e]ref. [50], [f]ref. [21], [g] ref. [51], [h]ref. [52], [i]ref. [53], [j]ref. [11], [k]ref. [9], [l]ref. [54], [m]ref. [55], [n]ref. [7], [o]ref. [56]

seen in Table. 1. The total density of states (TDOS) and partial density of states (PDOS) of the MoS_2 and MoO_2 monolayers are evaluated and plotted in Figs. 2(a-b). We found that these two pristine systems are band gap semiconductors. Quantitatively, the band gap values of 1.67 eV (2.17 eV) and 0.98 eV (1.48 eV) are measured using GGA (HSE) functional for the MoS_2 and MoO_2 monolayers, respectively. These values are in good agreement with previously reported data as presented in Table. 1. The PDOS

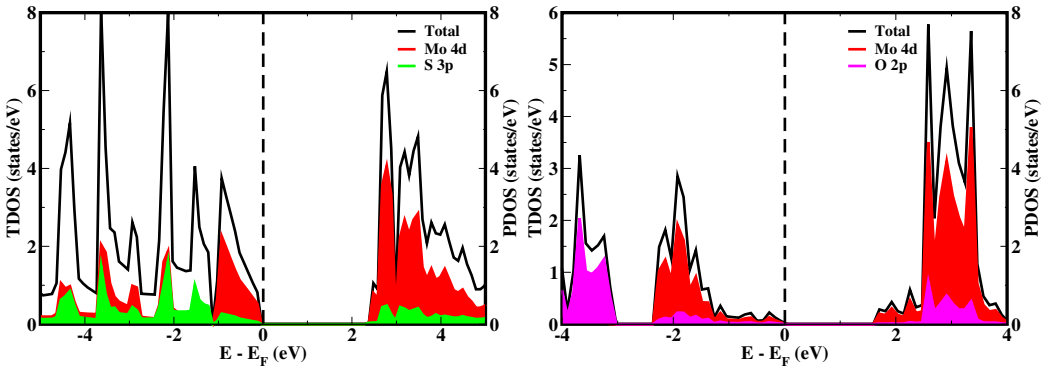

Figure 2: Total density of states (TDOS) and partial density of states (PDOS) of the (a) MoS_2 and (b) MoO_2 monolayers obtained using HSE06 functional. Black solid lines indicate the TDOS of the MoS_2 and MoO_2 monolayers. The red, green and magenta lines correspond to the d orbital of the Mo atom, the p orbitals of the S and O atoms, respectively. The dashed vertical lines represent the Fermi level.

plots clearly indicate that the conduction band minimum (CBM) states of both the MoS_2 and MoO_2 monolayers arise mainly from the Mo 4d orbitals. On the other hand, the valence band maximum (VBM) states of both systems are contributed by the hybridization of the Mo 4d orbitals and the S 3p (O 2p) orbitals. These orbital contributions are consistent with the results reported in Refs [11, 21].

3.2. Identification of the various O alloy configurations

Generally, the properties of an alloy material greatly depend on the structural arrangement and composition variation. In this section, various alloy configurations at different O concentrations are discussed. The identification of the O line-ordered alloy, typical O cluster, and various O random alloy configurations at each concentration is described. In fact, the vital question associated with this section is how to generate these various configurations

of O alloys?

To explain the O line-ordered alloy configurations studied in this work, Fig. 3 shows a schematic representation of labeled 5 × 5 supercell of a MoS_2 monolayer. For the formation of the O line-ordered alloys, S atoms are substituted with O atoms along the zigzag direction of the supercell. The labels u, b, r_1, r_2, r_3, r_4 and r_5 in the Fig. 3 are used to name the distinct configurations of O line-ordered alloys in a MoS_2 monolayer, obeying the periodic boundary conditions (PBC) to avoid the double counting. The letter u and b refer to the upper and the bottom layers of S atom respectively, sandwiching the Mo layer. The labels r_1, r_2, r_3, r_4 and r_5 indicate the first, second, third, fourth and fifth row of the S atoms in the 5 × 5 supercell, as clearly seen in Fig. 3. There are seven S concentrations (%) studied in this work: 0.0 (0%), 0.1 (10%), 0.3 (30%), 0.5 (50%), 0.7 (70%), 0.9 (90%) and 1.0 (100%). Several unique O line-ordered configurations at each concentration are identified and studied. Table. 2 lists all the identified O line-ordered alloy configurations. The 0.1 concentration of O atoms in a 5 × 5 supercell of a MoS_2 monolayer typically means five O atoms substitute five S atoms. For the continuous line-ordered alloy, one unique configuration is identifiable at this concentration, i.e the O atoms replacing the upper (u) S atoms in row 1 (r_1) can be denoted as O@r_{1u}. Obeying PBC, this configuration is the same as O$_@r_{2u}$, O$_@r_{3u}$, O$_@r_{1b}$, O$_@r_{2b}$, etc. Therefore, this configuration is uniquely called the line-ordered alloy configuration 1 at 0.1 concentration ($C_{1L(0.1)}$).

At 0.3 concentration, fifteen O atoms replace the S atoms in the system. Eight unique O line-ordered configurations (configuration $C_{1L(0.3)}$ to $C_{8L(0.3)}$) are also identified from Fig. 3 and enumerated in Table. 2. Their representa-

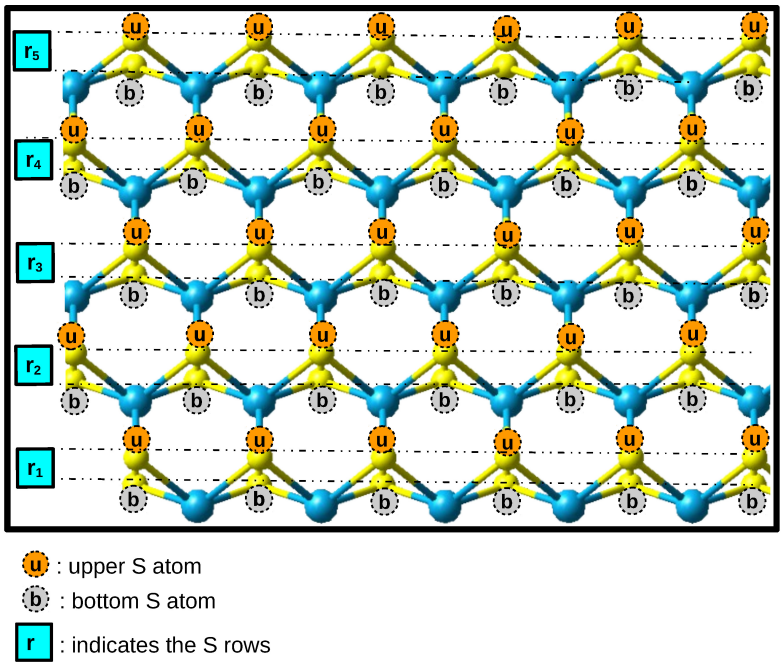

Figure 3: A schematic representation of a MoS_2 monolayer used to identify the line ordered alloys at every concentration. The diagram shows the three different layers of atoms. The blue and yellow spheres represent the Mo and S atoms, respectively. The labels u and b depict the upper and bottom S atoms. The label r indicates the rows.

tions are formulated the same way as that of 0.1 concentration. For instance, $C_{1L(0.3)}$ is the first line-ordered alloy configuration at 0.3 concentration. It is constituted by line of O atoms occupying row 1 (r_1) on the upper (u) layer and two rows r_1 and r_3 on the bottom (b) layer. It is denoted as $O_{@}r_{1ub}r_{3b}$ as seen in Table. 2. The same description is applicable to all the possible O line-ordered alloys at this concentration (see Table. 2). At 0.5 concentration, the number of the S and O atoms are the same (25 S atoms and 25 O atoms). Following the same pattern as in 0.1 and 0.3 concentrations, the permutation of the O rows gives sixteen unique line-ordered alloy configurations named as configuration $C_{1L(0.5)}$ to $C_{16L(0.5)}$. At 0.5 concentration, there is a special configuration where the O atoms fully cover the top layer and the S atoms

Table 2: All the possible line-ordered alloy configurations identified in a 5 × 5 supercell of MoS_2 monolayer at different concentrations. The thermodynamic stability of these various configurations will be checked. The labels u and b correspond to the upper and bottom S atoms. The letter r indicates the number of rows and the letter C stands for configuration.

	Concentration				
Conf.	0.1	0.3	0.5	0.7	0.9
C_{1L}	$O@r_{1u}$	$O@r_{1ub}r_{3b}$	$O@r_{1ub}r_{2u}r_{3u}r_{4u}$	$O@r_{2ub}r_{3u}r_{4ub}r_{5ub}$	$O@r_{1u}r_{2ub}r_{3ub}r_{4ub}r_{5ub}$
C_{2L}	-	$O@r_{1ub}r_{2u}$	$O@r_{1ub}r_{2ub}r_{3u}$	$O@r_{1u}r_{2u}r_{3u}r_{4ub}r_{5ub}$	-
C_{3L}	-	$O@r_{1u}r_{2u}r_{3u}$	$O@r_{1ub}r_{2u}r_{3ub}$	$O@r_{1b}r_{2u}r_{3u}r_{4ub}r_{5ub}$	-
C_{4L}	-	$O@r_{1u}r_{2u}r_{3b}$	$O@r_{1u}r_{2u}r_{3u}r_{4u}r_{5u}$	$O@r_{2u}r_{3ub}r_{4ub}r_{5ub}$	-
C_{5L}	-	$O@r_{1u}r_{2u}r_{4u}$	$O@r_{1u}r_{2u}r_{3u}r_{4u}r_{5b}$	$O@r_{1ub}r_{2u}r_{3u}r_{4ub}r_{5u}$	-
C_{6L}	-	$O@r_{1u}r_{2u}r_{4b}$	$O@r_{1u}r_{2u}r_{3u}r_{4b}r_{5b}$	$O@r_{1b}r_{2b}r_{3ub}r_{4u}r_{5ub}$	-
C_{7L}	-	$O@r_{1u}r_{2b}r_{3u}$	$O@r_{1b}r_{2u}r_{3b}r_{4u}r_{5b}$	$O@r_{1b}r_{2u}r_{3b}r_{4ub}r_{5ub}$	-
C_{8L}	-	$O@r_{1u}r_{2b}r_{4u}$	$O@r_{1ub}r_{2ub}r_{4u}$	$O@r_{1ub}r_{2b}r_{3ub}r_{4u}r_{5b}$	-
C_{9L}	-	-	$O@r_{1ub}r_{2u}r_{3u}r_{4b}$	-	-
C_{10L}	-	-	$O@r_{1ub}r_{2u}r_{3u}r_{5u}$	-	-
C_{11L}	-	-	$O@r_{1ub}r_{2u}r_{3u}r_{5b}$	-	-
C_{12L}	-	-	$O@r_{1ub}r_{2b}r_{3u}r_{5b}$	-	-
C_{13L}	-	-	$O@r_{1ub}r_{2u}r_{3b}r_{5b}$	-	-
C_{14L}	-	-	$O@r_{1ub}r_{2b}r_{3u}r_{4u}$	-	-
C_{15L}	-	-	$O@r_{1ub}r_{2u}r_{3b}r_{4u}$	-	-
C_{16L}	-	-	$O@r_{1ub}r_{2b}r_{4ub}$	-	-

fully cover the bottom layer. This configuration is known as *Janus* TMD structure [57]. It has been synthesized for the study of Se atoms in a MoS_2 monolayer. To generate the various O line-ordered alloy configurations at 0.7 concentration, we take all the configurations identified at 0.3 concentration

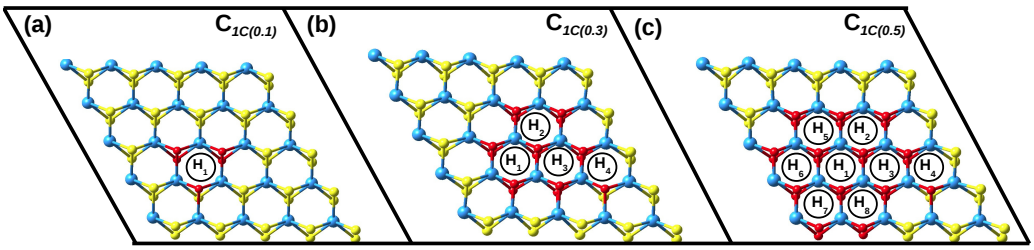

Figure 4: The geometric structures of the O atoms clustered in a MoS_2 monolayer viewed from the top at 10%, 30% and 50% concentrations. The blue, red and yellow spheres indicate the Mo, O and S atoms respectively.

and exchange the O with S atoms. Ditto to 0.9 concentrations.

The O cluster alloy configurations are also considered in this study. Basically, an O cluster configuration is constructed in such a way that all the O atoms are grouped together. Figs. 4(a-c) show typical cluster configurations at 0.1, 0.3 and 0.5 concentrations, respectively. At 0.1 concentration, the five O atoms occupy one hexagonal ring-like, denoted as H_1 indicated in Fig. 4(a). Three of the O atoms occupy all the three S sites of the upper layer (u) and form a triangle-like configuration, whereas the remaining two occupy the bottom layer (b). This cluster configuration is called $C_{1C(0.1)}$ in this work. At 0.3 concentration, the fifteen O atoms are grouped in the middle of the 5×5 supercell of a MoS_2 monolayer replacing the S atoms obeying the PBC. In this configuration, the fourteen O atoms occupy the hexagons H_1, H_2 and H_3 with one extra O atom overlapping to H_4 as shown in Fig. 4(b), and this configuration is denoted as $C_{1C(0.3)}$. The last cluster configuration presented in Fig. 4(c) corresponds to the 0.5 concentration. The O atoms are grouped together covering seven hexagons H_1, H_2, H_3, H_5, H_6, H_7 and

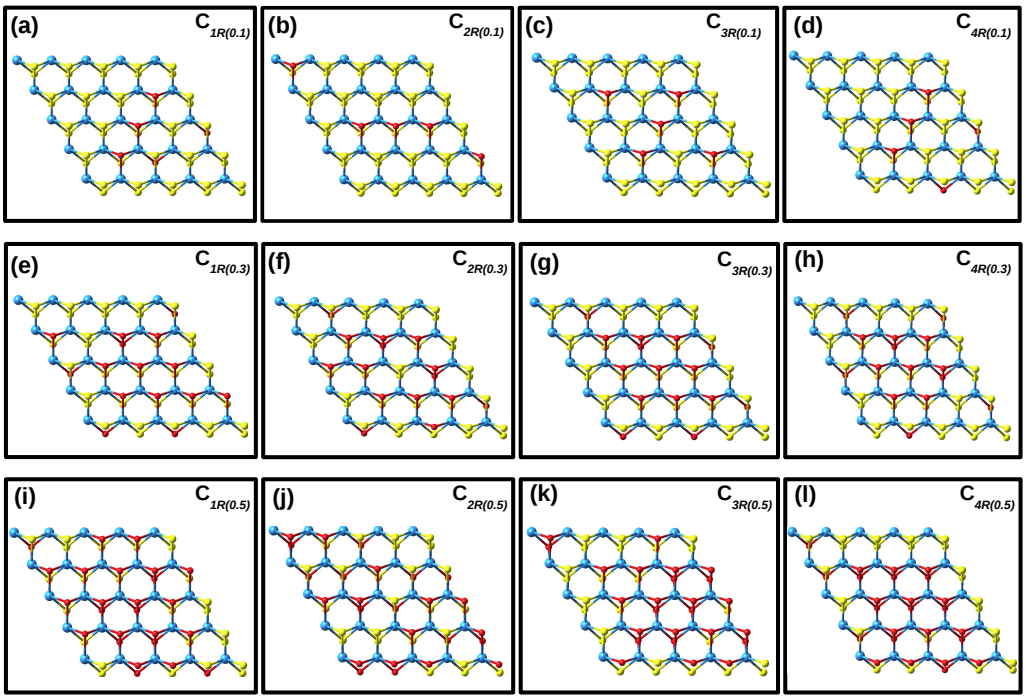

Figure 5: The selected geometric structures of the various O random alloy configurations in a MoS_2 monolayer viewed from the top at 10% (a-d), 30% (e-h) and 50% (i-l) concentrations. The blue, red and yellow spheres indicate the Mo, O and S atoms respectively.

H_8 in Fig. 4(c). One O atom is overlapping in H_4 as noted in Fig. 4(c). This cluster configuration at 0.5 concentration is called configuration $C_{1C(0.5)}$.

The last O alloy shape that we are considering in this paper is the most popular random distribution alloy. The challenge in the random alloy is the possibility of multiple configurations at each concentration. In this study, the special quasi-random structure (SQS) method proposed by Zunger et al. [58] is used to generate the various O random alloy configurations. The

SQS algorithm described in the Refs. [14, 33] which mimics an infinite perfect random alloy based on the behavior of the first nearest-neighbor atoms has been considered in this study. Obeying this method, the number of required alloy nearest-neighbor bonds are 2, 16 and 44 for 0.1, 0.3 and 0.5 concentrations respectively in a 5×5 supercell. At each concentration, many possible configurations can be formed. Considering a high computational cost, only selected alloy configurations that are spontaneously occur experimentally are shown in Fig. 5 are optimized. These special configurations are denoted as configuration $C_{1R(0.1)}$, $C_{2R(0.1)}$, $C_{3R(0.1)}$ and $C_{4R(0.1)}$ for 0.1 concentration, configuration $C_{1R(0.3)}$, $C_{2R(0.3)}$, $C_{3R(0.3)}$ and $C_{4R(0.3)}$ for 0.3 concentration, and configuration $C_{1R(0.5)}$, $C_{2R(0.5)}$, $C_{3R(0.5)}$ and $C_{4R(0.5)}$ for 0.5 concentration as presented in Fig. 5.

In the next section, the comparative studies of random, cluster and line-ordered alloy configurations at different concentrations are considered.

3.3. Thermodynamic stabilities of the MoS_2 monolayer alloyed with O atoms

As a common practice, in $ab - initio$ studies the relative thermodynamic stability of any alloy configuration is usually evaluated using the formation energy analysis defined in Eqn. 1.

In this study, the calculated formation energy values of all alloy configurations considered are summarized in Table. 3. The bold energy values represent the most energetically stable configuration for each type of alloy at every concentration. As seen in Table. 3, the formation energy values are positive, but with the small magnitude of the order 10^{-2} eV. The DFT calculations performed at static conditions may contribute to these positive

Table 3: Formation energy in meV values of various unique O line-ordered, random and cluster alloy configurations at 0.1, 0.3, 0.5, 0.7 and 0.9 concentrations. The letter C stands for configuration and the subscripts L, R and C indicate the line-ordered, random and cluster alloy configurations respectively. The bold values indicate the most energetically stable configuration for each type of alloy at every concentration.

		Concentration				
Type	Conf.	0.1	0.3	0.5	0.7	0.9
Line	C_{1L}	**31.12**	57.13	62.57	46.74	**15.89**
	C_{2L}	-	55.81	60.84	57.82	-
	C_{3L}	-	73.59	58.87	42.75	-
	C_{4L}	-	56.54	101.68	47.11	-
	C_{5L}	-	76.88	76.64	59.71	-
	C_{6L}	-	**52.87**	**53.90**	**39.32**	-
	C_{7L}	-	62.73	65.40	48.60	-
	C_{8L}	-	59.82	59.98	44.76	-
	C_{9L}	-	-	57.54	-	-
	C_{10L}	-	-	76.95	-	-
	C_{11L}	-	-	55.28	-	-
	C_{12L}	-	-	60.89	-	-
	C_{13L}	-	-	61.82	-	-
	C_{14L}	-	-	58.11	-	-
	C_{15L}	-	-	64.28	-	-
	C_{16L}	-	-	57.92	-	-
Random	C_{1R}	29.96	59.62	68.20	46.20	15.02
	C_{2R}	30.23	59.08	60.98	43.01	17.06
	C_{3R}	30.06	58.48	64.55	41.81	16.40
	C_{4R}	**29.59**	**56.77**	**59.98**	**39.28**	**14.74**
Cluster	C_{1C}	**27.91**	**54.61**	**58.78**	**42.46**	**15.80**

formation energy values. Therefore, the small positive values should not hinder the possibility of synthesizing a MoS_2 monolayer alloyed with O atoms.

The top part of Table. 3 summarizes the formation energy of the various O line-ordered alloy configurations defined in Table 2. Amongst of them, the configurations $C_{1L(0.1)}$, $C_{6L(0.3)}$, $C_{6L(0.5)}$, $C_{6L(0.7)}$ and $C_{1L(0.9)}$ are found to be energetically stable at 0.1, 0.3, 0.5, 0.7 and 0.9 concentrations respectively. The corresponding atomic structures of the configurations $C_{1L(0.1)}$, $C_{6L(0.3)}$ and $C_{6L(0.5)}$ are depicted in Figs. 6(a-c). Those of configurations $C_{6L(0.7)}$ and $C_{1L(0.9)}$ are simply the inverses of the configurations $C_{6L(0.3)}$ and $C_{1L(0.1)}$ respectively, i.e formed by exchanging the S and O atoms in the supercell system. We observe in Table. 3 and Fig. 7 that the configuration $C_{1L(0.1)}$ is more stable followed by $C_{1L(0.9)}$, $C_{6L(0.3)}$, $C_{6L(0.7)}$ and $C_{6L(0.5)}$, indicating that the formation energies of O alloys are concentration dependent as shown by the parabolic curve. This trend is in agreement with the previous studies of well known random and cluster alloys [33, 35].

Just like in some ideal alloys [14, 13, 32, 33], our 50/50 concentration alloy is the most energetically unfavorable. However, this observation contradicts that of Te alloy in a MoS_2 monolayer where 0.7 concentration is the least in stability [12, 15, 38]. At this concentration, the most stable configuration is configuration $C_{6L(0.5)}$ and can be defined as $O_{@}r_{1u}r_{2u}r_{3u}r_{4b}r_{5b}$, while the most unstable one is configuration $C_{10L(0.5)}$ given by $O_{@}r_{1u}r_{2u}r_{3u}r_{4u}r_{5u}$. This latter clearly shows that all five O rows are found in the upper layer and S atoms on the bottom layer or vice versa considering the translation symmetry operation. In addition, the O atoms fully cover the upper layer of S atoms. This typical structural arrangement has been discovered in the case of a

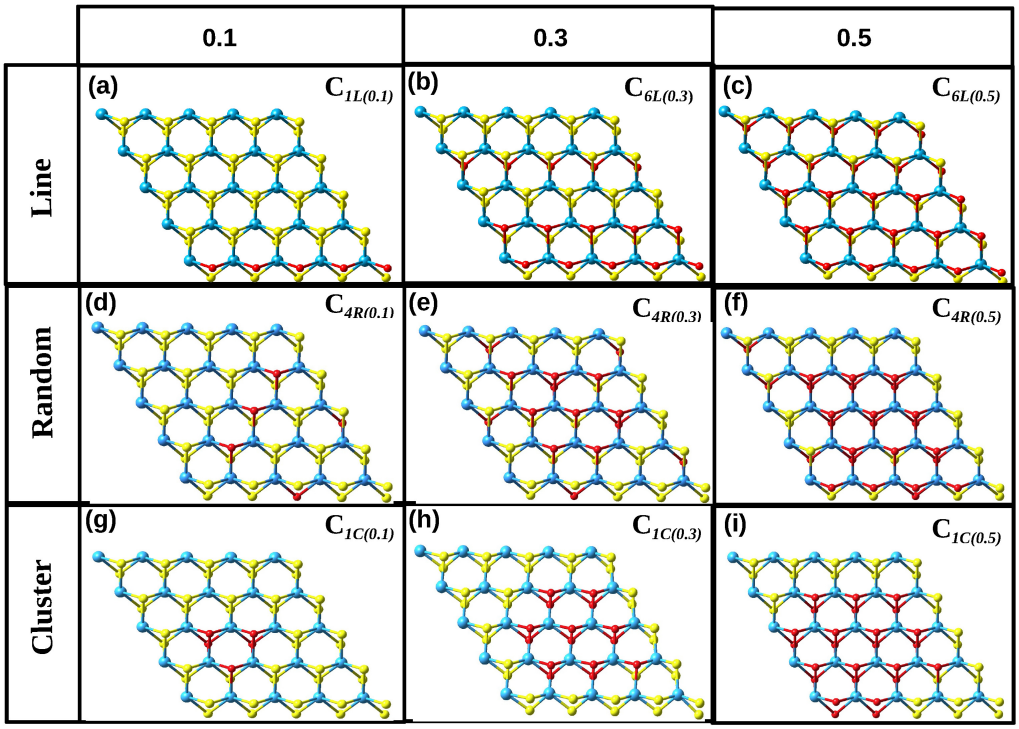

Figure 6: The optimized structures of the most energetically stable configuration at 0.1, 0.3 and 0.5 concentrations for line-ordered (a-c), random (d-f) and cluster (g-i) alloys. The blue, red and yellow spheres indicate the Mo, O and S atoms respectively.

MoS_2 monolayer alloyed with Se and Te atoms [12, 38, 59]. Also, it has been experimentally synthesized at high temperatures [57]. A common aspect with 0.5 concentration has been found at 0.3 concentration. The most stable configuration at 0.3 concentration is $C_{6L(0.3)}$ given by $O_{@}r_{1u}r_{2u}r_{4b}$ and the most unstable one is $C_{4L(0.3)}$ given by $O_{@}r_{1u}r_{2u}r_{3u}$. We observe that for each layer the lines of O atom prefer to be adjacent to each other but for

the different layer, they do not prefer to be superjacent to each other (see Fig.6(b) and Fig.6(c)). These observations and the diversity of the formation energy values summarized in Table. 3 reveal that the formation energy of the O alloy in a MoS_2 monolayer is governed by the concentration as well as the atomic arrangement.

The middle part of Table. 3 shows the formation energy of the selected random alloy configurations defined in the previous section. Amongst of them, the configurations $C_{4R(0.1)}$, $C_{4R(0.3)}$, $C_{4R(0.5)}$, $C_{4R(0.7)}$ and $C_{4R(0.9)}$ have the lowest formation energies at $0.1, 0.3, 0.5, 0.7$, and 0.9 concentration respectively. From Fig. 5 and Table. 3, we realize that the stability of the O random alloys depends on the distribution of the O atoms in the upper and bottom layer of the supercell. For the configuration to be most energetically favorable, the number of O atom in the upper and bottom layers must be close. For instance, at 0.3 concentration, configurations $C_{1R(0.3)}$, $C_{2R(0.3)}$, $C_{3R(0.3)}$ and $C_{4R(0.3)}$ have 10, 10, 9 and 8 O atoms in the upper layer and 5, 5, 6 and 7 O atoms in the bottom layer, respectively. According to Table. 3, configuration $C_{4R(0.3)}$ is most stable. That is, the larger the difference between the number of O atom in the upper and bottom layers, the more the random alloy system unstable. The similar trend is noted in other concentrations. However, the difference in formation energy values is relatively very small between the various configurations of the same concentration (less than 0.02 eV). This suggests that these configurations might co-exist at finite temperature.

Fig. 7 compares the formation energies of the lowest energy configurations at each concentration for the different alloy shapes. This gives an insight for

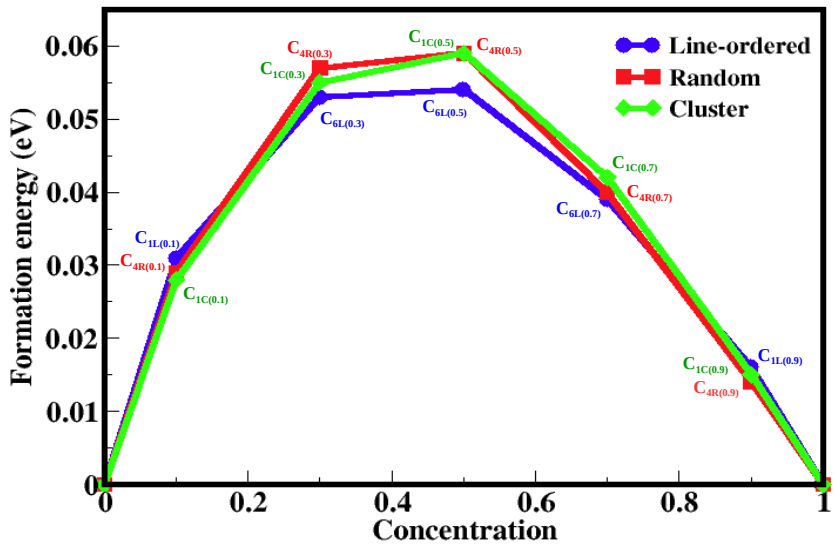

Figure 7: Variation of the formation energies with respect to the O concentration for the lowest energy configuration of the O line-ordered (blue), random (red), and cluster (green) alloys.

the possibility of synthesizing the newly predicted 2D material formed by a MoS_2 monolayer alloyed with O atoms. This plot of the formation energies shows that these different types of alloy follow the same trend. Although at 50/50 concentration, the hypothetical line-ordered is more energetically favorable. In addition, we found that the lowest energy configurations of the line-ordered competes with those that are already experimentally achieved (random and cluster) using other atoms, suggesting that all of them can be synthesized under the same conditions.

3.4. Structural properties of the O alloys in a MoS_2 monolayer

We now examine the effects of the O alloys on the lattice constants of a MoS_2 monolayer. We evaluate the lattice constants of the lowest energy configurations of the line-ordered, random and cluster obtained at each concentration shown in Fig. 8. We observe the three plots of the lattice constant to have the same trend, showing monotonously decrease due to the small atomic radii of the O atom compared to that of S atom. This trend is opposite to the previous result on MoS_2 monolayer alloyed with Te and Se atoms [15, 38] since they have large atomic radii compared to a S atom. For the three cases, the calculated values of the lattice constants of all configurations at every concentration ranges between those of the pristine MoS_2 (3.18 Å) and MoO_2 (2.81 Å) monolayers. Comparing the obtained values at each concentration for each shape of alloy, the magnitudes of the lattice constant are almost equal. This suggests that the area of the system does not really depend on the atomic arrangement but on the alloy concentration. We also in Fig. 8 plotted the lattice constants of these configurations obtained from the linear interpolations known as Vegard's law [60]. The reliability of this law has frequently been reported in the 3D [61, 62] and 2D TMD monolayer alloys [13, 14]. As seen in Fig. 8, we observe that the lattice constants of each type of alloy considered vary almost linearly, revealing that Vegard's law is being obeyed [63]. Usually, the fulfillment of this law indicates the existence of small lattice mismatch between the two pristine systems [60], in our case MoS_2 and MoO_2 monolayers.

To further analyze the intra-change in the structural properties at each concentration, the distribution of the first nearest bond lengths is measured.

We also compare the bond length deviation for each type of alloy considered in this study as shown in Fig. 9. We only present the bond lengths for the three different alloy shapes measured at 0.1 concentration, since the same observation is seen at higher concentrations. The measured Mo-S bond lengths for each alloy system are found to be constantly equal to that of a pristine MoS_2 monolayer, whereas a deviation from the pristine bond length value is noted for the Mo-O bonds. This deviation varies between 2.05 Å to 2.09 Å depending on the shape of alloy with a percentage difference of 1.93% (2.09 Å) for the line, 0.97-1.45% (2.07 Å, 2.08 Å) for the random and 0-0.49%

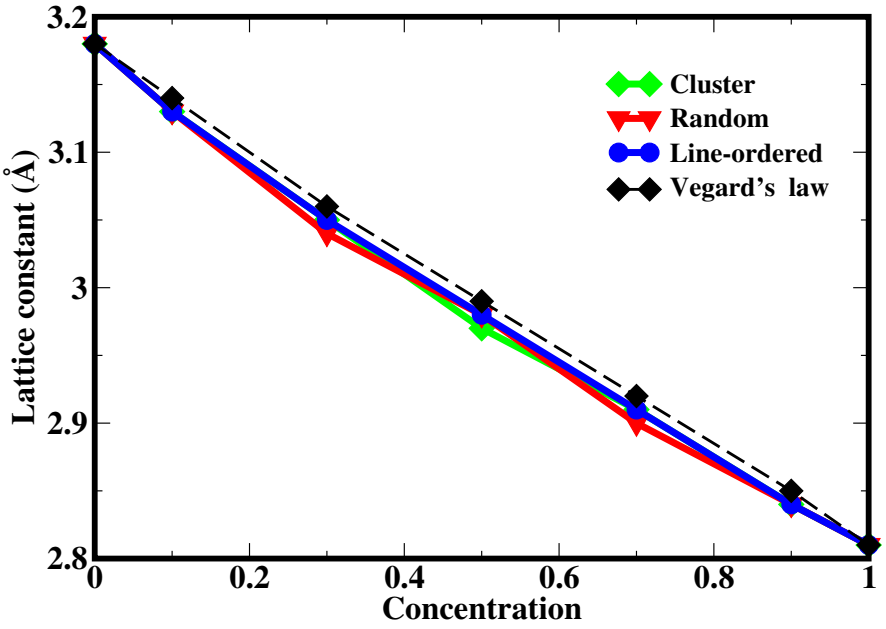

Figure 8: The variation in lattice constants for the lowest energy configuration at 0.1, 0.3, 0.5, 0.7 and 0.9 concentration, relative to the change in concentration. Blue, red and black solid lines connect the lattice constant at each concentration for the O line-ordered, random and cluster alloys respectively.

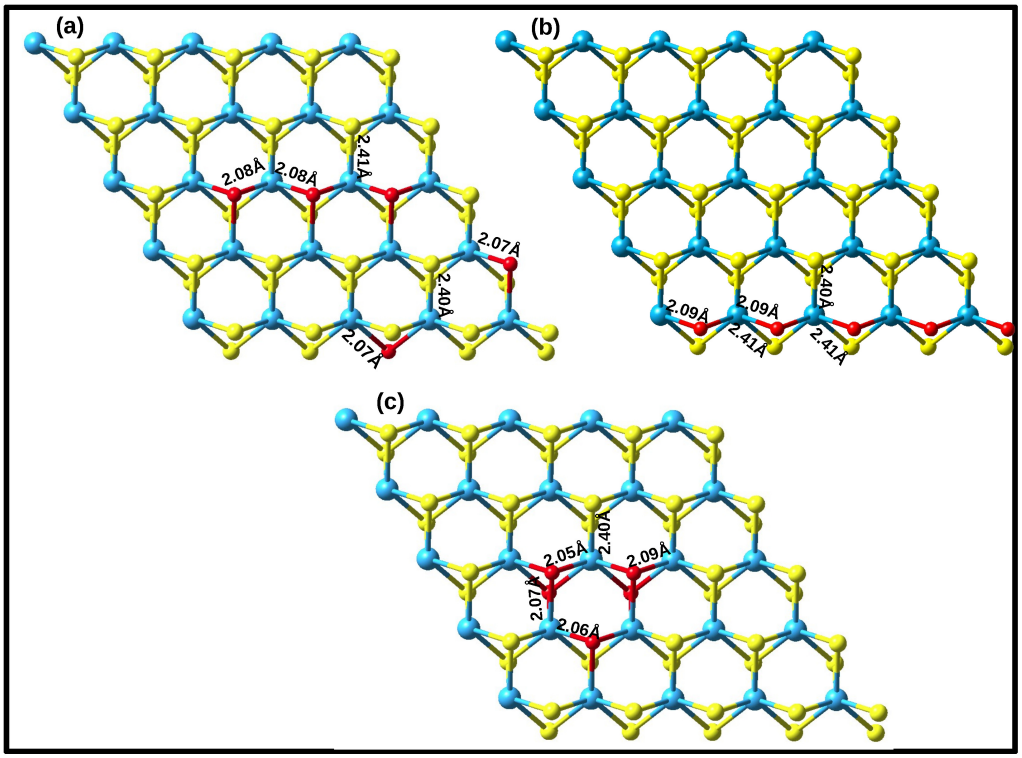

Figure 9: Top view of a hexagonal MoS_2 monolayer alloyed with 0.1 concentration of O atoms, showing the bond lengths (Mo-S) and (Mo-O) located at the various sites. The blue, red and yellow spheres indicate the Mo, O and S atoms respectively.

(2.05 Å, 2.06 Å) for the cluster. This small disparity in Mo-O bond length might be the cause of the slight differences in lattice constants for the three types of alloy studied. Since the bond length fluctuation of the various systems is not significant, the hexagonal symmetry from the top view of the host material is preserved after alloying.

Table 4: Calculated band gap values of the most stable configurations at every concentration for the O line-ordered, random and cluster configurations.

	Band gap(eV)					
	GGA			**HSE06**		
Concentration	Line	Random	Cluster	Line	Random	Cluster
0.1	1.50	1.50	1.60	2.00	2.12	2.15
0.3	1.39	1.43	1.53	1.97	2.00	2.10
0.5	1.18	1.37	1.45	1.82	1.90	2.02
0.7	1.12	1.19	1.29	1.63	1.75	1.93
0.9	1.02	1.12	1.03	1.58	1.60	1.66

The obtained band gap values are consistent with the values reported in ref. [64].

3.5. Electronic properties of the MoS_2 systems alloyed with O atoms

To examine the influence of the O atom alloys on the electronic properties of the MoS_2 monolayer, the total and partial density of states (TDOS and PDOS) at each concentration are plotted and shown in Fig.10. As seen in this figure, the alloyed systems retain the semiconducting features of the MoS_2 monolayer, although the band gap value decreases with the increase in O concentration. This suggests that the insertion of the O atoms in the MoS_2 monolayer can fine tunes the band gap of this system. To quantify this reduction, the band gaps of the most energetically stable configurations at each concentration for the O line-ordered, random and cluster alloys are measured and presented in Table 4. A common aspect of the electronic properties of the three shapes of alloys considered in this study is that the

band gap magnitudes of the various systems vary between the band gaps of the MoS_2 (1.65 eV for GGA and 2.17 eV for HSE06) and MoO_2 (0.98 eV for GGA and 1.48 eV for HSE06) monolayers. This range of the obtained band gap values is required for various applications such as solar cell, electronic applications, etc. Alternatively, the band gaps of the O random and cluster alloy configurations seem to be constantly higher than that of O line-ordered alloy. These observations suggest that the structural shape also have an influence on the band gap engineering in a MoS_2 monolayer alloyed with O atoms.

The PDOS shown in Fig.10 illustrates the origin of the reduction of the band gap. In this figure, we only present the PDOS of the O line-ordered alloys since the contribution of the orbitals at the band edges are the same for the three types of alloys. We found that the valence band maximum (VBM) is contributed by the d orbital of the Mo atoms and the p orbitals of the S and O atoms, while the conduction band minimum (CBM) is mainly dominated by the d orbitals of the Mo atoms. Therefore, the p orbital states from the O atoms introduced lie in the band edge and affect the hybridization of the Mo d orbital and S p orbital of the pristine MoS_2 monolayer, resulting in the band gap narrowing.

To have a deep understanding of the electronic interaction between the host material MoS_2 monolayer and the O atoms introduced, we also study the charge distribution at each site for each concentration as shown in Fig. 11. It can be seen that the VBM states of the O line-ordered alloy in a MoS_2 monolayer are localized around the Mo, S and O atoms, while the CBM states are concentrated around the Mo atoms only. These results are consistent with

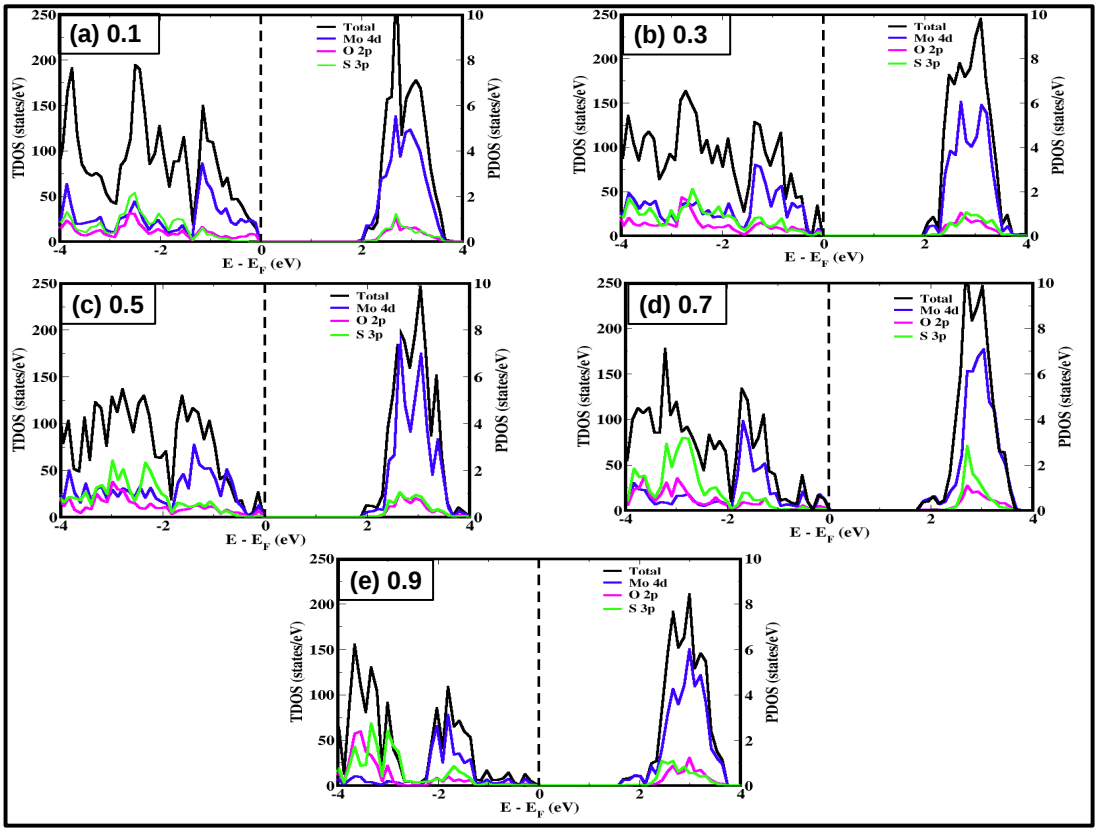

Figure 10: TDOS and PDOS of the lowest energy configuration at 0.1, 0.3, 0.5, 0.7 and 0.9 concentrations for the line-ordered alloy configurations obtained using HSE06 functional. The blue, magenta and green solid lines correspond to the Mo 4*d*, O 2*p* and S 3*p* orbitals respectively. The black solid line indicates the TDOS and the dashed vertical line represents the Fermi level

the PDOS observations described earlier (see Fig. 10). Furthermore, we also observe that the Mo atoms bonded with the O atoms along the O row have more charge compared to others.

Besides the transition from pristine MoS_2 to MoO_2 monolayers through alloying, stacking of these two different TMD monolayers is also expected

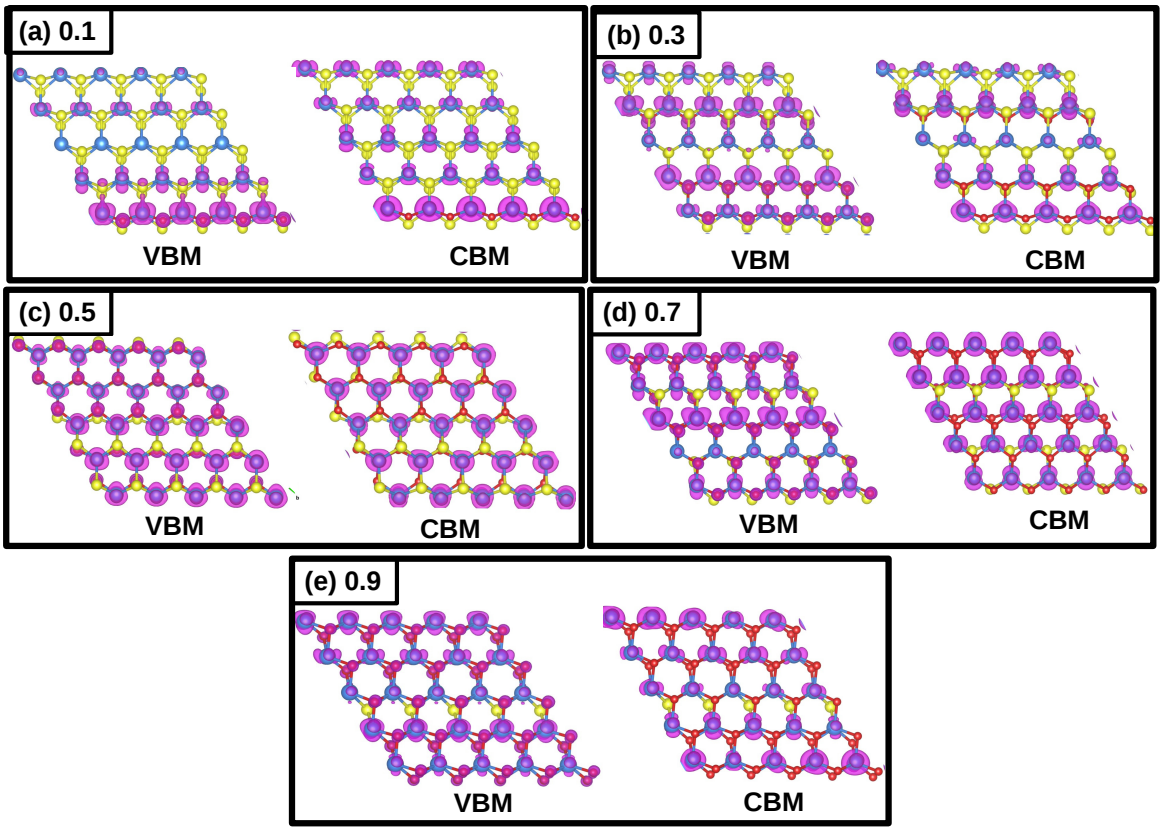

Figure 11: Partial charge density of the lowest energy configuration at each concentration. The blue, red and yellow spheres indicate the Mo, O and S atoms respectively.

to affect the electronic properties of these materials. In this study, the homobilayers (MoS_2/MoS_2 and MoO_2/MoO_2) and heterobilayer (MoO_2/MoS_2) are investigated for band gap engineering. The well known high-symmetry stacking orders such as AA, AA1 and AB are considered. (i) AA stacking is an eclipsed stacking with Mo atom facing Mo atom and S (or O) aligned with S (or O) atom of the subsequent layer. (ii) AA1 stacking is an eclipsed

stacking where Mo atom is on top of the S (or O) atom. (iii) Stacking type AB is a staggered stacking with S(or O) atom over Mo atom and Mo atom facing the center of the hexagon of the subsequent layer.

Table 5: The calculated formation energies $E_{form}(eV)$ and band gaps $E_{gap}(eV)$ of AA, AA1 and AB for homobilayers (MoS_2/MoS_2 and MoO_2/MoO_2) and heterobilayer (MoO_2/MoS_2).

Systems	properties	AA	AA1	AB
MoS_2/MoS_2	E_{form}	-0.31	-0.36	-0.34
	$E_{gap(GGA)}$	1.50	1.30	1.29
	$E_{gap(HSE)}$	2.10	1.95	1.90
MoO_2/MoO_2	E_{form}	1.09	1.08	1.15
	$E_{gap(GGA)}$	0.91	0.81	0.76
	$E_{gap(HSE)}$	1.47	1.45	1.30
MoO_2/MoS_2	E_{form}	0.40	0.37	1.3
	$E_{gap(GGA)}$	-	-	-
	$E_{gap(HSE)}$	-	-	-

The thermodynamic stability of these configurations is evaluated by calculating the formation energy using the following formula [65, 66]:

$$E_{form} = E_{stacking} - n_{MoS_2}E_{MoS_2} - n_{MoO_2}E_{MoO_2} \tag{4}$$

where $E_{stacking}$, E_{MoS_2} and E_{MoO_2} are the total energies of the stacked system, single layer of MoS_2 and MoO_2, respectively. n_{MoS_2} and n_{MoO_2} are the number of single layers of MoS_2 and MoO_2 present in the system. The energetics as well as the band gaps of the various configurations are summarized in Table. 5.

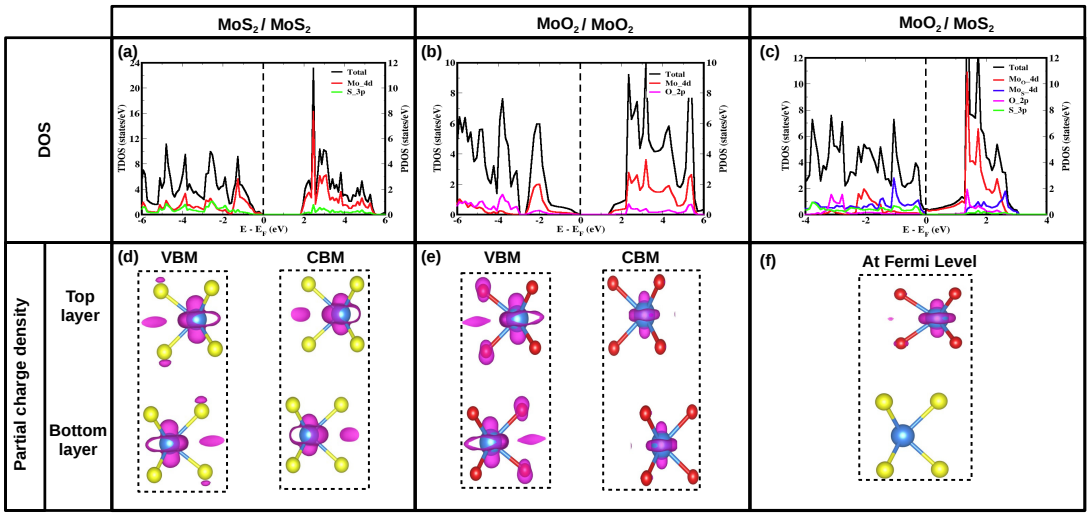

Figure 12: The calculated TDOS and PDOS of homobilayers (a) MoS_2/MoS_2, (b) MoO_2/MoO_2 and heterobilayer (c) MoO_2/MoS_2 for the most stable stacking (AA1). The dashed line represent the Fermi level. The calculated partial charge densities of homobilayers (d) MoS_2/MoS_2, (e) MoO_2/MoO_2 and heterobilayer (f) MoO_2/MoS_2.

For the homobilayer MoS_2/MoS_2 and MoO_2/MoO_2 systems, AA1 stacking is energetically most favorable. This is in good agreement with the previous theoretical work [65, 55]. Similarly, the stacking type AA1 has the lowest formation energy in the case of the heterobilayer MoO_2/MoS_2.

Regarding the electronic properties of these materials, the homobilayers MoS_2/MoS_2 and MoO_2/MoO_2 in different stacking are semiconductor materials with the reduced band gap values as compared to those of single layer counterparts. In both homobilayer cases, AA type presents the largest band gap value while AB type has the lowest value (see Table. 5). In order to understand the origin of the reduction in the band gap, the PDOS of the most energetically stable bilayers are depicted in Fig. 12. A downwards shift

of the CBM to the Fermi level is observed, and this is due to the presence of the 4*d* orbital of the Mo atom. This orbital states shift is mainly responsible for the reduction of the band gap. In the other hand, the VBM states are populated by the Mo 4*d* orbital and S 3*p* (O 2*p*) orbital. These distributions reconcile with the partial charge density analysis (see Fig. 12(d-e)). In the case of heterobilayer MoO_2/MoS_2, a metallic behavior is observed for all type of stacking orders. The PDOS reveal that the electronic states crossing the Fermi level arise from Mo 4*d* orbital of the MoO_2 layer (Fig. 12(c)). This is confirmed by the partial charge density distributions populated at the Mo atom of the MoO_2 layer (Fig. 12(f)).

4. Conclusion

In this paper, we performed a comparative study of all possible O line-ordered, cluster and random alloy configurations in a 5×5 supercell of MoS_2 monolayer for nanotechnological applications. An intensive comparative study on the thermodynamic stability, structural and electronic properties of these configurations have been considered. For each alloy shape, the most stable configuration at every concentration is identified and further characterized. Their noted relatively low formation energies suggest that these alloyed systems are thermodynamically stable and can easily be synthesized at low temperature using methods such as CVD technique or can easily be exfoliated from their bulk counterparts. The comparative study presented in this paper encourages the experimental synthesis of the line-ordered alloys since they are constantly energetically most stable at each concentration. Moreover, the effect of the O atoms greatly reduces the lat-

tice constant of the MoS_2 monolayer thereby obeying the Vegard's law. Most importantly, alloying with the O atoms fine tunes the band gap of the MoS_2 monolayer. The range of the obtained band gap values (2.17 eV (MoS_2) - 0.98 eV (MoO_2)) satisfies the requirement of nanoelectronic and solar cell applications. Creation of stacking of MoS_2 with MoO_2 gives metallic character, with Mo $4d$ orbital crossing the Fermi level. In conclusion, the O atom concentration and the atomic arrangement greatly affect the electronic structures of the MoS_2 monolayer, and the noted band gap variation can be beneficial for electronic device design.

Acknowledgment

The authors would like to acknowledge the University of Pretoria for computational resources and financial support. NC would also like to thank the National Institute of Theoretical Physics for financial support.

References

[1] B. Radisavljevic, A. Radenovic, J. Brivio, i. V. Giacometti, A. Kis, Nat. Nanotechnol 6 (3) (2011) 147–150.

[2] C. Lee, X. Wei, J. W. Kysar, J. Hone, science 321 (5887) (2008) 385–388.

[3] A. Kuc, T. Heine, A. Kis, MRS Bulletin 40 (7) (2015) 577–584.

[4] Y. Kubota, K. Watanabe, O. Tsuda, T. Taniguchi, Science 317 (5840) (2007) 932–934.

[5] A. K. Geim, K. S. Novoselov, Nat. Mater 6 (3) (2007) 183–191.

[6] J. C. Meyer, A. Chuvilin, G. Algara-Siller, J. Biskupek, U. Kaiser, Nano Lett 9 (7) (2009) 2683–2689.

[7] K. F. Mak, C. Lee, J. Hone, J. Shan, T. F. Heinz, Phys. Rev. Lett 105 (13) (2010) 136805.

[8] L. Xie, Nanoscale 7 (44) (2015) 18392–18401.

[9] C. Ataca, H. Sahin, S. Ciraci, J. Phys. Chem. C 116 (16) (2012) 8983–8999.

[10] F. A. Rasmussen, K. S. Thygesen, J. Phys. Chem. C 119 (23) (2015) 13169–13183.

[11] Y. Zhou, C. Geng, Nanotechnology 28 (10) (2017) 105402.

[12] H.-P. Komsa, A. V. Krasheninnikov, J. Phys. Chem. Lett 3 (23) (2012) 3652–3656.

[13] J. Kang, S. Tongay, J. Li, J. Wu, J. Appl. Phys 113 (14) (2013) 143703.

[14] N. Andriambelaza, R. Mapasha, N. Chetty, J. Phys. Condens. Matter 29 (32) (2017) 325504.

[15] B. Rajbanshi, S. Sarkar, P. Sarkar, Phys. Chem. Chem. Phys 17 (39) (2015) 26166–26174.

[16] H.-P. Komsa, A. V. Krasheninnikov, Phys. Rev. B 91 (12) (2015) 125304.

[17] K. Santosh, R. C. Longo, R. Addou, R. M. Wallace, K. Cho, Nanotechnology 25 (37) (2014) 375703.

[18] S. Haldar, H. Vovusha, M. K. Yadav, O. Eriksson, B. Sanyal, Phys. Rev. B 92 (23) (2015) 235408.

[19] C. González, B. Biel, Y. J. Dappe, Nanotechnology 27 (10) (2016) 105702.

[20] S.-C. Lu, J.-P. Leburton, Nanoscale Res. Lett 9 (1) (2014) 676.

[21] K. Dolui, I. Rungger, C. D. Pemmaraju, S. Sanvito, Phys. Rev. B 88 (2013) 075420.

[22] A. V. Krivosheeva, V. L. Shaposhnikov, V. E. Borisenko, J.-L. Lazzari, C. Waileong, J. Gusakova, B. K. Tay, J. Semicond. 36 (12) (2015) 122002.

[23] J. Suh, T.-E. Park, D.-Y. Lin, D. Fu, J. Park, H. J. Jung, Y. Chen, C. Ko, C. Jang, Y. Sun, et al., Nano letters 14 (12) (2014) 6976–6982.

[24] Y.-C. Lin, D. O. Dumcenco, H.-P. Komsa, Y. Niimi, A. V. Krasheninnikov, Y.-S. Huang, K. Suenaga, Adv. Mater. 26 (18) (2014) 2857–2861.

[25] Q. Yue, J. Kang, Z. Shao, X. Zhang, S. Chang, G. Wang, S. Qin, J. Li, Phys. Lett A 376 (12-13) (2012) 1166–1170.

[26] P. Lu, X. Wu, W. Guo, X. C. Zeng, Phys. Chem. Chem. Phys. 14 (37) (2012) 13035–13040.

[27] E. Scalise, M. Houssa, G. Pourtois, V. Afanasev, A. Stesmans, Nano Research 5 (1) (2012) 43–48.

[28] K. He, C. Poole, K. F. Mak, J. Shan, Nano letters 13 (6) (2013) 2931–2936.

[29] P. Johari, V. B. Shenoy, ACS nano 6 (6) (2012) 5449–5456.

[30] D. Dumcenco, K. Chen, Y. Wang, Y. Huang, K. Tiong, J. Alloys Compd 506 (2) (2010) 940–943.

[31] Y. Chen, J. Xi, D. O. Dumcenco, Z. Liu, K. Suenaga, D. Wang, Z. Shuai, Y.-S. Huang, L. Xie, Acs Nano 7 (5) (2013) 4610–4616.

[32] T. L. Tan, M.-F. Ng, G. Eda, J. Phys. Chem. C 120 (5) (2016) 2501–2508.

[33] X.-L. Wei, H. Zhang, G.-C. Guo, X.-B. Li, W.-M. Lau, L.-M. Liu, J. Mater. Chem. A 2 (7) (2014) 2101–2109.

[34] P. M. Larsen, A. R. Kalidindi, S. Schmidt, C. A. Schuh, Acta Mater. 139 (2017) 254–260.

[35] L.-Y. Gan, Q. Zhang, Y.-J. Zhao, Y. Cheng, U. Schwingenschlögl, Scientific reports 4 (2014) 6691.

[36] Q. Feng, N. Mao, J. Wu, H. Xu, C. Wang, J. Zhang, L. Xie, ACS nano 9 (7) (2015) 7450–7455.

[37] Q. Feng, Y. Zhu, J. Hong, M. Zhang, W. Duan, N. Mao, J. Wu, H. Xu, F. Dong, F. Lin, et al., Adv. Mater 26 (17) (2014) 2648–2653.

[38] N. Andriambelaza, R. Mapasha, N. Chetty, Physica B: Condens. Matter 535 (2018) 162 – 166.

[39] G. Kresse, J. Furthmüller, Phys. Rev. B 54 (16) (1996) 11169.

[40] J. P. Perdew, K. Burke, M. Ernzerhof, Phys. Rev. Lett 77 (18) (1996) 3865.

[41] Á. Morales-García, R. Valero, F. Illas, J. Phys. Chem. C 121 (34) (2017) 18862–18866.

[42] J. Heyd, G. E. Scuseria, M. Ernzerhof, J. Chem. Phys. 118 (18) (2003) 8207–8215.

[43] Y. Zhong, A. Luo, J. Nie, J. O. Sofo, Z.-K. Liu, in: Essential Readings in Magnesium Technology, Springer, 2016, pp. 427–432.

[44] C. Jiang, Y. Du, J. Appl. Phys 109 (2) (2011) 023504.

[45] U. K. Sen, P. Johari, S. Basu, C. Nayak, S. Mitra, Nanoscale 6 (17) (2014) 10243–10254.

[46] J. Su, N. Li, Y. Zhang, L. Feng, Z. Liu, AIP Advances 5 (7) (2015) 077182.

[47] Y. Li, Y.-L. Li, C. M. Araujo, W. Luo, R. Ahuja, Catal. Sci. Technol 3 (9) (2013) 2214–2220.

[48] P. Young, J. Phys. D Appl. Phys. 1 (7) (1968) 936.

[49] A. Ramirez-Torres, D. Le, T. S. Rahman, in: IOP Conf. Ser. Mater. Sci. Eng., Vol. 76, IOP Publishing, 2015, p. 012011.

[50] H. Wan, L. Xu, W.-Q. Huang, J.-H. Zhou, C.-N. He, X. Li, G.-F. Huang, P. Peng, Z.-G. Zhou, RSC Adv. 5 (11) (2015) 7944–7952.

[51] C. Ataca, S. Ciraci, J. Phys. Chem. C 115 (27) (2011) 13303–13311.

[52] D. Wang, L.-M. Liu, S.-J. Zhao, Z.-Y. Hu, H. Liu, J. Phys. Chem. C 120 (9) (2016) 4779–4788.

[53] A. Kumar, P. Ahluwalia, Mater. Chem. Phys. 135 (2-3) (2012) 755–761.

[54] Y. Ji, M. Yang, H. Lin, T. Hou, L. Wang, Y. Li, S.-T. Lee, J. Phys. Chem. C 122 (5) (2018) 3123–3129.

[55] Z. Fan, Z. Wei-Bing, T. Bi-Yu, Chin. Phys. B 24 (9) (2015) 097103.

[56] Y. Jing, X. Tan, Z. Zhou, P. Shen, J. Mater. Chem. A 2 (40) (2014) 16892–16897.

[57] J. Zhang, S. Jia, I. Kholmanov, L. Dong, D. Er, W. Chen, H. Guo, Z. Jin, V. B. Shenoy, L. Shi, et al., ACS nano 11 (8) (2017) 8192–8198.

[58] A. Zunger, S.-H. Wei, L. Ferreira, J. E. Bernard, Phys. Rev. Lett 65 (3) (1990) 353.

[59] Y. Huang, X. Chen, D. Zhou, H. Liu, C. Wang, J. Du, L. Ning, S. Wang, J. Phys. Chem. C 120 (10) (2016) 5839–5847.

[60] K. Jacob, S. Raj, L. Rannesh, Int. J. of Mater. Res 98 (9) (2007) 776–779.

[61] Y. Mao, X. Liang, G. Zhao, T. Song, in: J. Phys. Conf. Se, Vol. 490, IOP Publishing, 2014, p. 012172.

[62] H. M. Foronda, B. Mazumder, E. C. Young, M. A. Laurent, Y. Li, S. P. DenBaars, J. S. Speck, J. Cryst. Growth 475 (2017) 127–135.

[63] A. R. Denton, N. W. Ashcroft, Phys. Rev. A 43 (6) (1991) 3161.

[64] S. KC, R. C. Longo, R. M. Wallace, K. Cho, J. Appl. Phys 117 (13) (2015) 135301.

[65] T. Peng, G. Huai-Hong, Y. Teng, Z. Zhi-Dong, Chin. Phys. B 23 (10) (2014) 106801.

[66] W. Wei, Y. Dai, B. Huang, Phys. Chem. Chem. Phys. 19 (1) (2016) 663–672.

Chapter 6

Published paper: First-principles of tellurium line-ordered alloys in a MoS_2 monolayer

The work presented in this chapter has been published as N. F. Andriambelaza, R. E. Mapasha, N. Chetty, Physica B: Condensed Matter 535 (2018) 162 - 166.

In this chapter, a comparative study of the thermodynamic stability, structural and electronic properties of the Te line-ordered and random configurations are reported. Previous study on a MoS_2 monolayer alloyed with Te atoms only considered random alloy configurations and we aim to systematically study the effects of the Te atoms by considering the possible line-ordered alloy configurations at each concentration. The outcome of the study is found in the attached publication where the computational details used, discussion of the various results and conclusions are given.

First-principles studies of Te line-ordered alloys in a MoS_2 monolayer

N.F. Andriambelaza[a,*], R.E. Mapasha[a], N. Chetty[a,b]

[a] *Department of Physics, University of Pretoria, Pretoria 0002, South Africa*
[b] *National Institute for Theoretical Physics, Johannesburg, 2000, South Africa*

Abstract

The thermodynamic stability, structural and electronic properties of Te line-ordered alloys are investigated using density functional theory (DFT) methods. Thirty four possible Te line-ordered alloy configurations are found in a 5×5 supercell of a MoS_2 monolayer. The calculated formation energies show that the Te line-ordered alloy configurations are thermodynamically stable at 0K and agree very well with the random alloys. The lowest energy configurations at each concentration correspond to the configuration where the Te atom rows are far apart from each other (avoiding clustering) within the supercell. The variation of the lattice constant at different concentrations obey Vegard's law. The Te line-ordered alloys fine tune the band gap of a MoS_2 monolayer although deviating from linearity behavior. Our results suggest that the Te line-ordered alloys can be an effective way to modulate the band gap of a MoS_2 monolayer for nanoelectronic, optoelectronic and nanophotonic applications.

Keywords: Two dimensional materials, molybdenum disulfide, band gap.

1. Introduction

In the past decade, two dimensional (2D) materials have gained a lot of attention in various research fields due to their potential applications in electronic, optoelectronic and photonic devices. Graphene, a single sheet of graphite, was the first 2D layered material to be synthesized successfully [1]. Although it has exotic properties such as high electron mobility, high tensile strength and high mechanical flexibility [2, 3], its major shortcoming is the absence of a band gap [4]. Recently, the novel 2D materials known as transition metal dichalcogenides (TMD) such as molybdenum disulfide (MoS_2), molybdenum diselenide ($MoSe_2$) and molybdenum ditelluride ($MoTe_2$) are becoming attractive materials for nanotechnology applications (nanoelectronic, optoelectronic and nanophotonic applications) due to their sizable band gaps as well as high charge carrier mobility [5, 6].

Similar to graphene, MoS_2 monolayer has been synthesized using mechanical exfoliation [7, 8] and chemical vapor deposition (CVD) methods [9]. The MoS_2 monolayer is a semiconductor with a direct band gap of 1.8 eV (experimentally) [10] and 1.67 eV (theoretically) [6]. This issue of band gap is of great importance in the electronic applications of a MoS_2 monolayer. Moreover, in order to optimize the application of this material, engineering of the band gap is a critical idea to investigate.

Previous studies on MoS_2 monolayer reported that alloying at the Mo and S sites can fine tune the band gap of this material [10, 11]. Xu *et al.* [10] studied the effects of tungsten (W) and selenium (Se) alloys in the MoS_2 monolayer using CVD methods. They found that W alloys fine tune the band

gap of a MoS_2 monolayer from 1.8 eV to 1.97 eV, whereas Se alloys tune from 1.8 eV to 1.55 eV. They reported that band gap engineering is important to improve the nanoscale photoelectric devices such as the sensitivity and response rate. Kuc *et al.* [11] have performed the density functional theory (DFT) calculations to study the stability and electronic properties of the $MoS_{(1-x)}Se_x$ alloys. In agreement with the experiments [10], they found that these alloys are thermodynamically stable and successfully fine tune the band gap of the MoS_2 monolayer.

Note that the challenge in the theoretical study of alloying is the atomic arrangement. Depending on the position of the dopants, we can obtain different alloy configurations such as cluster, line or just random configurations. Combining all of them together brings a huge number of configurations at each concentration. Computing the physical properties of all these configurations is impracticable using first-principles methods. Most of the previous studies on alloying [11, 12] considered only random alloys. To the best of our knowledge, a systematic study of the line-ordered alloys configurations at different concentrations has not yet explored.

In this paper, we perform first-principles calculations to study the thermodynamic stability, structural and electronic properties of the Te line-ordered alloys in a MoS_2 monolayer. Only the S sites are substituted by the Te atoms since both are chalcogen atoms. We show that the incorporation of the Te atoms significantly affects the thermodynamic stability, the lattice constant and the electronic structure of the MoS_2 monolayer.

2. Computational details

First-principles calculations using the DFT methods as implemented in the Vienna *ab-initio* simulation package (VASP) [13] are performed to study the geometric structure, thermodynamic stability and electronic properties of the Te line-ordered alloys in a MoS_2 monolayer. The calculations are carried out in a 5×5 supercell of a MoS_2 monolayer. The generalized gradient approximation (GGA) parameterized by Perdew, Burke, and Ernzerhof (PBE) [14] is employed for the exchange-correlation potential. In DFT calculation, the standard GGA exchange-correlation is known to give an underestimated value of the pristine MoS_2 band gap [15]. The Heyd, Scuseria, and Ernzerhof exchange-correlation functional (HSE06) [16] has been proven to accurately predict the MoS_2 band gap values close to experimental values [17]. In this study, we compare the band gap value obtained using GGA exchange-correlation with the band gap obtained using HSE06 for the Te line-ordered alloys. In all the calculations, the projector augmented wave (PAW) method [18] is used for the pseudopotential generation. After convergence tests, a plane wave cutoff energy of 300 eV is considered. A k-grid of $2 \times 2 \times 1$ is used to sample the Brillouin zone. Both the lattice constants and atomic positions are fully relaxed. The relaxation convergence of energy is taken as 10^{-5} eV and the Hellmann-Feynman force between each atom set to less than 0.02 eV/Å. A vacuum spacing of 15 Å is used to isolate the single layer of MoS_2 and to suppress the spurious interlayer interaction along the z-axis.

The relative stabilities of the various possible Te line-ordered alloy con-

figurations are evaluated by calculating the formation energies given by:

$$E_{form} = E_{MoTe_xS_{1-x}} - (1-x)E_{MoS_2} - xE_{MoTe_2} \ , \tag{1}$$

where $E_{MoTe_xS_{1-x}}$, E_{MoS_2} and E_{MoTe_2} are the total energies of the mixed compound, the pristine MoS_2 and $MoTe_2$ monolayers, respectively. The x parameter is the concentration of Te atoms introduced in the MoS_2 monolayer [19].

3. Results and discussion

3.1. Structural aspects

In this study, the hexagonal structure of a MoS_2 monolayer is considered, since it has been reported that it is the most stable structure amongst different polytypes of MoS_2 monolayers [6]. Top view of this structure is shown in Fig. 1. It can be seen at a glance from Fig. 1 that the hexagonal MoS_2 monolayer is composed of three layers, one layer of the molybdenum (Mo) atoms sandwiched between two layers of the sulfur (S) atoms.

As mentioned above, we are interested in the study of the Te line-ordered alloys in a MoS_2 monolayer. To obtain the various unique Te line-ordered alloy configurations, we selectively consider the S atom sites along the zigzag of the MoS_2 monolayer. When applying this idea, the periodic boundary condition is always obeyed. The line formed by the S atoms along the zigzag is denoted by letter L shown in Fig. 1. L_1, L_2, L_3, L_4 and L_5 represent respectively the first, second, third, forth and fifth line of the S atoms along the zigzag. The letter u and b represent the upper and bottom layers of the S atoms respectively. There are ten possible rows of S atoms in a 5×5

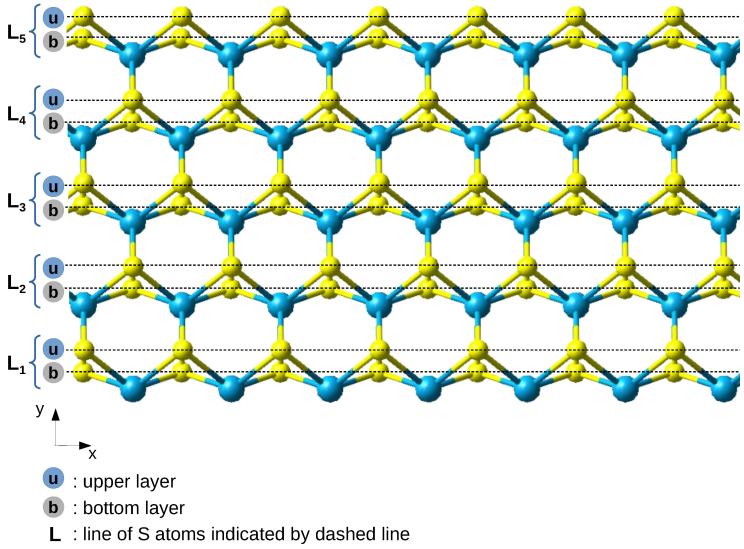

Figure 1: An hexagonal structure of a MoS_2 monolayer. The blue spheres indicate the Mo atoms and the light yellow spheres indicate the S atoms. u stand for upper layer and b for the bottom layer of the S atoms. L_1, L_2, L_3, L_4 and L_5 indicate respectively the first, second, third, forth and fifth line of S atoms along the zigzag in the 5 $\times$ 5 supercell of a MoS_2 monolayer.

supercell, five in the upper layer and the other five in the bottom layer (see Fig. 1).

Depending on the position of the Te atoms, various unique line-ordered alloys configurations can be possible at different concentrations of the Te atoms. In this work, five concentrations are chosen as $x = 0.1$ (10%), $x = 0.3$ (30%), $x = 0.5$ (50%), $x = 0.7$ (70%)and $x = 0.9$ (90%). For each concentration, different unique Te line-ordered alloy configurations are identified. We found thirty four possible unique Te line-ordered configurations: one configuration for 10%, eight configurations for 30%, sixteen configurations for 50%, eight configurations for 70% and one configuration for 90% as summarized

in Table. 1.

To better understand how to identify the Te line-ordered alloys, consider for instance the configuration L_{1u} at $x = 0.1$ (see Table. 1). It is constituted by the Te atoms substituting the upper (u) row of S atoms in line 1 (L_{1u}), denoted as $C_{1(0.1)}$. The configuration L_{1b} should be a possible configuration but due to the symmetry translation, it is the same as L_{1u}. To avoid double counting, the configuration $C_{1(0.1)}$ is the only possible configuration at $x = 0.1$. Therefore, double counting has been carefully avoided even at high concentration. For $C_{1(0.3)}$ given as $L_{1ub}L_{2u}$, the Te atoms occupy three rows

Table 1: Various Te line-ordered configurations at different concentrations.

	Concentration x				
Conf.	$x = 0.1$	$x = 0.3$	$x = 0.5$	$x = 0.7$	$x = 0.9$
C_1	L_{1u}	$L_{1ub}L_{2u}$	$L_{1ub}L_{2u}L_{3u}L_{4u}$	$L_{2ub}L_{3u}L_{4ub}L_{5ub}$	$L_{1b}L_{2ub}L_{3ub}L_{4ub}L_{5ub}$
C_2	-	$L_{1ub}L_{3b}$	$L_{1ub}L_{2ub}L_{3u}$	$L_{1u}L_{2u}L_{3u}L_{4ub}L_{5ub}$	-
C_3	-	$L_{1u}L_{2u}L_{3u}$	$L_{1ub}L_{2u}L_{3ub}$	$L_{1b}L_{2u}L_{3u}L_{4ub}L_{5ub}$	-
C_4	-	$L_{1u}L_{2u}L_{3b}$	$L_{1u}L_{2u}L_{3u}L_{4u}L_{5u}$	$L_{2u}L_{3ub}L_{4ub}L_{5ub}$	-
C_5	-	$L_{1u}L_{2u}L_{4u}$	$L_{1u}L_{2u}L_{3u}L_{4u}L_{5b}$	$L_{1ub}L_{2u}L_{3u}L_{4ub}L_{5u}$	-
C_6	-	$L_{1u}L_{2u}L_{4b}$	$L_{1u}L_{2u}L_{3u}L_{4b}L_{5b}$	$L_{1b}L_{2b}L_{3ub}L_{4u}L_{5ub}$	-
C_7	-	$L_{1u}L_{2b}L_{3u}$	$L_{1b}L_{2u}L_{3b}L_{4u}L_{5b}$	$L_{1b}L_{2u}L_{3b}L_{4ub}L_{5ub}$	-
C_8	-	$L_{1u}L_{2b}L_{4u}$	$L_{1ub}L_{2ub}L_{4u}$	$L_{1ub}L_{2b}L_{3ub}L_{4u}L_{5b}$	-
C_9	-	-	$L_{1ub}L_{2u}L_{3u}L_{4b}$	-	-
C_{10}	-	-	$L_{1ub}L_{2u}L_{3u}L_{5u}$	-	-
C_{11}	-	-	$L_{1ub}L_{2u}L_{3u}L_{5b}$	-	-
C_{12}	-	-	$L_{1ub}L_{2b}L_{3u}L_{5b}$	-	-
C_{13}	-	-	$L_{1ub}L_{2u}L_{3b}L_{5b}$	-	-
C_{14}	-	-	$L_{1ub}L_{2b}L_{3u}L_{4u}$	-	-
C_{15}	-	-	$L_{1ub}L_{2u}L_{3b}L_{4u}$	-	-
C_{16}	-	-	$L_{1ub}L_{2b}L_{4ub}$	-	-

of the S atoms. The upper (u) and bottom (b) rows of S atoms in L_1, and the upper (u) row of S atoms in L_2 are occupied. Following the same procedure, different unique configurations are possible at $x = 0.3$ to $x = 0.9$ as summarized in Table. 1. The atomic positions as well as the lattice constants of all Te line-ordered alloys configurations are optimized in order to study their relative thermodynamic stabilities and also to identify the lowest energy configuration at each concentration.

3.2. Thermodynamic stabilities of the Te line-ordered alloys

The feasibility and stability of the Te line-ordered alloy configurations are investigated by calculating the formation energy using Eq. 1. The formation energies of each configuration in Table. 1 are summarized in Table. 2. The calculated values allow us to recognize the lowest energy configuration at each concentration.

At $x = 0.1$ only one configuration $C_{1(0.1)}$ is possible, and has the lowest formation energy as compared to those of high concentration as shown in Table. 1. For comparison purpose, we used the special quasirandom structure (SQS) algorithm [20] to identify unique random alloy configurations at 10% (x=0.1) only. Few of the selected configurations are shown in Fig. 2. These random configurations are similar to those reported in Ref. [21, 22] for Se and Te alloys. We found that the formation energy of the $C_{1(0.1)}$ although slightly higher by 0.002 eV on average, compares very well with those of random alloys. Even though the formation energies are positive, their magnitudes are very small, on the order of ∼meV. Our random alloy configurations formation energies are in good agreement with those reported by Kang *et al.* [23], who argued that these types of system can be synthesized at experimentally

achievable temperatures. Therefore, since the formation energy of the $C_{1(0.1)}$ line-ordered alloy compares very well with those of random alloys, both systems should be synthesized at the same conditions.

At 30% concentration, configuration $C_{8(0.3)}$ is the most stable structure

Table 2: Formation energies of the various Te line-ordered configurations at different concentrations. The bold values indicate the lowest energy at each concentration.

	Formation energies (meV)				
Conf.	$x = 0.1$	$x = 0.3$	$x = 0.5$	$x = 0.7$	$x = 0.9$
C_1	**7.6**	18.9	34.4	16.8	**7.5**
C_2	-	16.7	24.7	35.1	-
C_3	-	30.2	21.3	16.2	-
C_4	-	15.6	66.0	20.6	-
C_5	-	28.2	31.4	33.0	-
C_6	-	16.2	16.7	15.6	-
C_7	-	12.9	**12.8**	15.4	-
C_8	-	**12.2**	22.1	**14.1**	-
C_9	-	-	17.4	-	-
C_{10}	-	-	35.6	-	-
C_{11}	-	-	19.4	-	-
C_{12}	-	-	18.7	-	-
C_{13}	-	-	18.2	-	-
C_{14}	-	-	18.8	-	-
C_{15}	-	-	15.7	-	-
C_{16}	-	-	19.1	-	-

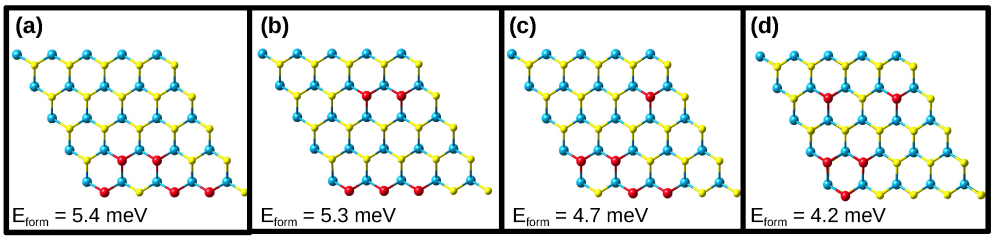

Figure 2: Selected different random alloy configurations at 10% (x= 0.1) consisting of 5Te substituting S atoms.

and configuration $C_{3(0.3)}$ is the most unstable one. The configuration $C_{8(0.3)}$ corresponds to the configuration $L_{1u}L_{2b}L_{4u}$ (see Table. 1), where the Te atoms occupy the upper (u) row of S atoms in L_1, the bottom (b) row of S atoms in L_2 and the upper (u) row of S atoms in L_4 as seen in Fig. 3b. Contrary, the highest energy configuration ($C_{3(0.3)}$) is the configuration where the rows of the Te atoms are settled next to each other and occupy the same layer as $L_{1u}L_{2u}L_{3u}$ (see Table. 1). We realized that the formation energies of the configurations depend on the separation of the Te atom rows within the supercell. In the highest energetically configuration $C_{3(0.3)}$, all the three Te rows are close to each other, each separated by 3.27 Å on the upper layer. In configuration $C_{8(0.3)}$, $L_{1u}L_{2b}L_{4u}$, the two Te rows $L_{1u}L_{2b}$ are separated by 4.46 Å, but the third row L_{4u} is relatively far 7.08 Å away within the supercell, and this is the most stable configuration. Considering the periodic boundary condition as usual, L_{4u} row is 6.34 Å away from L_{1u} in the next cell, thus this separation is still large making the structure stable. Nevertheless, due to very smaller energy difference, both configurations can be achieved experimentally under the same conditions. The same observation is found

at 50% (as seen in Fig. 3c) and at 70% (as seen in Fig. 3d). Note that the highest formation energy value is found at around 70%. This trend is in agreement with the results of Rajbanshi *et. al.* on the study of Se and Te random alloy configurations [21] and they argued that the formation of such kind of alloys is greatly composition dependent. In general, the Te alloys prefer to be at a distance far away from each other as opposed to transition metal alloys where the substituted atoms prefer to be next to each other [11].

The introduction of the Te line-ordered alloys affects the lattice constant of the MoS_2 monolayer since the atomic size of the Te atoms is larger than that of the S atoms. Fig. 4 shows the lattice constant of the lowest energy configuration at each concentration ($C_{1(0.1)}$, $C_{8(0.3)}$, $C_{7(0.5)}$, $C_{8(0.7)}$ and $C_{1(0.9)}$). We can see in Fig. 4 that the lattice constant increases linearly with the increase in concentration. The lattice constant values vary between the lattice constants of a MoS_2 monolayer (3.18 Å) and a $MoTe_2$ monolayer

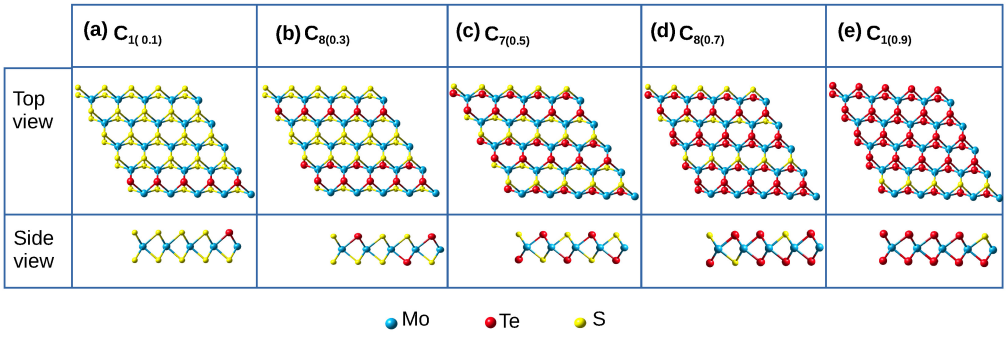

Figure 3: Top view and side view of the lowest energy configuration at (a) 10%, configuration $C_{1(0.1)}$; (b) 30%, configuration $C_{8(0.3)}$; (c) 50%, configuration $C_{7(0.5)}$; (d) 70%, configuration $C_{8(0.7)}$ and (e) 90%, configuration $C_{1(0.9)}$.

(3.54 Å). Indeed, the Te line-ordered alloys cause an outward strain in the system and the lattice constant obey Vegard's law. This behavior has already been experimentally found in the 2D TMD random alloys [24].

3.3. Electronic properties of the Te line-ordered alloys

Both 2D MoS_2 and $MoTe_2$ monolayers are semiconductor materials with the band gap values of 1.65 eV ($x = 0$ in Fig. 6) and 1.04 eV ($x = 1$ in Fig. 6), respectively. These values are in agreement with the values reported in Refs. [6, 24]. To explore the effects of the Te line-ordered alloys on the electronic properties of the MoS_2 monolayer, we calculate the total density of states (TDOS) at each concentration. Fig. 5 shows the TDOS of the lowest energy configurations at each concentration. Then, the magnitudes of the band gap at each concentration are measured and plotted in Fig. 6. The black (red) line indicates the band gap of the Te line-ordered alloys at

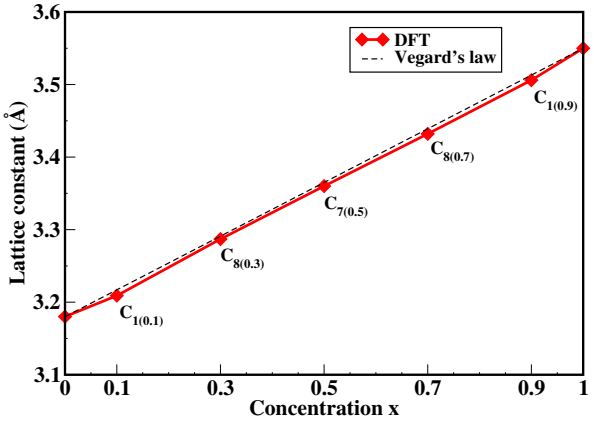

Figure 4: The lattice constants for the lowest energies configurations of the Te line-ordered alloys at different concentration (red line). The black dashed line shows the lattice constants obtained by using Vegard's law.

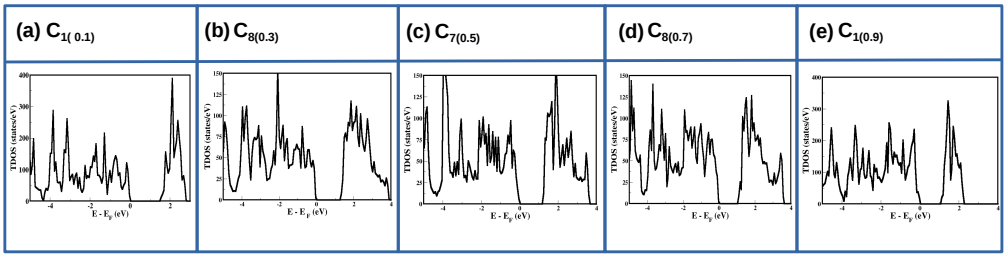

Figure 5: Total density of states (TDOS) for the lowest energy configurations at each concentration.

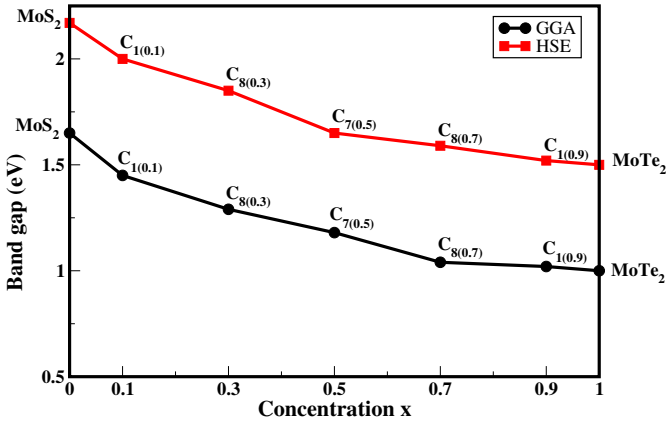

Figure 6: The calculated band gaps of the lowest energy configurations at each concentration. The black and red lines are the band gaps obtained using GGA and HSE exchange-correlation, respectively.

different concentrations using GGA (HSE) exchange-correlation functional. The values of the band gap decrease with the increase in Te concentration towards that of $MoTe_2$ monolayer (see Fig. 6). Unlike the lattice constant, the plot of the band gap deviates from the linearity behavior. The Te line-ordered alloys fine tune the band gap of the pristine MoS_2 monolayer from 1.65 eV (2.17 eV) to 1.04 eV (1.48 eV) using GGA(HSE) exchange-correlation

functional. The magnitudes of the band gaps depend on the composition of the alloys and cover the range of visible spectrum. Therefore, these materials can be used in solar related applications, for example as an absorber in a solar cell.

Fig. 6 compares the GGA and HSE band gap values. We realize that the HSE values are higher than that of GGA for the entire plots. However, the trend of the band gap plots (black line in Fig. 6 for GGA and red line for HSE) is the same. This indicates that the GGA functional can give a qualitative description of the electronic structure of various alloys in TMD materials.

4. Conclusion

In conclusion, using the density functional theory method, the lowest energy configuration at each concentration for the Te line-ordered alloys in a MoS_2 monolayer has been identified to optimize the applications of the 2D MoS_2 in the nanotechology devices. The calculated formation energies show that the Te line-ordered alloy configurations are thermodynamically stable at 0K and compete very well with the random alloys. The Te line-ordered alloys affect the lattice constant as well as the electronic properties of the MoS_2 monolayer. The lattice constant variation obeys Vegard's law and the band gap of the 2D MoS_2 is tuned between 1.65 eV and 1.04 eV. The range of band gap is related to the solar spectrum, indicating the importance of this study in nanoelectronic and nanophotonic, more especially in solar cell related devices.

Acknowledgment

The authors wish to thank the University of Pretoria for financial assistance. NRF and NIThep are greatly acknowledged.

References

[1] K. S. Novoselov, A. K. Geim, S. V. Morozov, D. Jiang, Y. Zhang, S. V. Dubonos, I. V. Grigorieva, A. A. Firsov, science 306 (5696) (2004) 666–669.

[2] J.-H. Chen, C. Jang, S. Xiao, M. Ishigami, M. S. Fuhrer, Nat. Nanotech. 3 (4) (2008) 206–209.

[3] C. Lee, X. Wei, J. W. Kysar, J. Hone, science 321 (5887) (2008) 385–388.

[4] A. C. Neto, F. Guinea, N. M. Peres, K. S. Novoselov, A. K. Geim, Rev. Mod. Phys. 81 (1) (2009) 109.

[5] X.-B. Li, P. Guo, Y.-N. Zhang, R.-F. Peng, H. Zhang, L.-M. Liu, J. Mater. Chem. C 3 (24) (2015) 6284–6290.

[6] F. A. Rasmussen, K. S. Thygesen, J. Mater. Chem. C 119 (23) (2015) 13169–13183.

[7] J. Wu, H. Li, Z. Yin, H. Li, J. Liu, X. Cao, Q. Zhang, H. Zhang, Small 9 (19) (2013) 3314–3319.

[8] I. Song, C. Park, H. C. Choi, RSC Advances 5 (10) (2015) 7495–7514.

[9] Y.-H. Lee, X.-Q. Zhang, W. Zhang, M.-T. Chang, C.-T. Lin, K.-D. Chang, Y.-C. Yu, J. T.-W. Wang, C.-S. Chang, L.-J. Li, et al., Adv. Mater. 24 (17) (2012) 2320–2325.

[10] W. Zhang, X. Li, T. Jiang, J. Song, Y. Lin, L. Zhu, X. Xu, Nanoscale 7 (32) (2015) 13554–13560.

[11] A. Kuc, T. Heine, Electronics 5 (1) (2015) 1.

[12] H.-P. Komsa, A. V. Krasheninnikov, J. Phys. Chem. Lett. 3 (23) (2012) 3652–3656.

[13] G. Kresse, J. Furthmüller, Comput. Mater. Sci. 6 (1) (1996) 15–50.

[14] J. P. Perdew, K. Burke, M. Ernzerhof, Phys. Rev. Lett. 77 (18) (1996) 3865.

[15] N. F. Andriambelaza, E. Mapasha, N. Chetty, J. Phys. Condens. Matter.[link].
URL http://iopscience.iop.org/10.1088/1361-648X/aa7a22

[16] J. Heyd, G. E. Scuseria, M. Ernzerhof, J. Chem. Phys. 118 (18) (2003) 8207–8215.

[17] M. Faraji, M. Sabzali, S. Yousefzadeh, N. Sarikhani, A. Ziashahabi, M. Zirak, A. Moshfegh, RSC Advances 5 (36) (2015) 28460–28466.

[18] P. E. Blöchl, Phys. Rev. B 50 (24) (1994) 17953.

[19] T. L. Tan, M.-F. Ng, G. Eda, J. Phys. Chem. C 120 (5) (2016) 2501–2508.

[20] A. Zunger, S.-H. Wei, L. Ferreira, J. E. Bernard, Phys. Rev. Lett. 65 (3) (1990) 353.

[21] B. Rajbanshi, S. Sarkar, P. Sarkar, Phys. Chem. Chem. Phys. 17 (39) (2015) 26166–26174.

[22] Q. Feng, Y. Zhu, J. Hong, M. Zhang, W. Duan, N. Mao, J. Wu, H. Xu, F. Dong, F. Lin, et al., Advanced Materials 26 (17) (2014) 2648–2653.

[23] J. Kang, S. Tongay, J. Li, J. Wu, J. Appl. Phys. 113 (14) (2013) 143703.

[24] S. Srivastava, D. Palit, Solid State Ion. 176 (5) (2005) 513–521.

Chapter 7

General conclusions

In this chapter, the obtained results are summarized, and general conclusions are drawn. The first-principles calculations based on the density functional theory (DFT) methods have been performed to study the band gap engineering of a MoS_2 monolayer using the transition metal (Cr) and chalcogen (O and Te) alloying. The thermodynamic stability, structural and electronic properties of the various line-ordered alloy configurations were intensively investigated. The obtained properties were compared with those of the well known random and/or cluster alloy configurations. The various alloy configurations were generated using the special quasirandom structure (SQS) method. Since it is known that the GGA functional underestimates the band gap of the real materials, the band gap values obtained in this study were improved using the HSE06 functional. We found that both functionals qualitatively predict similar trends in the physical properties, revealing that the GGA functional can qualitatively describe the physical behavior of a MoS_2 monolayer.

7.1 First-principles studies of chromium line-ordered alloys in a MoS_2 monolayer

The influence of the alloy Cr concentrations and configurations on the physical properties of a MoS_2 monolayer was primarily investigated. The study was divided into two parts: firstly, the effects of the Cr atom at low concentration (single and double dopants in a 5 $\times$ 5 supercell) were considered. By varying the position of the two dopants, four distinct configurations were identified. It was established that the two Cr dopants prefer to be close to each other in a MoS_2 monolayer supercell. At this low concentration, the Cr atom reduces the band gap of the MoS_2 monolayer, and the magnitude is Cr configuration dependent. Secondly, a systematic study of the Cr line-ordered alloy at five higher concentrations (0.2, 0.4, 0.6, 0.8, 1.0) was considered. Several Cr line-ordered alloy configurations were found to be possible at each concentration. The lowest energy configuration at each concentration was identified by calculating the formation energies of all configurations. Although our calculated formation energies of all the Cr line-ordered alloy configurations are positive, their values are very small ($\sim$ 60 meV) indicating that they can thermodynamically be stable under favorable condition. To compare the line-ordered alloy stability with those of well known experimental configurations, the random alloys were also designed using the SQS method, and their formation energies were also calculated. The hypothetical Cr line-ordered alloys compete very well with the random alloys at each concentration. This suggests that the line-ordered alloy can be synthesized under the same practical conditions as random. The introduction of the Cr atom also affected the structural network of a MoS_2 monolayer. After introduction of the Cr atoms, the 2D MoS_2 hexagonal symmetry was preserved and no induced buckling noted. However, the lattice constant of the alloyed system is smaller than that of pristine MoS_2 monolayer, and keep reducing with the increase in Cr concentration obeying the Vegard's law. Regarding the

electronic properties, the density of states (DOS) analysis revealed that the Cr alloying concentration and configuration fine-tuned the band gap of the MoS_2 monolayer. The reduction of the band gap is mainly contributed by the hybridization of the Cr $3d$ and Mo $4d$ orbitals at the vicinity of the band edges. The range of band gap value (0.86 to 1.65 eV) obtained from this alloy extends the available band gap of the 2D material for nanotechnology applications.

7.2 Band gap engineering of a MoS_2 monolayer through oxygen alloying: an *ab initio* study

A large number of O alloying configurations with different shapes such as random, cluster and line-ordered was considered. The thermodynamic stability, structural and electronic properties of these configurations were examined. The formation energies of the hypothetical O line-ordered alloys were found to compete very well with the well-known alloy shapes such as cluster and random alloys at low concentration. At high concentration, the line-ordered alloys dominate in terms of thermodynamic stability. Concerning the structural properties, the lattice constants of the O alloyed system decreased linearly with the increase in O concentration due to the effects of the small atomic radius of the O atom compared to the S atom. Most importantly, the O alloying fine-tunes the band gap of the MoS_2 monolayer continuously, from 1.65eV (2.17 eV) to 0.98 eV (1.48 eV) using GGA (HSE06) functional. The valence band maximum (VBM) states originate from hybridization of the Mo $4d$ and O $2p$ orbitals, while the conduction band minimum (CBM) states are mainly contributed by the Mo $4d$ orbital. The reduction of the band gap originates mainly from the shift in the CBM states to the inner side of the band gap. In the last part of this study, a bilayer material system was considered, to compare the band gap engineering from the in-plane, and vertical interactions between the MoS_2 and MoO_2 systems. All the stacking sequences of the

MoS_2 and MoO_2 structure give metallic characters at every concentration, with Mo $4d$ orbital crossing the Fermi level. The O alloys in a MoS_2 monolayer should be considered for an effective way to engineer the band gap for designing new nanoelectronic devices with innovative performance.

7.3 First-principles studies of tellurium line-ordered alloys in a MoS_2 monolayer

A systematic study of the tellurium (Te) alloy configurations at each concentration is still missing in the literature but that of selenium (Se) chalcogen is sufficient. The Se alloys are promising materials for future electronics. This motivated our study to explore the thermodynamic stability, structural and electronic properties of the Te line-ordered alloys using DFT methods. All the possible Te line-ordered alloys in a 5×5 supercell considering six different concentrations (0.1, 0.3, 0.5, 0.7, 0.9, 1.0) were investigated. The thermodynamic stability of these configurations was evaluated through the formation energies analysis. The formation energies of the Te line-ordered alloy configurations at 0K were found to be in good agreement with those of already experimentally achieved. The structural analysis revealed that the most stable line-ordered configuration at each concentration corresponds to the configuration of which the Te atom rows are far apart from each other (avoiding clustering) but within the supercell. The lattice constants variation of the Te alloyed systems is concentration dependent. The lattice constants increase linearly with the Te concentration obeying Vegard's law, due to the large atomic radius of the Te atom compared to the S atom. The DOS analysis revealed that the Te line-ordered alloys fine-tune the band gap of a MoS_2 monolayer but deviate from linear behavior. The same behavior was observed in the previously reported result on the random alloys. The band gap is tuned in the range of 1.04 to 1.65 eV (1.48 to 2.17 eV) using GGA (HSE06) functional. This observation

suggests that the Te line-ordered alloys can be an effective way to change the band gap of a MoS_2 monolayer to the desired electronic and optical functions.

7.4 Future Work

This thesis provides the essential investigations of the band gap engineering of a MoS_2 monolayer through alloying. It reveals the possibility of a systematic study of the alloying in a MoS_2 monolayer through line-ordered alloy configurations. This study can be extended to the other transition metal and chalcogen alloying in a MoS_2 monolayer such as MoS_2 monolayer alloyed with W or Se atoms. This would be beneficial for the fabrication of these MoS_2 monolayer alloyed systems. Although a thorough study of the band gap engineering of a MoS_2 monolayer was given in this thesis, the thermodynamic stability temperature dependent of the various alloying shapes is still missing. Since the DFT calculations are done at 0K, a finite temperature calculation method such as *ab initio* molecular dynamics is necessary to control the alloy structure through the temperature dependencies. Furthermore, most of the study on alloying in a MoS_2, including this work, focused on transition metal dichalcogenides (TMD) formed by the transition metal of group VIb. Further studies of alloying between MoS_2 monolayer with the other TMD monolayer apart from group VIb such as Ta, Nb, Fe, Re, Co, etc. should also be considered. It can be a source of a magnetic system that would be essential for spintronic applications.

Appendix A

First-principles studies of transition metal defects in a MoS_2 monolayer

As stated in the future work section, the study of a MoS_2 alloying with the block of transition metals surrounding the Mo atom in the periodic table (excluding the transition metals in the same group as Mo atom) is still missing. To get an insight into this study, we have already investigated the effects of the transition metal elements such as rhenium (Re) and tantalum (Ta) doping on the physical properties of the MoS_2 monolayer. The Re-doped MoS_2 monolayers were found not to be energetically stable. To enhance the stability of this system, a co-doping with Ta atom was considered. These studies is describded in the article below, published in the South African Institute of Physics (SAIP) proceedings, ISBN: 978-0-620-77094-1.

First-principles studies of transition metal defects in a MoS_2 monolayer

N F Andriambelaza[1], R E Mapasha[1] and N Chetty[1,2]

[1]Department of Physics, University of Pretoria, Pretoria 0002, South Africa
[2]National Institute for Theoretical Physics, Johannesburg 2000, South Africa

E-mail: arinala.f@gmail.com

Abstract. Density functional theory (DFT) implemented within the Vienna *ab-initio* simulation package (VASP), have been used to study the effects of transition metal defects (Rhenium (Re) and Tantalum(Ta)) on the thermodynamic stability and electronic properties of a MoS_2 monolayer. Calculations are performed using the projector augmented wave method (PAW) with the Perdew-Burke-Ernzerhof (PBE) for the exchange-correlation interactions. Our results show that Ta_{Mo} is a thermodynamically stable $p-$type defect whereas Re_{Mo} is a $n-$type with high cost of energy. To reduce the high energy cost of Re_{Mo} in a MoS_2, co-doping was considered. Our studies show that the co-doping of acceptors and donors to be accessible, the acceptors should dominate the donors. The variation of donors and acceptors in a MoS_2 monolayer tune the magnetic moment on and off. Our results indicate that combination of p-type (Ta) and n-type (Re) doped MoS_2 monolayers are promising materials for various electronic applications.

1. Introduction

Since its discovery, graphene has attracted considerable attention due to its unique electronic structure, high carrier mobility and exceptional strength [1]. Although it is a promising material for nanoelectronic devices, the absence of band gap inhibits its direct application. For this reason, researchers became interested in exploring other kind of two dimensional (2D) materials. The transition metal dichalcogenides (TDMCs) such as MoS_2, WS_2, $MoSe_2$, WSe_2, etc, are wide band gap semiconductors and are thermodynamically stable 2D materials [2]. Several studies have reported that MoS_2 monolayer has a band gap of about 1.90 eV experimentally [3] and of about 1.67 eV theoretically [4, 2]. Xu *et al*. reported that MoS_2 exhibits an excellent carrier mobility and desirable optical properties. These interesting properties make MoS_2 a suitable candidate for nanoelectronic devices [5].

During the synthesis of MoS_2 monolayer, point defects and impurities appear in the samples [6] just like in any materials. The presence of these defects are known to greatly alter the properties of pristine MoS_2 monolayer. It was reported that presence of the $p-$type and $n-$type defects causes semiconductor to metal transition in a MoS_2 system. Noh *et al*. reported that Rhenium (Re) impurities exist naturally in a MoS_2 monolayer and are $n-$type defects [7]. The valence band maximum (VBM) and conduction band minimum(CBM) states of a pristine MoS_2 monolayer are derived mainly from Mo $4d$ orbitals. This was shown by atomic resolution transmission electron microscopy [8]. In most studies of defects in a MoS_2 monolayer, Mo site is chosen in order to examine the influence of defects on the VBM and CBM states.

SA Institute of Physics ISBN: 978-0-620-77094-1 457

The widely studied $p-$type defect in MoS_2 is the Niobium (Nb) substituting Molybdenum (Nb_{Mo}). Dolui *et al*. reported that the presence of Nb_{Mo} has low formation energy and introduces impurity states above the VBM whose origin is the hybridisation of Nb and Mo d orbitals [9]. Lu *et al*. reported that the formation energy for Ta_{Mo} is lower than that of Nb_{Mo}. However, its electronic and magnetic properties have not been explored extensively [10]. Therefore, Tantalum (Ta) which is below Nb on the periodic table is also worth of investigation as an isolated defect (Ta_{Mo}) to learn how its interaction with MoS_2 influences the electronic and magnetic properties of MoS_2 monolayer.

In this paper, we examine the effect of Ta acceptor and Re donor defects on the thermodynamic stability and electronic properties of a MoS_2 monolayer. We also examine Ta and Re co-doping on MoS_2 monolayer. This will be to study the interaction of an acceptor (Ta) and donor (Re) defects on the stability and electronic properties of the system. We further identify Ta-Re configurations that have ferromagnet characteristics and low formation energy which will be important in spintronic application devices.

2. Methodology

In this work, density functional theory (DFT) [11] as implemented in the Vienna $ab-initio$ simulation package(VASP) [12] is employed to perform ab initio calculations on the electronic and magnetic properties of monolayer MoS_2 doped with Re and Ta impurities. All calculations are carried out using the projector augmented wave (PAW) pseudopotential and generalized gradient approximation (GGA) exchange correlation parameterized by Perdew, Burke, and Ernzerhof (PBE) [13]. A 5×5 hexagonal supercell with 75 atoms (25 Mo atoms and 50 S atoms) and having a vacuum region of 15 Å is employed to suppress the influence of neighboring layers. A kinetic energy cutoff of 250 eV for plane wave expansion and 2×2×1 k-point mesh are used. The atomic structures were relaxed until the Hellmann-Feynman forces were less than 0.02 eV/Å. The formation energies (E_{form}) of a particular dopant is defined as :

$$E_{form} = E_{tot}[MoS_2 + D] - E_{tot}[MoS_2] + \mu_{host} - \mu_D \text{ [6]} \quad (1)$$

where $E_{tot}[MoS_2+D]$ is the total energy of the MoS_2 monolayer with the substitutional atom D (Re or Ta), $E_{tot}[MoS_2]$ is the total energy of the pristine MoS_2 monolayer. μ_D and μ_{host}, are respectively the chemical potentials of the substitutional atom D (Re or Ta) and the host atom (Mo or S). All the chemical potentials are calculated by using the reference (stable) phase of each element. The orthorhombic structure is chosen for the sulphur and body center cubic (bcc) for Mo. μ_D is obtained from DFT total energies of a Ta bcc metal and Re hexagonal structure per atom.

3. Results and discussion

Before discussing the effect of dopant on a MoS_2 monolayer, let us analyse the electronic properties of the pristine MoS_2 monolayer. The top view and side view of a MoS_2 monolayer are shown in (Fig. 1). It can be seen that each of the S atom is bonded covalently to the three Mo atoms. Each Mo atom is coordinated with six S atoms, three of them make the top surface and other three to the bottom S layer. The band gap obtained using GGA functional for the pristine is 1.65 eV. This value is in good agreement with the experimental value of 1.90 eV and the previous theoretical results found in references [4, 2]. The VBM is mainly constituted from the hybridisation of Mo 4d and S 3p orbitals, whereas the CBM is mainly due to Mo 4d orbitals. The pristine of MoS_2 monolayer is a non-magnetic material in nature, since the spin up states are invertibly symmetric to spin down states for the entire plot. In the next section, we examine the effects of Ta and Re atoms on the electronic properties of a MoS_2 monolayer.

SA Institute of Physics ISBN: 978-0-620-77094-1 458

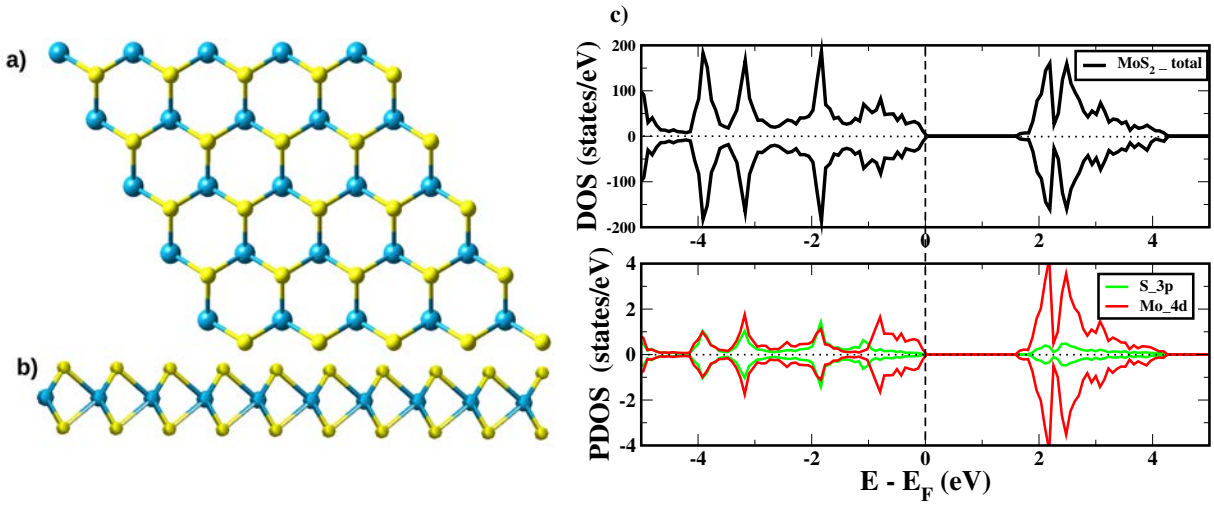

Figure 1. (a) Top view and (b) side view of a 5×5 MoS_2 monolayer. Blue spheres indicate Mo atoms and light yellow spheres indicate S atoms. (c) The total DOS and Projected DOS for a pristine MoS_2 monolayer. The positive DOS and PDOS values refer to majority spins, while the negative ones are for minority. The dashed line indicates the Fermi energy.

3.1. Ta substitution

Firstly, we analyse Ta atom(s) substituting Mo atom(s). The number of Ta dopants considered ranges between one and three (Ta_x where x = 1Mo, 2Mo and 3Mo) on a single hexagonal ringlike in a MoS_2 monolayer. When examining the structures, we found that the insertion of Ta atom in a MoS_2 monolayer affects the bond lengths. The relaxed Ta-S bonds for Ta_{1Mo}, Ta_{2Mo} and Ta_{3Mo} are 2.41, 2.46 and 2.47 Å respectively. The Mo-S bond length for the relaxed MoS_2 monolayer is 2.42 Å which is in good agreement with references [2, 9]. Therefore, we realise that the induced strain in Ta_{1Mo} is small, however in Ta_{2Mo} and Ta_{3Mo}, it is significantly large. This should have a significant effect on the other properties.

Table 1. Formation energies E_{form} (eV) and magnetic moments $m(\mu_B)$ of Ta and Re defects in a MoS_2 monolayer.

Type of doping	E_{form}(eV)	$m(\mu_B)$
Ta_{1Mo}	-0.43	0.01
Ta_{2Mo}	-0.97	0.00
Ta_{3Mo}	-1.73	0.00
Re_{1Mo}	2.18	1.00
Re_{2Mo}	4.02	0.00
Re_{3Mo}	5.73	1.00
$Ta_{1Mo}Re_{1Mo}$	0.09	0.01
$Ta_{2Mo}Re_{1Mo}$	-0.38	0.01
$Ta_{1Mo}Re_{2Mo}$	2.10	0.98

The relative stability of our defects is determined using the formation energies calculated using Eq.1. Table.1 shows that the formation energies of Ta_{Mo} (Ta_{1Mo}, Ta_{2Mo} and Ta_{3Mo}) are all negative. We realised that E_{form} becomes more energetically favourable when the number of defects increases. The negative formation energies indicate that the corresponding substitutional

reactions can occur spontaneously under favourable conditions. Ding *et al*. have reported that

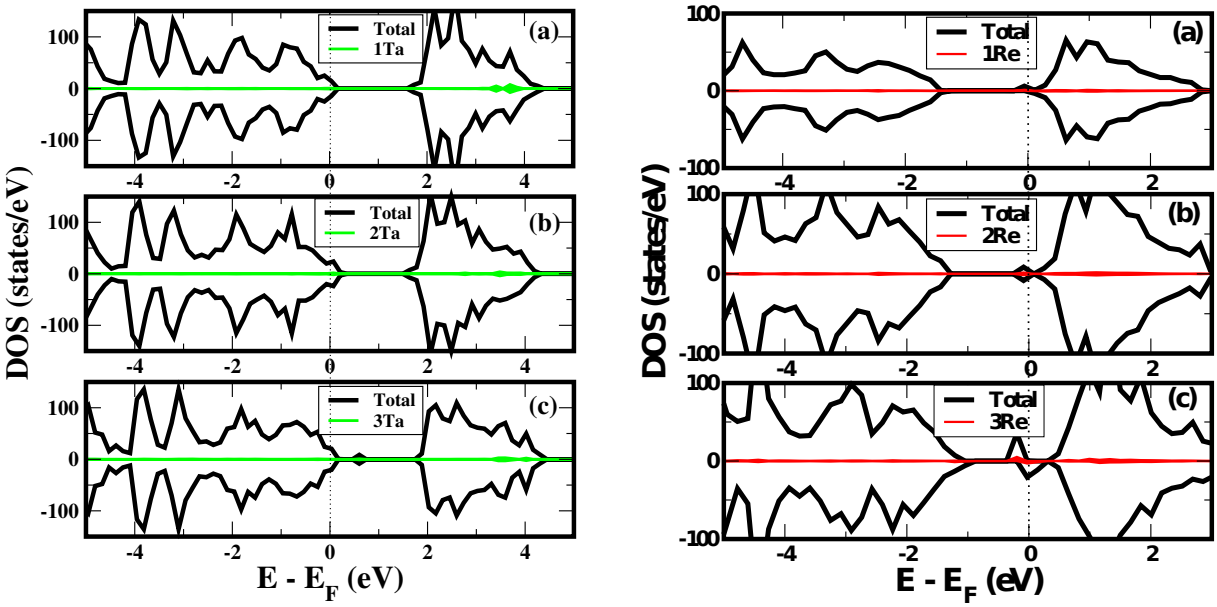

Figure 2. The Total DOS for a 5×5 supercell of (a) Ta_{1Mo}, (b) Ta_{2Mo}, (c) Ta_{3Mo}, (d) Re_{1Mo}, (e) Re_{2Mo} and (f) Re_{3Mo}. The positive DOS values refer to majority spins, while the negative ones are for minority. The dashed line indicates the Fermi energy.

Fig. 2 shows the density of states (DOS) plots for Ta_{1Mo} (Fig. 2(a)), Ta_{2Mo} (Fig. 2(b)) and Ta_{3Mo} (Fig. 2(c)). We found that the effect of Ta substituting Mo is to shift the Fermi level into the valence band. This shift is an indication that Ta_{1Mo}, Ta_{2Mo} and Ta_{3Mo} systems have deficiency of electrons compared to MoS_2. Therefore, Ta_{Mo} systems are p-type defects in a MoS_2 monolayer and can act as an electron trap. In a Ta_{3Mo} DOS, we also noted an extra non-spin polarised impurity states at 0.47 eV above the VBM within the band gap. These exotic impurities states are relative deep, and therefore will unlikely be ionised at room temperature [14]. Fig. 2 also shows that in all cases, the minority spin is aligned to the majority spin revealing that the systems are non-magnetic (see Table.1). Nevertheless, Ta defect is energetically stable and can be a suitable p-type dopant for MoS_2 monolayer.

3.2. Re substitution

The formation energies of Re defect configurations, Re_{1Mo}, Re_{2Mo} and Re_{3Mo}, are shown in Table.1. They are all positive indicating that the cost of substituting Mo with Re is energetically expensive. We further found that when the number of Re dopants in the system increases, i.e Re_{3Mo}, the system gradually becomes more energetically unstable. The DOS of Re_{1Mo}, Re_{2Mo} and Re_{3Mo} are shown in Fig. 2(a), Fig. 2(b) and Fig. 2(c) respectively.

For Re_{1Mo} system, we found that the induced defect state is near but at 0.25 eV below the CBM . This state is formed by hybridisation of the Re 5d orbitals with the Mo 4d orbitals. The creation of Re_{1Mo} add an electron into the system, resulting in shifting the Fermi level into the CB. This reveals that Re_{1Mo} system is a $n-$type. The DOS of Re_{1Mo} (Fig.2(d)) also shows that the majority spin and minority spin are asymmetric leading the system been magnetic with a magnetic moment of $1\mu_B$. This is in good agreement with reference [9].

The substitution of two Re dopants induces non-spin polarised states at 0.19 eV below the CBM. This system is non-magnetic in nature. This might be due to the effect of pairing of localised electrons each contributed by defect. However, the introduction of three Re defects for the Re_{3Mo} system induces spin-polarised states in the gap around 0.3 eV below the CBM. A magnetic moment of $1\mu_B$ in this defective system is noted. The half metallic character is also noted in Re_{3Mo} as the Fermi level crosses only the spin down states. The systems that are half metallic ferromagnet have a future application in the spintronic technology.

Since the intrinsic defects are inefficient to create a $n-$type MoS_2 monolayer [9], our results indicate that Re is a plausible for a $n-$type dopant in MoS_2 although highly expensive to form.

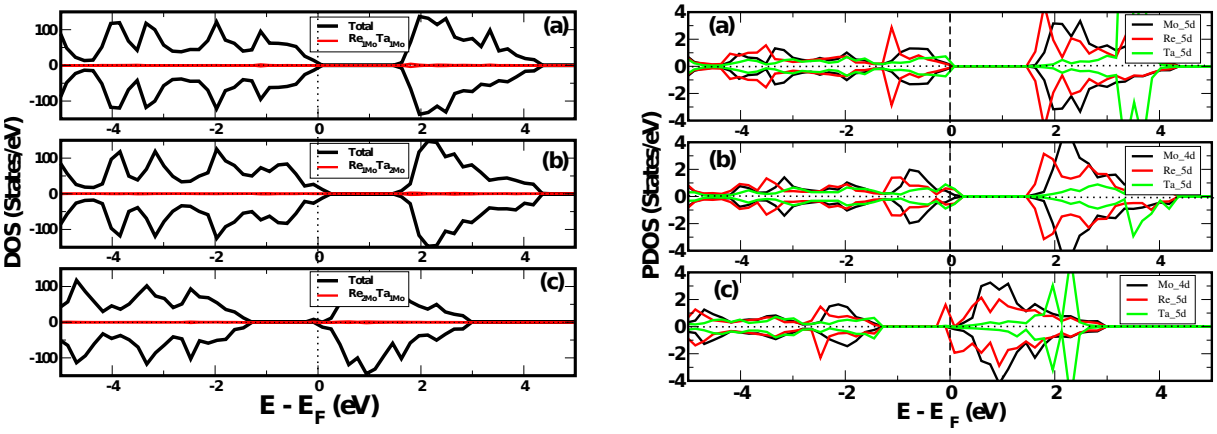

Figure 3. The total DOS(left) and Projected DOS(right) for (a) $Ta_{1Mo}Re_{1Mo}$, (b) $Re_{1Mo}Ta_{2Mo}$ and (c) $Re_{2Mo}Ta_{1Mo}$. The dashed line indicates the Fermi energy.

3.3. Re and Ta co-doping

Lastly, we examine the co-doping of the Re and Ta dopants in a MoS_2 monolayer. It has been reported that Re exists spontaneously during the synthesis of the MoS_2 samples and an $n-$type device was characterised. We model the interactions of naturally existing Re defects with Ta dopants in a MoS_2 system. This will be to give an explanation of how the unintentional donors can be controlled by acceptors in a MoS_2 monolayer.

Substitution around the ringlike hexagonal is considered by varying the number of dopants. The three possible defects denoted as $Re_{1Mo}Ta_{1Mo}$, $Re_{1Mo}Ta_{2Mo}$ and $Re_{2Mo}Ta_{1Mo}$ are considered. Table.1 shows that the formation energies of these defects are higher than that of isolated acceptors (Ta) doping but lower than that of donors (Re) doping. The relatively low formation energy for $Re_{1Mo}Ta_{1Mo}$ of 0.09 eV albeit positive, do not rule out the possibility of synthesising this material at an ambient conditions. The substitution of a second acceptor making $Re_{1Mo}Ta_{2Mo}$ system yields a low formation energy of -0.38 eV. However two donors and one acceptor $Re_{2Mo}Ta_{1Mo}$ is a problem because the formation of this system is endothermic. For such defects to be easily accessible under ambient conditions, acceptors should always dominate the donors.

For the first case of $Re_{1Mo}Ta_{1Mo}$, the DOS is quite similar to the pristine (Fig. 3(a)). Since Re has one electron more and Ta has one electron less compared to Mo, those two excess electrons compensate each other. Therefore, the compensation does not alter much the electronic behaviour of the MoS_2 monolayer. But for $Re_{1Mo}Ta_{2Mo}$, we observe that the Fermi level is shifted deeper into the VB. This is to ensure that $Re_{1Mo}Ta_{2Mo}$ behave as $n-$type material. The system is, however, non-spin polarised with no magnetic moment obtained.

SA Institute of Physics *ISBN: 978-0-620-77094-1* *461*

In the case of $Re_{2Mo}Ta_{1Mo}$, impurities states appear near the CBM. They are originated from 5d orbital of Re (Fig. 3(a)). The Fermi level is shifted closer to the CBM which indicates that $Re_{2Mo}Ta_{1Mo}$ has a p-type behaviour. After the compensation of one electron from Re and one from Ta, there is still one unpaired electron in the system which makes the system ferromagnetic with a magnetic moment of $1\mu_B$.

4. Conclusion

We have successfully studied the electronic properties and the thermodynamic stability of a MoS_2 monolayer doped with Re and Ta atoms using DFT approximation. We considered isolated doping along a single hexagonal ringlike in a 5×5 supercell of MoS_2 monolayer. We found that Ta atom doping is thermodynamically stable (exothermic) for all possible defect configurations. Ta doping also show a $p-$type features in MoS_2 monolayer. For Re doping, the formation energies are positive (endothermic) for all defect configurations considered. For Re_{1Mo} and Re_{3Mo} the system show ferromagnetic features with a magnetic moment of about $1\mu_B$. The DOS analysis of Re doping possess $n-$type characteristics. In trying to control or lower the high formation energy of Re doping co-doping of Ta with Re was also considered. This was to combine donors (Re) with acceptors (Ta) in a MoS_2 monolayer. Three configurations were investigated $Ta_{1Mo}Re_{1Mo}$, $Re_{1Mo}Ta_{2Mo}$ and $Re_{2Mo}Ta_{1Mo}$. $Re_{Mo}Ta_{2Mo}$ is the most energetically favourable configuration whereas $Re_{2Mo}Ta_{1Mo}$ is the least. For a co-doping to be releasable under ambient conditions, acceptors should dominate the donors. Our results suggest that these systems might be useful in various electronic and spintronic devices applications.

Acknowledgments

The authors would like to thank the University of Pretoria for computational resources and financial support. We also thank R.C. Andrew and E. Igumbor for useful discussions.

References

[1] Geim A K and Novoselov K S 2007 *Nat. Mater.* **6** 183–191
[2] Ding Y, Wang Y, Ni J, Shi L, Shi S and Tang W 2011 *Phys.* B **406** 2254–60
[3] Izyumskaya N, Demchenko D O, Avrutin V, Özgür Ü and Morkoç H 2014 *Turk. J. Phys.* **38** 478–496
[4] Faraji M, Sabzali M, Yousefzadeh S, Sarikhani N, Ziashahabi A, Zirak M and Moshfegh A 2015 *RSC Adv.* **5** 28460–66
[5] Xu M, Liang T, Shi M and Chen H 2013 *Chem. Rev.* **113** 3766–98
[6] Komsa H P and Krasheninnikov A V 2015 *Phys. Rev.* B **91** 125304
[7] Noh J Y, Kim H and Kim Y S 2014 *Phys. Rev.* B **89** 205417
[8] Lin Y C, Dumcenco D O, Komsa H P, Niimi Y, Krasheninnikov A V, Huang Y S and Suenaga K 2014 *Adv. Mater.* **26** 2857–61
[9] Dolui K, Rungger I, Pemmaraju C D and Sanvito S 2013 *Phys. Rev.* B **88** 075420
[10] Lu S C and Leburton J P 2014 *Nanoscale Res. Lett.* **9** 1–9
[11] Kohn W and Sham L J 1965 *Phys. Rev.* **140** A1133
[12] Hafner J 2008 *J. Comput. Chem.* **29** 2044–78
[13] Perdew J P, Burke K and Ernzerhof M 1996 *Phys. Rev. Lett.* **77** 3865
[14] Freysoldt C, Grabowski B, Hickel T, Neugebauer J, Kresse G, Janotti A and Van de Walle C G 2014 *Rev. Mod. Phys.* **86** 253

Appendix B

Special quasirandom structure

The main focus of this thesis is to create substitutional alloying in a MoS_2 monolayer. This can be generalized as a binary alloy with the form of $A_{1-x}B_x$. For a large system, it is practically impossible to study all the possible random alloys. To address this issue, Zunger *et al.* [1] proposed a structural model called special quasirandom structure (SQS) to mimic the correlation of an infinite substitutional random alloy by a finite system alloy. Wei *et al.* in Ref. [2] reformulate it for the case of 2D transition metal dichalcogenides (TMD).

For a perfect random alloy, the correlation function is given by $\prod_{k,m}(\mathrm{R}) = (2x-1)^k$, where $k = 2, 3, ...$ indicates the pair (2), triple (3),... correlation functions; $m = 1, 2, 3, ...$ indicates the first, second, third,...,nearest-neighbor distances and x represents the concentration of the substituted atoms [3]. In the SQS method, the sites i occupied by atoms A or B are assigned to a variable σ_i equals to -1 or 1, respectively. The correlation function for this binary alloy can be written as $\prod_{k,m} = \frac{1}{N_{k,m}} \sum_{\{k,m\}} \sigma_1\sigma_2...\sigma_k$, where $N_{k,m}$ is the total number of shape that can be obtained when varying k and m. In the present study, only the nearest-neighbor pairs are scrutinized, since the interactions between far distant neighbors have been reported not to have much effect on the total energy [2]. In this model (nearest neighbor pair), the correlation function $\Pi_{2,1}$ is given

by $\Pi_{2,1} = \frac{1}{N_{bond}} \sum_{j,h=1,N}^{j>h} \sigma_j \sigma_h$, where N_{bond} is the number of bonds between nearest neighbor metals, N is the total number of transition metal in the supercell, j and h represent the two pair sites considered. If the total number of the nearest-neighbor bonds between $A-A$, $B-B$ and $A-B$ atoms are denoted by N_{AA}, N_{BB} and N_{AB}, respectively, the correlation function can be written as :

$$\Pi_{2,1} = \frac{N_{AA} + N_{BB} - N_{AB}}{N_{AA} + N_{BB} + N_{AB}}. \tag{B.1}$$

The number of atoms A and B in an $A_{1-x}B_x$ alloy is given by: $N_A = N(1-x)$ and $N_B = Nx$. In addition, assuming that z is the coordination number of atoms in the system, N_A and N_B are related to the number of bonds as:

$$\begin{cases} N_A = \frac{N_{AB}+2N_{AA}}{z} \\ N_B = \frac{N_{AB}+2N_{BB}}{z} \end{cases} \tag{B.2}$$

Therefore, the correlation function in Eq. B.1 becomes :

$$\Pi_{2,1} = 1 - 4x + \frac{8N_{BB}}{Nz}. \tag{B.3}$$

Thus, eqn. B.3 shows that the correlation function can be completely described by N_{BB}. The SQS configurations are considered to have the same correlation functions as the perfect random alloys: $\prod_{2,1}(R) = \prod_{2,1}(SQS)$ [3]. Using this equality and eqn. B.3, we found that the number of $N_{BB} = \frac{1}{2}x^2Nz$ in a TMD monolayer. This later is used in this study to generate all random configurations.

Bibliography

[1] A. Zunger, S.-H. Wei, L. Ferreira, J. E. Bernard, Physical Review Letters 65 (3) (1990) 353. [157]

[2] X.-L. Wei, H. Zhang, G.-C. Guo, X.-B. Li, W.-M. Lau, L.-M. Liu, Journal of Materials Chemistry A 2 (7) (2014) 21012109. [157]

[3] C. Jiang, C. Wolverton, J. Sofo, L.-Q. Chen, Z.-K. Liu, Physical Review B 69 (21) (2004) 214202. [157, 158]